THE UNIVERSITY OF MICHIGAN
JAN 28 1960
ENGINEERING LIBRARY

THE AERONAUTICAL QUARTERLY

A Journal devoted to Aeronautics and the Allied Sciences

Volume X NOVEMBER 1959 Part 4

CONTENTS

The Atmospheric Stress-Corrosion Resistance of some Forged High Strength Aluminium Alloys and an Assessment of the Effects of a Step Quench into Molten Salt — *W. M. Doyle and R. G. Jones*

A Unified Numerical Method for the Calculation of the Loading on Wings with Subsonic Leading Edges. Part II — *G. J. Hancock*

The Stress Concentration Factors in Cylindrical Tubes with Transverse Circular Holes — *H. T. Jessop, C. Snell and I. M. Allison*

Theoretical and Experimental Studies of Stall Propagation in Rows of Axial Flow Compressor Blades — *M. D. Wood*

The Design of an Annular Entry to a Circular Duct — *J. C. Gibbings*

Stresses Around Reinforced Elliptical Holes, with Applications to Pressure Cabin Windows — *W. H. Wittrick*

Index to Volume X

LONDON

ROYAL AERONAUTICAL SOCIETY

4 HAMILTON PLACE W1

15/-

THE AERONAUTICAL QUARTERLY

Editorial Board

Dr. A. M. BALLANTYNE, T.D., B.Sc., Ph.D., Hon.F.C.A.I. F.I.A.S., F.R.Ae.S. (*Chairman*)

Mr. HAYNE CONSTANT, C.B., C.B.E., M.A., F.R.S., F.R.Ae.S.

Sir HAROLD ROXBEE COX, D.Sc., D.I.C., Ph.D., F.I.A.S., F.R.Ae.S.

Sir WILLIAM FARREN, C.B., M.B.E., M.A., D.Sc., F.R.S., Hon.F.I.A.S., Hon.F.R.Ae.S.

Sir ARNOLD HALL, M.A., F.R.S., F.R.Ae.S.

Sir BENNETT MELVILL JONES, C.B.E., A.F.C., M.A., F.R.S., Hon.F.I.A.S., Hon.F.R.Ae.S.

Sir ALFRED PUGSLEY, O.B.E., D.Sc., F.R.S., F.R.Ae.S.

Sir GEOFFREY TAYLOR, M.A., D.Sc., F.R.S., Hon.F.R.Ae.S.

Dr. P. B. WALKER, C.B.E., M.A., F.R.Ae.S.

Editor—E. C. PIKE, M.A., A.F.R.Ae.S.

Editorial Referees

Aerodynamics

(a) *General*

Sir LEONARD BAIRSTOW
Mr. D. KEITH-LUCAS
Prof. W. A. MAIR
Mr. L. F. NICHOLSON
Dr. R. C. PANKHURST
Mr. E. F. RELF
Prof. E. J. RICHARDS
Dr. B. THWAITES

(b) *Fluid Motion*

Dr. G. K. BATCHELOR
Mr. A. FAGE
Dr. D. W. HOLDER
Prof. L. HOWARTH
Dr. W. P. JONES
Dr. J. W. MACCOLL
Prof. J. H. PRESTON
Prof. H. B. SQUIRE
Prof. G. TEMPLE
Prof. G. N. WARD
Prof. A. D. YOUNG

(c) *Stability and Control*

Mr. L. W. BRYANT
Mr. S. B. GATES
Mr. H. B. IRVING
Mr. G. H. LEE
Mr. M. B. MORGAN
Mr. H. H. B. M. THOMAS

Helicopters and Propellers

Prof. J. A. J. BENNETT
Mr. P. BRETT
Mr. L. G. FAIRHURST
Mr. R. HAFNER
Dr. G. S. HISLOP
Capt. R. N. LIPTROT

Instruments and Electrical Equipment

Dr. G. E. BAIRSTO
Sir GEORGE GARDNER
Dr. C. S. HUDSON
Mr. C. N. JAQUES
Mr. F. W. MEREDITH

Aircraft Design

Mr. R. BOORMAN
Mr. R. M. CLARKSON
Mr. A. N. CLIFTON
Mr. H. H. GARDNER
Mr. H. KNOWLER
Mr. W. E. W. PETTER
Mr. F. H. POLLICUTT
Dr. A. E. RUSSELL
Mr. R. S. STAFFORD
Mr. W. H. STEPHENS

Radio and Radar

Mr. J. F. ATHERTON
Mr. B. G. GATES
Dr. R. L. SMITH ROSE
Dr. A. M. UTTLEY
Sir ROBERT WATSON-WATT

Aviation Medicine

Dr. K. G. BERGIN
Dr. A. BUCHANAN BARBOUR

Meteorology

Sir DAVID BRUNT
Mr. J. K. HARDY
Prof. P. A. SHEPPARD

Sound

Mr. W. MAKINSON
Mr. F. B. GREATREX
Mr. N. FLEMING

Aircraft Propulsion

Mr. A. D. BAXTER
Mr. A. V. CLEAVER
Sir A. H. ROY FEDDEN
Dr. S. HOOKER
Mr. A. R. HOWELL
Mr. W. H. LINDSEY
Mr. P. LLOYD
Dr. A. W. MORLEY
Dr. E. S. MOULT
Mr. N. S. MUIR
Mr. F. NIXON
Mr. F. M. OWNER
Mr. H. PEARSON
Sir DAVID PYE
Mr. H. SAMMONS
Prof. O. A. SAUNDERS
Prof. A. G. SMITH

Air Transport

Mr. A. C. CAMPBELL ORDE
Mr. P. G. MASEFIELD
Mr. N. E. ROWE
Mr. B. S. SHENSTONE
Mr. W. TYE

Aircraft Accessories

Mr. A. E. BINGHAM
Mr. W. C. CLOTHIER
Mr. H. G. CONWAY
Sir GEORGE DOWTY
Mr. R. GRAHAM
Mr. C. D. HOLLAND

Performance

Mr. H. DAVIES
Mr. D. R. NEWMAN
Mr. A. H. YATES

Flight Testing

Mr. R. R. DUDDY
Mr. P. A. HUFTON
Mr. E. T. JONES
Mr. S. SCOTT HALL
Mr. H. L. STEVENS

Structures

Prof. J. H. ARGYRIS
Mr. A. C. BROWN
Mr. H. L. COX
Mr. D. J. FARRAR
Prof. W. S. HEMP
Prof. R. HILL
Mr. H. B. HOWARD
Col. H. T. JESSOP
Mr. E. D. KEEN
Mr. F. A. KERRY
Dr. D. M. A. LEGGETT
Mr. R. L. LICKLEY
Prof. A. J. SUTTON PIPPARD
Prof. S. C. REDSHAW
Mr. R. H. SANDIFER
Sir RICHARD SOUTHWELL

Fuels and Oils

Mr. E. L. BASS
Dr. J. W. DRINKWATER
Prof. F. H. GARNER
Prof. W. E. GARNER
Dr. K. E. W. RIDLER
Dr. C. G. WILLIAMS

Materials

Dr. L. AITCHISON
Dr. N. P. ALLEN
Mr. G. FORREST
Prof. N. F. MOTT
Mr. L. ROTHERHAM
Dr. H. SUTTON
Dr. C. SYKES

Vibration and Flutter

Mr. E. G. BROADBENT
Prof. A. R. COLLAR
Prof. W. J. DUNCAN
Dr. R. A. FRAZER
Mr. H. TEMPLETON
Mr. M. O. W. WOLFE

The Atmospheric Stress-Corrosion Resistance of some Forged High Strength Aluminium Alloys and an Assessment of the Effects of a Step-Quench into Molten Salt

W. M. DOYLE, Ph.D., M.Eng., F.I.M. and R. G. JONES, B.Sc., L.I.M.

(*High Duty Alloys Limited*)

SUMMARY: Since the introduction of aluminium-zinc-magnesium-copper alloys, investigations into the behaviour of these high strength materials, over a wide range of composition, have indicated the significance of corrosion as a factor affecting the cracking of these alloys after prolonged stressing at loads below the ultimate tensile strength of the material.

Most of the previous work designed to assess the stress-corrosion resistance of aluminium-zinc-magnesium-copper alloys (D.T.D. 683A*) was carried out on sheet and plate material and the present investigation is concerned with the examination of these materials in the form of large hand-forged slabs, tested in the short transverse direction. In addition, tests have been carried out on an aluminium-copper-magnesium alloy conforming to B.S.S. L.65†.

The effects of variations in heat-treatment procedure on stress-corrosion resistance have been determined on one selected alloy of the D.T.D. 683A type and step-quenching in molten salt, following solution heat-treatment, has been shown to give maximum resistance to atmospheric stress-corrosion. The effects of this heat treatment on the residual stress, fatigue and tensile properties of forged material have also been determined.

1. Historical Review

Following the pioneer work by the National Physical Laboratory under Dr. Rosenhain[1] during the First World War, the introduction in 1921 of an aluminium-zinc-magnesium-copper alloy containing approximately 20 per cent zinc and having an ultimate tensile strength of about 40 tons/in.^{2} in the heat-treated condition, widened the field of application of aluminium by providing prospective users with a light alloy having a strength greater than that obtainable with the

*The specification covering forged alloys of this type has now been subdivided into D.T.D. 5024 and D.T.D. 5034.

†This specification has now been divided, forged products being covered by B.S.S. L.77.

Received May 1959.

[The Aeronautical Quarterly, Vol. X, November 1959]

aluminium-copper-magnesium type alloys. Subsequent work by Sander and Meissner[2] extended the range of these alloys by investigating the lower ranges of zinc content, but the results indicated that although high levels of tensile strength were obtainable, the alloys were susceptible to cracking after prolonged stressing under corrosive conditions, atmospheric corrosion being sufficient to initiate failure.

Although many of the early applications of these new alloys failed because of their susceptibility to stress corrosion, a systematic examination of the factors affecting the stress-corrosion resistance was not undertaken until the early years of the Second World War, when the need for a high strength alloy assumed great importance. A joint investigation by Rolls-Royce Limited and High Duty Alloys Limited resulted in an alloy of this type being marketed in 1937 under the name of Hiduminium R.R.77[3]. Development work proceeded and by 1943 the nominal composition of this alloy was fixed at 5·5 per cent zinc, 2·8 per cent magnesium, 0·5 per cent manganese and 0·4 per cent copper[4], and this composition has remained virtually unaltered to the present day. Since its introduction, many thousands of tons of this alloy in the form of small and large forged structural components have given excellent service in both military and civil aircraft.

In the United States, parallel development work was in progress and culminated in the introduction in late 1943 of the alloy generally known as 75S (7075). This alloy contained similar amounts of zinc and magnesium to Hiduminium R.R.77, but the nominal copper content was 1·6 per cent and a proportion of the manganese was replaced by an addition of chromium[5]. The claim was made that the presence of chromium improved the stress-corrosion resistance. The work indicating the benefits of chromium in promoting increased stress-corrosion resistance had been carried out mainly on sheet and plate material[5] and it had been suggested that the improved life resulted from a modified elongated grain structure in the wrought product together with the prevention of selective precipitation at the grain boundaries. Later work by Chadwick, Muir and Grainger[6] showed that the improvement of the safe stress levels, with chromium, could be accounted for by the fibrous elongated structure in the sheet specimens tested. However, since grain structures are affected by methods of fabrication, the beneficial effect of chromium may not be expressed as common to all wrought forms of these alloys.

The cracking of aluminium-zinc-magnesium alloys during stress-corrosion is, like the corrosion attack, confined mainly to the grain boundaries. Evidence of the existence of solute-depleted intergranular zones, resulting from local over-ageing, has been found in several aluminium alloys and the marked influence of this phenomenon on the susceptibility to stress corrosion has been shown on aluminium-zinc alloys[7, 8], in which the depleted regions are formed by discontinuous precipitation. Since this precipitation is thought to be accelerated by grain-boundary strains[9], a thermal treatment designed to modify the intensity of grain-boundary precipitation, relative to that within the grains, by reducing grain-boundary strains might be effective in increasing resistance to stress corrosion. A slow or interrupted quench has been proposed as a means of reducing the quenching stresses and resultant grain-boundary strain and it has been reported[10] that quenching

aluminium-zinc-magnesium-copper alloys from the solution-treatment temperature into a salt, or oil, bath at 150°C for a few minutes, and air cooling to room temperature before precipitation treatment, had a beneficial effect on the stress-corrosion resistance.

2. Material Tested

The manipulation of cast billet stock during manufacture may give rise to hand-forged slabs exhibiting marked directional effects. Although little difference in proof stress or ultimate tensile strength may be measured in the three mutually perpendicular geometric directions, the percentage elongation is least in the short transverse direction and this condition is accentuated when the direction of the axis of the original cast stock coincides with the smallest dimension of the forged slab. Testing has shown that the stress-corrosion resistance of a forged slab is lowest in this short transverse direction.

All the atmospheric stress-corrosion tests reported herein have been carried out by the Research Division of High Duty Alloys Limited on sections cut from the short transverse direction of slabs, approximately 7 in. × 15 in. × 48 in., forged from semi-continuous cast ingots of 15½ in. diameter, by upsetting, drawing out at right angles, re-upsetting and drawing out at a right angle in the same plane. Previous experience has been that a modification to chemical composition or heat-treatment procedure, which can be shown to produce a substantial increase in the stress-corrosion resistance in the short transverse direction of these slabs, will produce comparable benefits in any other direction.

Subsequently, it was found that quenching into molten salt (I.C.I. Tempering Salt C.T.S.150) improved the atmospheric stress-corrosion resistance of Hiduminium R.R.77, and this necessitated a full assessment of the effects of the modified quenching procedure on the mechanical properties. Determination of the tensile properties of material heat-treated at various ruling thicknesses was carried out on test bars cut from forged bars made from cast ingot by upsetting and drawing out at right angles. A large number of die-forged components, selected and pre-machined to have a 2 in. ruling section, at the heat-treatment stage, were also tested to determine the minimum design properties. Additional work, on both forged bar and sections from the longitudinal and short transverse directions of a hand-forged slab, was designed to compare the fatigue properties under conditions of rotating-cantilever and direct-stressing. The residual stresses in a die-forged undercarriage component were determined by strain-gauge cut-up tests.

3. Results

3.1. The Effect of Chromium and Cadmium on the Atmospheric Stress-Corrosion of Al-Zn-Mg-Cu Alloys

Individual stress-corrosion specimens of dimensions 0·250 in. × 0·960 in. × 6 in. were machined from sections cut from the short transverse direction of large hand-forged slabs, 7 in. × 15 in. by approximately 48 in. long, such that the stressed face

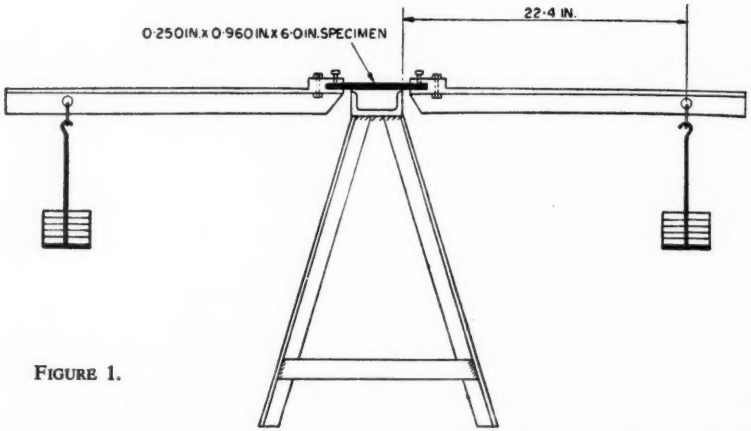

FIGURE 1.

of each specimen was parallel to the longitudinal direction. The slabs were forged on a 3,000 ton hydraulic press from 15½ in. diameter semi-continuous cast ingots.

Several billets in Hiduminium R.R.77 were cast under production conditions to act as norms. To examine the effects of chromium on the stress-corrosion resistance of forged materials, an addition of 0·2 per cent chromium was made to the standard alloy for one billet, while in a second the addition of chromium was accompanied by a decrease in the manganese content. Two further chromium-containing alloys were tested, these being of similar basic composition to Hiduminium R.R.77, but based on the American 7075 and 7079 type alloys. The effect of cadmium was assessed by means of one block containing 0·06 per cent of this element added to the standard Hiduminium R.R.77. An alternative high strength alloy, widely used for aircraft applications, is an aluminium-copper-magnesium alloy conforming to British Standard Specification L.65 and three billets in Hiduminium 66 were prepared to provide comparable test material in this alloy.

The sections of forged slab were heat treated in the form of rough blanks of approximately 1¼–2 in. square by 7 in. long and details of the heat treatments used on the various alloys are given in Table I.

The stress-corrosion resistance of the aluminium alloy slabs has been assessed by means of atmospheric stress-corrosion tests in bending, the test specimens being stressed in four-point bending under atmospheric conditions at calculated stresses equivalent to 90 per cent of the 0·1 per cent proof stress measured on standard tensile testpieces cut from adjacent locations. This test, developed by A. Black of Vickers-Armstrongs, has been used by the Royal Aircraft Establishment, Farnborough[11], and members of the Society of British Aircraft Constructors for the measurement of stress-corrosion life of materials to D.T.D.683A composition. The general form of the test equipment used by the authors for the determination of these properties is shown in Fig. 1, the test site being located in semi-rural surroundings. While the specimens on test were open to the atmosphere, a roofed-in area provided protection from direct rain.

CHEMICAL COMPOSITION, HEAT TREATMENT, TENSILE PROPERTIES, AND RESULTS OF ATMOSPHERIC STRESS-CORROSION TESTS ON SECTIONS FROM THE SHORT TRANSVERSE DIRECTION OF LARGE HAND-FORGED SLABS

Slab Number	Alloy Type	Chemical composition (per cent)									Heat Treatment	Average Tensile Properties			Atmospheric Stress Corrosion in Bending. Life on Test (days at 90% of 0·1% P.S.)
		Zn	Mg	Cu	Mn	Cr	Fe	Si	Ni	Ti		0·1% P.S. (tons/in.²)	U.T.S. (tons/in.²)	Elongation (per cent)	
1	Hiduminium R.R.77 (Specification D.T.D. 683A)*	5·58	2·73	0·40	0·50	—	0·25	0·13	<0·10	0·05	4 hr. 460°C, B.W.Q., 12 hr. 135°C	28·4	32·5	5	67, 76, 77, 105
2		5·54	2·79	0·42	0·53	—	0·29	0·16	<0·10	0·06		28·4	31·3	2	15, 17, 25, 35
3		5·52	2·83	0·43	0·52	—	0·31	0·19	<0·10	0·05	6 hr. 460°C, B.W.Q., 12 hr. 135°C	29·0	32·7	2	17, 20, 22
4		5·56	2·73	0·40	0·50	—	0·26	0·14	<0·10	0·05	4 hr. 460°C, 85°C, 12 hr. 135°C	28·2	31·7	3	100, 120, 160
5		5·58	2·70	0·45	0·51	—	0·30	0·12	<0·10	0·07		28·5	32·8	4	27, 56
6	Hiduminium R.R.77, added Cr	5·53	2·71	0·39	0·56	0·19	0·20	0·11	<0·10	0·05	4 hr. 465°C, 85°C, 12 hr., 135°C	20·2	25·4	4	105U, 319U, 414
7	Hiduminium R.R.77, added Cr, reduced Mn	5·56	2·76	0·43	0·06	0·20	0·24	0·09	<0·10	0·07		26·0	30·8	3	34, 36, 42, 44
8	Hiduminium R.R.77, added Cd	5·54	2·70	0·42	0·50	Cd 0·06	0·23	0·14	0·03	0·06	4 hr. 460°C, 85°C, 12 hr. 135°C	28·3	32·2	2	31, 35
											4 hr. 460°C, B.W.Q., 12 hr. 135°C	26·3	29·7	2	44, 54
9	7075 type	5·62	2·63	0·92	0·02	Cr 0·16	0·29	0·11	<0·10	0·06	6 hr. 460°C, C.W.Q., 24 hr. 120°C	27·0	34·0	5	31, 33, 68
10	7079 type	4·52	3·20	0·59	0·04	0·16	0·23	0·12	0·02	0·05	4 hr. 465°C, 85°C, 24 hr. 120°C	25·8	32·0	7	28, 33, 37
											4 hr. 444°C, C.W.Q., 5 days N.A., 48 hr. 115°C	29·2	33·7	4	11, 18, 20, 59
11	7079 type	4·56	3·14	0·58	0·01	0·20	0·24	0·09	<0·10	0·06	6 hr. 444°C, C.W.Q., 8 days N.A., 48 hr. 115°C	25·7	31·5	3	25, 76, 83
12	Hiduminium 66 (Specification B.S. L.65)†	<0·15	0·69	4·10	0·74	—	0·29	0·82	<0·10	<0·15	4 hr. 500°C, below 70°C, 6 hr., 185°C	25·8	29·0	2	35U, 161U, 362U
13		<0·15	0·70	4·14	0·77	—	0·31	0·83	<0·10	0·04		26·0	29·8	3	21, 21, 32, 54, 63
14		<0·15	0·76	4·26	0·76	—	0·28	0·77	<0·10	0·05		26·9	30·1	3	17, 21, 26, 33, 62

*The specification covering forged alloys of this type has now been subdivided into D.T.D. 5024 and D.T.D. 5034.
†Now replaced by B.S.S. L.77.

B.W.Q.—Quenched in boiling water.
C.W.Q.—Quenched in water at room temperature.
85°C—Quenched in water at 85°C.
N.A.—Natural age

U—Specimens unbroken.
U.T.S.—Ultimate tensile stress.
P.S.—Proof stress.

The results of the atmospheric stress-corrosion tests are given in Table I, together with the chemical compositions, details of the heat treatments used and the tensile properties. Comparison of the results obtained on Slabs 5 and 6 confirm that the addition of chromium has rendered the alloy quench-sensitive, the tensile strength being 5–7 tons/in.^{2} lower than normal Hiduminium R.R.77. Although the life on atmospheric stress-corrosion test is much improved, the actual test load was much lower for the chromium-containing material. The addition of chromium concomitant with a reduction in the manganese content (Slab 7) has produced no significant benefit in stress-corrosion resistance. The comparatively poor stress-corrosion lives for these alloys containing chromium, but with low manganese content, is also demonstrated by reference to the results on Slabs 9, 10 and 11, although the tensile results obtained on Slab 10 indicate that this particular composition is not as quench-sensitive as that containing both chromium and manganese. Hiduminium R.R.77 with an addition of 0·06 per cent of cadmium has not shown any significant increase in stress-corrosion resistance over the normal alloy.

The results obtained on five different slabs in the normal Hiduminium R.R.77, (Slabs 1–3 heat treated with a boiling-water quench, Slabs 4–5 quenched at 85°C) show that slabs of similar composition, heat treated under similar conditions to produce the same level of tensile properties, may give very dissimilar lives on atmospheric stress-corrosion test, although reasonably consistent values have been obtained on individual slabs. The values determined on three slabs in Hiduminium 66 (Slabs 12–14) indicate that a similar effect is found in the Al-Cu-Mg alloy to B.S.S. L.65. Rather short lives were recorded on two of these slabs and it appears that this alloy can be as susceptible to atmospheric stress corrosion as the zinc-containing alloys under similar test conditions.

The results of the series of tests on large hand-forged slabs in various alloys of the aluminium-zinc-magnesium-copper type have indicated that the minor modifications to composition examined will not improve the stress-corrosion resistance with the maintenance of the tensile properties normally obtained with these materials.

3.2. The Effects of Modified Quenchng Conditions on Stress-Corrosion Resistance

The presence of an inhibitor element, *e.g.* chromium or cadmium, in alloys of the Al-Zn-Mg-Cu type had not necessarily proved beneficial to stress-corrosion resistance and it was decided to investigate the effect of slow or interrupted quenching only on the chromium-free alloy Hiduminium R.R.77. In order to provide directly comparable results, the material was taken from a single hand-forged slab in Hiduminium R.R.77. The material selected was known to give rise to short life on atmospheric stress-corrosion testing, when given the normal heat treatment for Hiduminium R.R.77 (*see* Slab 2 in Table I), and was used to enable a rapid assessment of the heat-treatment processes investigated.

Since Fink and Willey[12] have shown that the corrosion resistance and tensile properties of Alcoa 7075 were markedly dependent on the rate of cooling over the

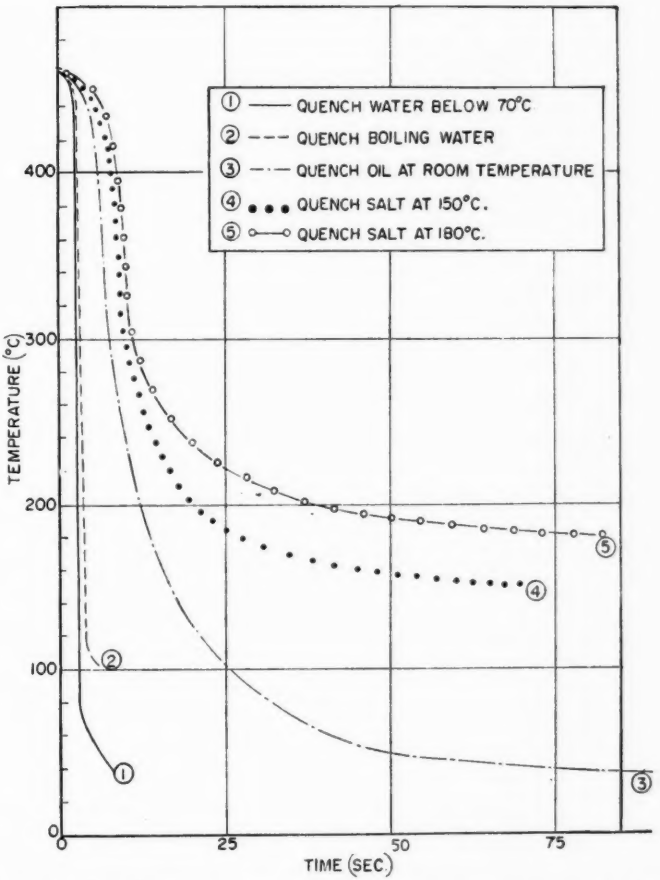

FIGURE 2. Cooling rates of ½ in. × 1 in. × 7 in. blanks. Hiduminium R.R.77 Solution treated 460°C.

critical range 400–290°C following solution treatment, the rates of cooling of the specimens of Hiduminium R.R.77 used in the present investigation were measured. The cooling rates produced by the quench media investigated were determined by measuring the temperatures at the geometric centre of a ½ in. × 1 in. × 7 in. section from the short transverse direction of the forged slab, using the Nash & Thompson high-speed temperature recorder, and the resultant cooling curves are depicted in Fig. 2.

The individual test blanks were solution treated for 4 hours at 460°C, quenched and subsequently aged for 12 hours at 135°C. The quench media employed were: — water below 70°C, water at 85°C, boiling water, oil at room temperature and molten salt either at 150°C or 180°C. In the case of the molten salt quenches, the samples

TABLE II

THE EFFECT OF VARIATION IN QUENCH CONDITION ON THE TENSILE PROPERTIES AND ATMOSPHERIC STRESS-CORROSION RESISTANCE OF SECTIONS FROM THE SHORT TRANSVERSE DIRECTION OF HAND-FORGED SLAB IN HIDUMINIUM R.R.77 HEAT-TREATED AS ½ IN. × 1 IN. × 7 IN. BLANKS

Quench Condition	*Average Tensile Properties*			*Bend Test Results (Life in days at 90% of 0·1% proof stress)*
	0·1% P.S. (tons/in.²)	*U.T.S. (tons/in.²)*	*Elongation (per cent)*	
Water below 70°C	30·0	34·7	4	5, 5, 6, 8, 12
Water at 85°C	30·0	33·0	2	12, 17, 18, 24, 27
Boiling water	28·4	31·3	2	15, 17, 25, 35
Oil at room temperature	29·0	32·7	2	44, 56, 69
Intermediate quench in:—				
Salt at 150°C for 5 min.*	28·9	31·8	2	72, 86
Salt at 150°C for 10 min.*	29·0	32·3	2	77, 91
Salt at 150°C for 20 min.*	28·0	32·3	4	42, 62
Salt at 180°C for 5 min.*	28·2	31·0	2	106, 265U
Salt at 180°C for 10 min.*	28·1	32·0	2	265U, 265U
Salt at 180°C for 20 min.*	27·6	31·8	2	265U, 265U

U—Specimens unbroken. *Followed by quench in water at 85°C.

were allowed to remain immersed for 5, 10 or 20 minutes before transfer to a water quench at 85°C.

Atmospheric stress-corrosion tests were carried out in four-point bending, using the method previously described, and the results are given in Table II, arranged in order of decreasing severity of quench, assessed from the graphs of Fig. 2. The use of boiling water in comparison with cold water quenching has produced only a small increase in life on atmospheric stress-corrosion test, but examination of Fig. 2 shows that there is very little difference in the initial cooling rates of the samples. Specimens quenched into an oil bath at room temperature showed an improvement in life, while the tensile properties were maintained at a high level.

Step-quenching from the solution treatment temperature, using an intermediate quench in a salt bath at 150°C, produced an approximate fourfold improvement in life for a salt quench of 5–10 min. duration, although it appeared that the improvement in stress-corrosion resistance decreased with a longer period of immersion in the salt bath. Results of tests on material given a similar step-quench, using a salt bath at 180°C, were very satisfactory, one test piece breaking at 106 days, with the remaining five specimens being unbroken during the test period of 265 days. The level of tensile properties attained on these small section thicknesses was comparable with that obtained by quenching into boiling water, giving approximately 28 tons/in.² proof stress with 31 tons/in.² ultimate tensile strength.

During a preliminary investigation, tests on short transverse sections of a hand-forged slab showed that the use of an intermediate salt bath at 200°C gave tensile properties approximately 2 tons/in.² lower than obtainable with a bath at 180°C, for similar specimen size. Accelerated stress-corrosion tests indicated that

the higher quench temperature did not produce the increased stress-corrosion resistance noted on material quenched at 180°C.

Although further testing has indicated that the tensile strength decreases with increasing section thickness, for a quench into molten salt at 180°C, the efficacy of this heat treatment in improving the atmospheric stress-corrosion resistance of Hiduminium R.R.77 appeared to warrant a full assessment of the effects of step-quenching, using an intermediate salt bath at this temperature. The benefits of step-quenching on the atmospheric stress-corrosion resistance of Hiduminium R.R.77 have been confirmed on test material taken from four further forged slabs and the results are listed in Table III.

3.3. The Effect of Quench Procedure on Residual Stress

The mechanical properties developed by the heat treatment of high strength aluminium alloys depends on the retention of a super-saturated solid solution by rapid quenching from the solution treatment temperature, followed by an ageing treatment designed to allow the intermetallic phases to precipitate in a controlled manner. This rapid quenching of wrought products during heat treatment may produce a high level of internal stress and these stresses may either give rise to distortion troubles on subsequent machining or, in conjunction with assembly stresses, provide the necessary stress to initiate failure under conditions of stress corrosion. The level of internal stress may be reduced by boiling-water quenching[13] thus producing a slower cooling rate in thick sections, although lower mechanical properties will result in certain alloys. Thus a compromise between low internal stress and high tensile properties may have to be sought and it is for this reason that forgings in 7075 type alloy exceeding 3 in. thickness are rough-machined, to reduce the mass at the heat treatment stage[4].

Although Hiduminium R.R.77 is not prone to mass effect on heat treatment, it is recommended that forgings are machined before heat treatment such that the amount of metal to be removed in the fully heat-treated condition is kept to a minimum. The results of a long investigation into the effects of quenching have

TABLE III

ATMOSPHERIC STRESS-CORROSION TESTS IN BENDING ON SECTIONS FROM THE SHORT TRANSVERSE DIRECTION OF FOUR HAND-FORGED SLABS IN HIDUMINIUM R.R.77 AND TESTED AT 90% OF THE MEASURED 0·1% PROOF STRESS

Bend Test Life in Days, After Heat Treatment Involving:—	
Quench in water at 85°C	*Step-quench: salt bath at 180°C for 10 min. followed by water quench at 85°C*
12, 17, 18, 24, 27	265U, 265U
8, 16, 16	179U, 179U
55, 63	179U, 480U
32, 39, 60	221, 241

TABLE IV

EFFECT OF QUENCH CONDITION ON THE INTERNAL STRESS OF FORGED PRODUCTS IN HIDUMINIUM R.R.77 (D.T.D. 683A) AND HIDUMINIUM 66 (B.S.S. L.65)

Quench Condition	*Machining Distortion Measured on Forged Component in Hiduminium R.R.77 (Closure 10^{-3} in.)*	*Highest Level of Residual Stress Determined by Strain-Gauge Methods in Comparable Locations of Machined Undercarriage Forgings (Stress in tons/in.² tension)*	
		Hiduminium R.R.77	*Hiduminium 66*
Water below 70°C	26·5	—	7·7
Water at 85°C	—	5·0	3·2
Boiling water	1·4	2·8	1·2
Step quench: salt bath at 180°C, followed by water quench at 85°C	0·9	0·8	—

also shown that the distortion is least when the machining is carried out symmetrically.

The effect of variations in quenching condition on the level of internal stress induced in forged products in Hiduminium R.R.77 was assessed by comparing the amount of distortion occurring in slitting a stamping or by measuring the residual stresses present by the use of electrical strain gauges. In the latter method, strain-gauge elements were cemented to the surface of fully machined undercarriage forgings, which were then sectioned by sawing, to allow relief of stress, the change of resistance of the gauge being proportional to the change of strain. The components used for the strain-gauge tests were cylindrical die-forgings designed for use in the main undercarriage of a military aircraft. Apart from slotting between lugs, there was no machining on the outside of the components and pre-heat-treatment machining was carried out such that 0·1 in. was removed from the internal surfaces after full heat treatment. Strain-gauge tests were also done on identical components in Hiduminium 66 to B.S.S. L.65 subjected to the same machining operations.

The test forgings in Hiduminium R.R.77 were solution treated for 4 hours at 460°C, quenched as indicated in Table IV, and aged for 12 hours at 135°C, while the forged components in Hiduminium 66 were solution treated for 4 hours at 500°C, quenched also as indicated in Table IV, before ageing for 6 hours at 185°C.

The results obtained in all groups of tests are given in Table IV and indicate that, although the level of residual stress in forged products in Hiduminium R.R.77 may be reduced by the use of increased water-quenching temperatures, a step-quench treatment involving a salt bath at 180°C produces the lowest level of internal stress. Although hot-water quenching reduces the level of internal stress in components in Hiduminium 66, the mechanical properties required by B.S.S. L.65 are only obtained by quenching in water at a temperature not exceeding 70°C and the use of a boiling-water quench would produce greatly reduced tensile strength[14].

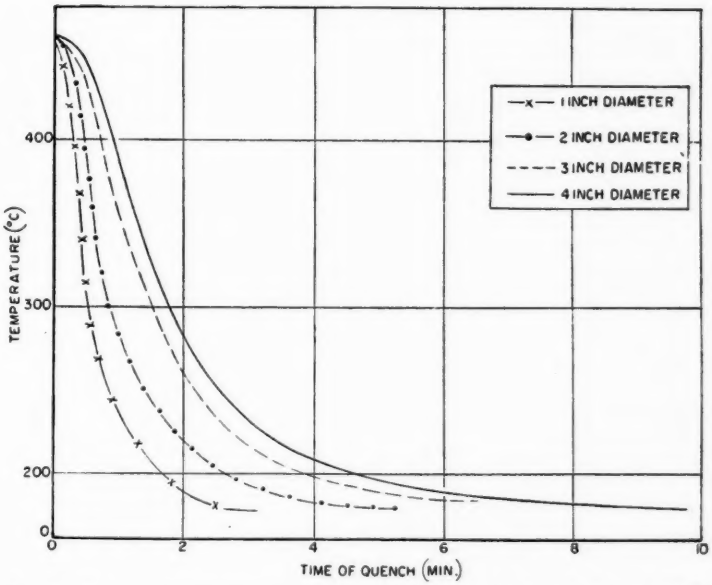

FIGURE 3. Cooling curves measured at the centre of 6 in. long cylinders of Hiduminium R.R.77 quenched into molten salt at 180°C.

3.4. The Effect of Step-Quenching on Tensile Properties of Forged Bar

Initial tests on a forged slab in Hiduminium R.R.77 had shown that the tensile strength decreased with increasing section thickness for a standardised quench of 10 min. in molten salt at 180°C, before a water quench at 85°C. It was realised that, because of different cooling rates, the actual time at 180°C was dependent on section thickness and it was decided to investigate the effect of modified quenching periods.

Cooling curves were determined by means of thermocouples placed at the geometric centres of 6 in. lengths of 4, 3, 2 and 1 in. diameter forged bar produced from common ingot stock; the results are shown in Fig. 3, from which it may be seen that all samples were fully quenched to 180°C in the 10 min. period. Using these results, a second series of quench experiments was conducted in which selected blanks were allowed to remain at the salt bath temperature for differing periods.

The tensile properties obtained on specimens machined from these fully heat-treated blanks, shown graphically in Fig. 4, indicate that, for section thicknesses up to 3 in., the level of strength is not dependent on time of immersion over the range of times investigated. Thus, for material heat treated at a maximum ruling section of 3 in., a quench period of 10 min. in molten salt at 180°C will suffice to develop the full properties obtainable with the standard solution treatment and ageing employed. However, to maintain a level of tensile strength similar to that obtained

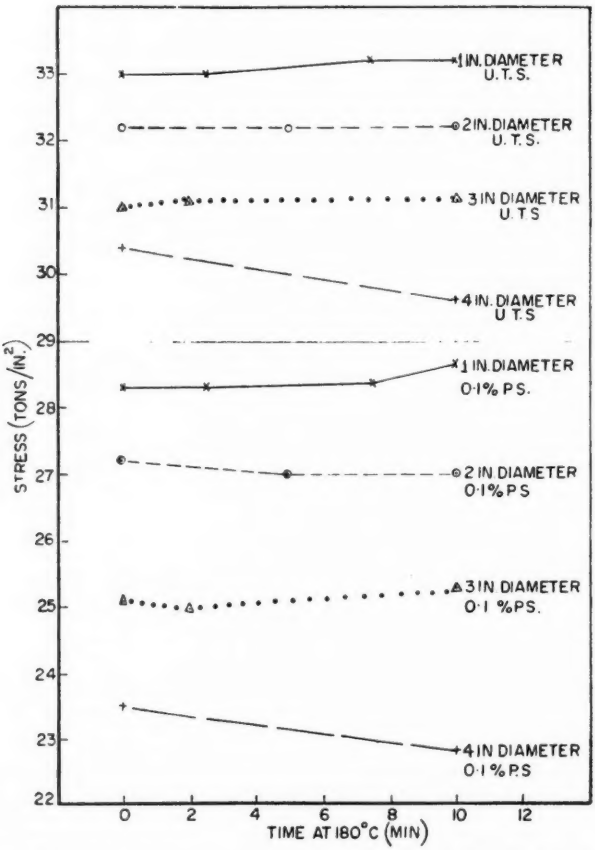

FIGURE 4. Tensile tests at room temperature on Hiduminium R.R.77 forged bar quenched into molten salt at 180°C. Longitudinal tests.

in alloys conforming to B.S.S. L.65, the section thickness of salt-quenched material should be limited to 2 in.

3.5. THE EFFECTS OF CHARGE/SALT RATIO

Heat treatment under production conditions conventionally involves the use of large furnace charges and, to provide the most economical processing of material heat-treated by the salt-quench process, the charge/salt ratio should be high. Since the thermal mass of forgings at the solution treatment temperature would raise the temperature of the quench medium and this might have a deleterious effect on the tensile properties, it was decided to investigate the effect of charge/salt ratios of 1/230, 1/100 and 1/16. The results of tensile tests carried out on sections cut from components are given in Table V, values determined on a similar forging

TABLE V

A COMPARISON OF THE TENSILE PROPERTIES OBTAINED AT COMPARABLE LOCATIONS OF A DIE-FORGED COMPONENT AFTER HEAT TREATMENT AT MAXIMUM RULING SECTION OF 2 IN., INVOLVING A BOILING-WATER QUENCH OR A SALT-QUENCH AT 180°C WITH VARIOUS CHARGE/SALT RATIOS

Test Piece Number	*Location*	*Heat-Treatment Involving Boiling-Water Quench*			*Heat-Treatment Involving Salt-Quench 10 min. with Charge/Salt Ratio of 1/230*			*Heat-Treatment Involving Salt-Quench 10 min. with Charge/Salt Ratio of 1/100*			*Heat-Treatment Involving Salt-Quench 10 min. with Charge/Salt Ratio of 1/16*		
		Yield Point (tons/in.²)	*U.T.S. (tons/in.²)*	*Elongation (per cent)*	*Yield Point (tons/in.²)*	*U.T.S. (tons/in.²)*	*Elongation (per cent)*	*Yield Point (tons/in.²)*	*U.T.S. (tons/in.²)*	*Elongation (per cent)*	*Yield Point (tons/in.²)*	*U.T.S. (tons/in.²)*	*Elongation (per cent)*
1	T	32·0	35·5	8·0	26·8	31·6	7·0	25·4	30·1	12·5	25·5	30·8	12·5
2	T	31·2	34·5	8·5	25·2	29·9	7·5	24·3	29·6	8·5	24·6	29·6	12·5
3	S.T.	30·2	32·6	4·0	25·7	30·3	7·0	25·9	30·0	5·5	24·9	29·9	8·0
4	T	29·7	32·6	5·5	25·8	30·6	9·0	24·5	29·4	7·0	23·8	28·8	7·5
5	S.T.	29·4	32·0	3·0	25·8	29·2	3·5	25·6	29·2	5·0	23·6	29·2	5·5
6	L	28·2	32·0	11·0	25·6	30·6	11·0	24·8	29·1	14·0	24·6	29·2	13·5
7	L	28·1	31·8	12·0	24·8	30·1	12·5	25·4	29·7	11·0	24·2	29·0	10·0
8	T	31·8	34·8	10·0	26·8	31·5	11·0	26·5	30·6	10·0	25·6	30·6	13·5
9	T	32·0	34·6	6·5	27·5	31·2	11·0	25·6	30·9	10·0	26·6	31·0	7·0
10	T	30·8	34·3	9·5	26·8	31·1	10·0	24·5	29·6	12·0	25·6	30·6	13·5
11	T	30·4	33·7	13·0	25·5	30·5	13·0	26·2	30·9	14·0	26·9	31·1	11·5
12	T	31·0	34·2	7·0	25·7	30·8	11·5	25·5	30·8	11·0	26·4	31·1	10·0
13	S.T.	30·3	33·0	3·5	25·2	30·0	5·5	25·2	30·0	7·0	25·4	29·6	5·5

T—Transverse
S.T.—Short Transverse
L—Longitudinal

TABLE VI

COMPARISON OF THE TENSILE PROPERTIES OF HIDUMINIUM R.R.77 AND HIDUMINIUM 66

	Hiduminium 66 (*to B.S.S. L.77*) *Heat-Treated with a Quench in Water below 70°C* (*formerly B.S.S. L.65*)				*Hiduminium R.R.77* (*to D.T.D. 5024*) *Heat-Treated with Boiling-Water Quench* (*formerly D.T.D. 683A*)				*Hiduminium R.R.77* *Newly Developed Heat Treatment Involving Step-Quenching in Molten Salt at 180°C* (2 *in. maximum section*)			
	0·1% *P.S.* (*tons/in.²*)	*Yield Point* (*tons/in.²*)	*U.T.S.* (*tons/in.²*)	*Elongation* (*per cent*)	0·1% *P.S.* (*tons/in.²*)	*Yield Point* (*tons/in.²*)	*U.T.S.* (*tons/in.²*)	*Elongation* (*per cent*)	0·1% *P.S.* (*tons/in.²*)	*Yield Point* (*tons/in.²*)	*U.T.S.* (*tons/in.²*)	*Elongation* (*per cent*)
Minimum design properties:—												
Transverse	—	23	26	4	—	25	29	4	—	21·5*	27·5*	4*
Longitudinal	—	25	29	6	—	27	31	8	—	23 *	29 *	8*
Typical values (1¼ in. diameter forged bar)	27	—	31	10	28	—	33	12	27	—	32	14
Specification values (1¼ in. diameter forged test bar)	25	—	29	8	27	—	32	7	26*	—	31 *	8*

*Tentative values only.

heat treated with a boiling-water quench being given for comparison. Although the level of strength for salt-quenched components is about 3 tons/in.^{2} lower than for boiling-water quenching, this level is not affected by the size of the charge, within the limits investigated.

3.6. Minimum Design Values for Components

Before consideration may be given to the selection of material for production components it is necessary to determine the minimum levels of properties, within a given size range, using the newly developed salt-quench heat treatment.

A series of die-forged components, heat treated at a maximum ruling section of 2 in., have been tested and the results have been used to establish tentative minimum design values. These minima are given in Table VI, the guaranteed properties[15] for Hiduminium R.R.77 to Specification D.T.D.683A and Hiduminium 66 to Specification B.S. L.65 being included for comparison. Although the proposed values for salt-quenched Hiduminium R.R.77 are lower than those guaranteed for the same alloy quenched in boiling water, the ultimate tensile strength and elongation values are slightly superior to those of Hiduminium 66. Since the ratio of 0·1 per cent proof stress to ultimate tensile stress of these materials is normally greater than 75 per cent, designs based on the usual criterion of 4/3 proof stress or ultimate tensile stress, whichever is the lower, will depend on the ultimate tensile stress values. In the present case, therefore, salt-quenched Hiduminium R.R.77 has higher design properties than Hiduminium 66 to B.S.S. L.65.

3.7. The Effect of Salt-Quench Heat Treatment on the Fatigue Properties of Forged Bar and Hand-Forged Slab

In considering a high strength aluminium alloy for structural applications, an aircraft designer requires a knowledge of the fatigue resistance of the material, together with an assessment of its notch sensitivity, this latter factor being of great importance when the applied stress is transverse to the direction of grain flow. In order to compare the fatigue resistance and notch sensitivity of Hiduminium R.R.77, heat-treated by processes involving either a boiling-water quench or a quench into salt at 180°C, fatigue tests were carried out on sections cut from the short transverse direction from a hand-forged slab which had been manipulated so as to have marked directionality, and from the longitudinal direction of 2 in. diameter forged bar.

The forged slab, of dimensions 4 in. × 8 in. × 33 in., was cut into blanks of 2 in. × 2 in. × 4 in. before heat treatment, these blanks providing either a tensile test piece or four fatigue specimens, while the 2 in. diameter forged bar, manufactured from machine cast ingot, was cut into 6 in. lengths for heat treatment. Sections of the forged slab cut from the short transverse direction were selected for tensile testing, to determine the consistency of the material across the block examined, but fatigue tests were taken at random from the available material.

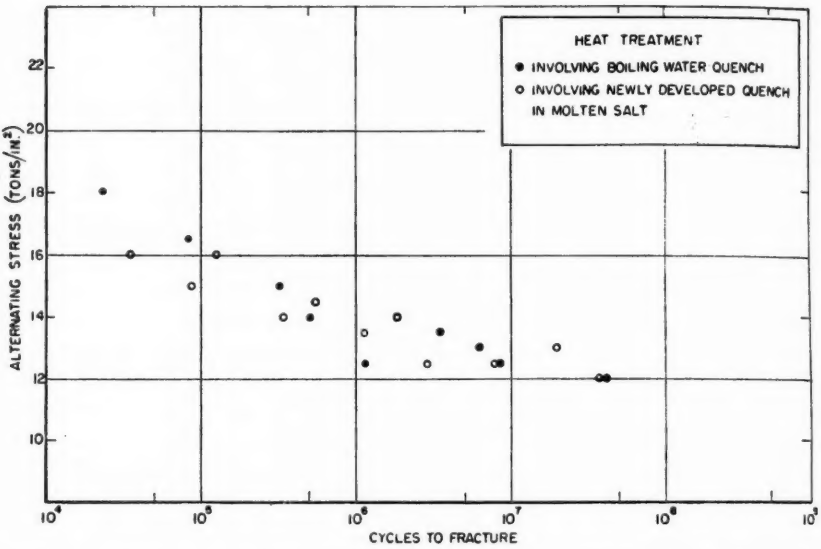

FIGURE 5. Fatigue tests at room temperature (Haigh type). Hiduminium R.R.77 (forged block). Short transverse, plain specimens. Static stress zero tons/in.²

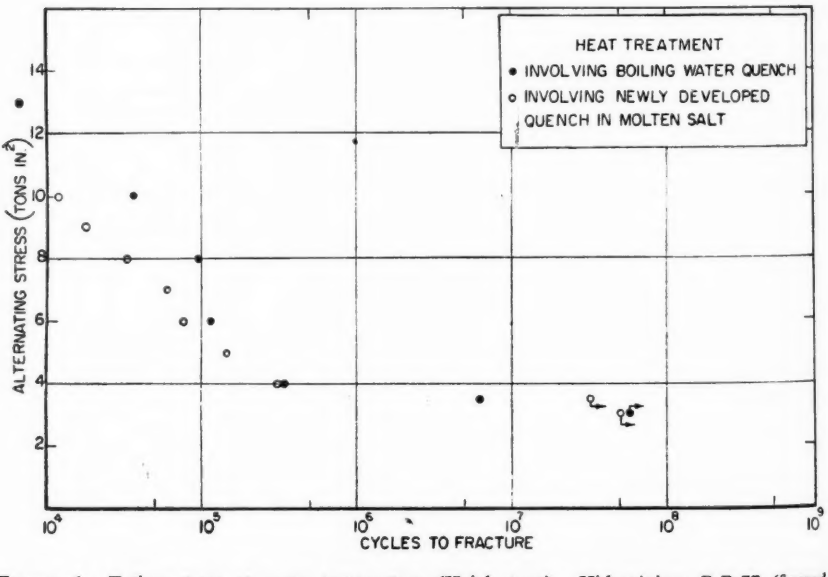

FIGURE 6. Fatigue tests at room temperature (Haigh type). Hiduminium R.R.77 (forged block). Short transverse, V notch specimens. Static stress zero tons/in.²

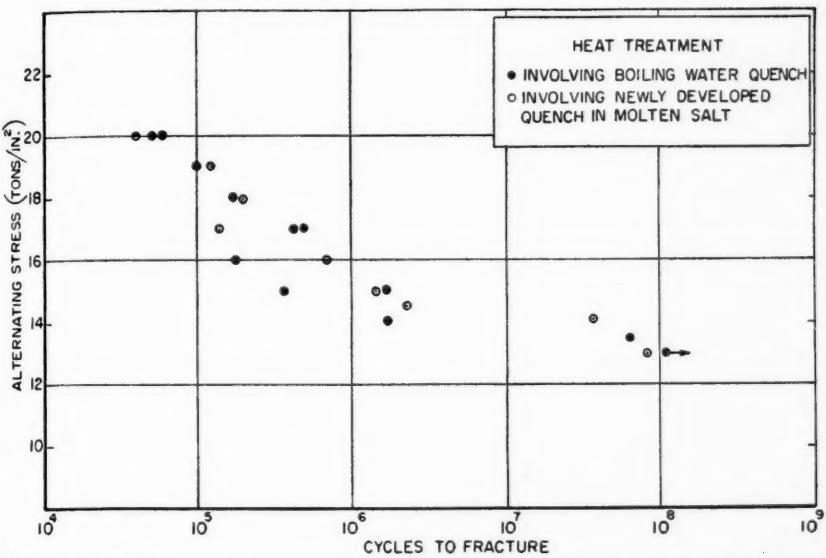

FIGURE 7. Fatigue tests at room temperature (Rolls-Royce type). Hiduminium R.R.77 (forged bar, 2 in. diameter). Longitudinal, plain specimens. Static stress zero tons/in.²

Fatigue tests were carried out at room temperature on material from the forged slab, under conditions of direct stress, with a static mean zero, in Haigh type fatigue machines running at approximately 6,000 cycles per minute, using either plain specimens of 0·226 in. diameter or specimens having a 60° V notch, with a root radius of 0·004 in. and a depth of 0·008 in. (theoretical stress concentration factor 3·4), cut circumferentially, so that the diameter of the specimen at the base of the notch was the same as that used for plain test pieces. The tests on forged bar were carried out on test pieces of 0·160 in. diameter under conditions of rotating-cantilever fatigue in Rolls-Royce type machines running at 4,000 revolutions per minute.

The results of the fatigue tests on sections of forged slab are plotted on diagrams of stress against log-endurance in Figs. 5 and 6. Although some degree of scatter exists in the results, it is considered that there is no significant difference in the fatigue behaviour of Hiduminium R.R.77 heat treated with a boiling-water quench or by a process involving an interrupted quench into molten salt at 180°C, a result confirmed by longitudinal tests from forged bar (Fig. 7).

3.8. The Effect of Variation in Artificial Ageing

All work concerned with the establishment of atmospheric stress-corrosion resistance, tensile and fatigue properties of Hiduminium R.R.77, heat treated by the process involving a quench into molten salt at 180°C, had been done on material given the standard ageing treatment of 12 hours at 135°C.

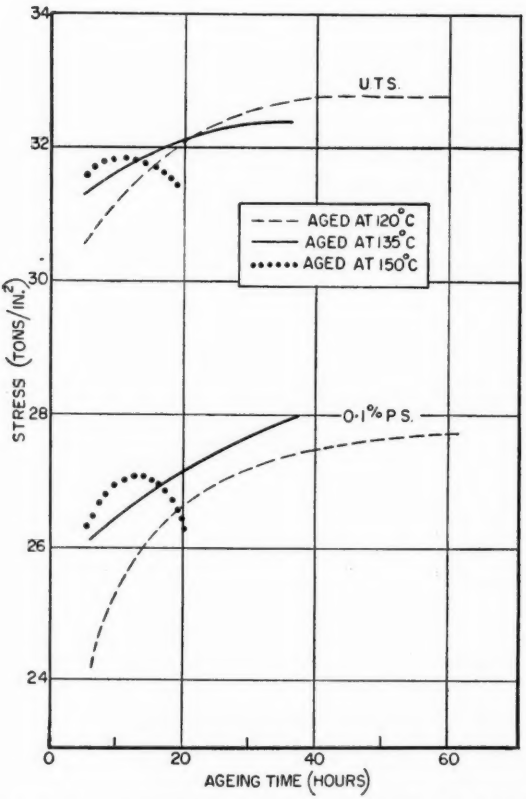

FIGURE 8. Tensile tests at room temperature on Hiduminium R.R.77 forged bar heat-treated by process involving quenching into molten salt at 180°C.

To determine whether this treatment gave optimum properties, a series of lengths of forged bar were solution treated and subjected to differing precipitation treatments. The results of the tensile tests on the forged bar are shown in Fig. 8 and it is evident that, for material heat treated with a salt quench, the tensile strength is increased by increasing time of ageing at 135°C. Raising the ageing temperature from 135°C to 150°C but keeping the time of ageing at 12 hours produces some increase of tensile properties. Alternatively, the tensile properties are increased if the time of ageing at 120°C is extended. The limitations and requirements of production heat treatment schedules would favour as short an ageing period as possible, concomitant with the maintenance of mechanical properties.

To provide a fairly rapid assessment of the possible beneficial effect of modified ageing on the proposed minimum design properties, a series of die-forged components, selected within the size range up to 3 in. thick, were heat treated, identical

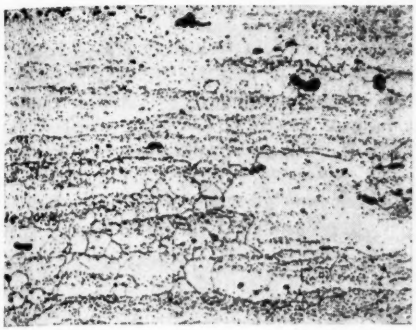

FIGURE 9. Hiduminium R.R.77, heat treated with boiling-water quench (×500).

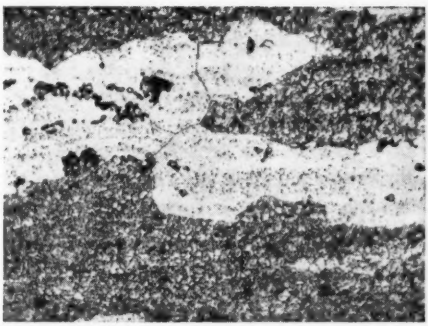

FIGURE 10. Hiduminium R.R.77, heat treated by quenching into molten salt at 180°C (×500).

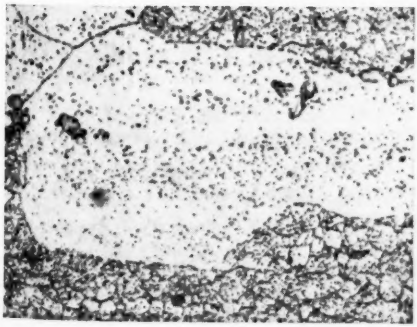

FIGURE 11. Large field of central portion of Fig. 10 (×1250).

components being aged for 12 or 36 hours at 135°C and 12 hours 150°C. The results of cut-up testing showed that the latter treatment produced no significant increase in level of tensile strength, whereas the increased ageing at 135°C produced an increase of 1 ton/in.^{2} in both proof stress and ultimate tensile strength for all size ranges. Additional work is proceeding to establish atmospheric stress-corrosion resistance but, to date, no decrease in comparison with the 12 hours 135°C treatment has been found. Fatigue tests on sections from forged components indicate no significant difference in fatigue behaviour for either 12 or 36 hours at 135°C

3.9. Metallographic Examination

The photomicrographs of Figs. 9 and 10 show representative structures for Hiduminium R.R.77, quenched in boiling water and molten salt at 180°C, respectively, obtained after etching in 25 per cent nitric acid at 70°C for three minutes.

It may be seen that the structure of the boiling-water-quenched material consists of mixed fine and coarse grains with a banded precipitate. The salt-quenched material shows areas of large grains with a more general precipitate, together with more heavily precipitated regions of a fine crystalline or sub-grain structure. Fig. 11 shows the central area of Fig. 10 at a higher magnification, in which this effect can clearly be seen.

Additional metallographic investigations, including electron micrography, are being undertaken in order to study this phenomenon in greater detail.

4. Discussion of Results

The comparison of the stress-corrosion resistance of medium and high strength aluminium alloys in the form of large hand-forged slabs, carried out by means of atmospheric stress-corrosion tests in four-point bending, has shown that the susceptibility to failure of aluminium-zinc-magnesium-copper alloys in the short transverse direction may not be reduced with certainty by the addition of chromium, even though the presence of this element had been shown to benefit the stress-corrosion resistance of similar alloys in the form of sheet and plate.

With forged material, heat treated at moderate section thickness, the addition of chromium produced a quench-sensitive alloy, the level of tensile strength varying both with section thickness and quench temperature following the solution treatment. Thus, the addition of 0·2 per cent chromium to Hiduminium R.R.77, having a nominal manganese content of 0·5 per cent, produced an alloy of low tensile strength, under the quench conditions used, although the stress-corrosion resistance was reasonable. Reduction in manganese, together with a chromium addition, maintained the tensile strength after heat treatment but the stress-corrosion properties were low.

Examination of the effects of modified quench condition, assessed on Hiduminium R.R.77, has shown that a marked increase in the resistance of aluminium-zinc-magnesium-copper alloys can be achieved by the use of step-quenching employing an intermediate salt bath at 180°C. However, the slow rate of cooling from the solution-treatment temperature produces a reduction in tensile strength obtained on subsequent ageing. For section thicknesses up to 2 in., the level of strength obtained after precipitation for 12 hours at 135°C is considered to be sufficiently high for aircraft applications.

The measured tensile properties of forged bar of 2 in. diameter, or less, lies between the requirements of Specification B.S. L.77 (formerly B.S.S. L.65) and Specification D.T.D.5024 (formerly D.T.D.683A) having a tentative minimum value

of 26 tons/in.^{2} proof stress, 31 tons/in.^{2} ultimate tensile strength and 8 per cent elongation.

Minimum design figures, estimated from the results of tensile tests carried out on sections cut from a series of die-forged components, approximated to those guaranteed for Hiduminium 66 (B.S.S. L.65), being slightly inferior in the case of yield stress. However, based on the conventional design criterion of 4/3 proof stress or ultimate tensile stress, whichever is the lower, the salt-quenched Hiduminium R.R.77 has the higher design strength and additional work has indicated that the minimum design values are increased by the use of 36 hours ageing at 135°C.

The results of fatigue tests on sections of large forged slab, or forged bar, have indicated that there is little difference in fatigue resistance of Hiduminium R.R.77 heat treated with either a boiling-water quench or a step-quench into molten salt at 180°C. An assessment of the levels of residual stress in die-forgings, carried out by a measurement of machining distortion and cut-up testing using strain gauges, has shown that, while the use of a boiling-water quench reduces the levels of residual stress, in the case of Hiduminium R.R.77, the lowest levels are obtained in those components heat treated by the salt-quench process.

5. Conclusions

It is concluded that the atmospheric stress-corrosion resistance of large hand-forged slabs in Al-Zn-Mg-Cu alloys, assessed by four-point bending tests in the short transverse direction, may not be improved with certainty by compositional modifications involving chromium and manganese. Comparable short transverse tests on an Al-Cu-Mg alloy to B.S.S. L.65 have indicated that this material can also exhibit a variable resistance to atmospheric stress corrosion.

However, modified quench procedures have been shown to be very beneficial in the case of one type of alloy to D.T.D.683A, Hiduminium R.R.77, and a step-quench, involving an intermediate molten salt bath at 180°C, has proved most effective in practically eliminating the tendency of this alloy to atmospheric stress-corrosion cracking. Although this process produces a decrease in the tensile strength, at a maximum ruling section of 2 in. at the heat treatment stage, the tentative guaranteed minimum design properties for forgings are comparable with those quoted for Hiduminium 66 (B.S.S. L.65) although slightly inferior to those of Hiduminium R.R.77 (D.T.D.683A) using the current standard heat treatment involving a boiling-water quench.

ACKNOWLEDGMENT

The authors wish to thank the Directors of High Duty Alloys Limited for permission to publish this paper.

REFERENCES

1. ROSENHAIN, W., ARCHBUTT, S. L. and HANSON, D. Eleventh Report to the Alloys Research Committee: On Some Alloys of Aluminium (Light Alloys). *Institution of Mechanical Engineers*, 1921.

2. SANDER, W. and MEISSNER, K. L. The Influence of the Compound $MgZn_2$ on the Workability of Aluminium Alloys. (In German). *Zeitschrift für unorganische Chemie*, Vol. 154, p. 144, 1926

3. BRADBURY, T. F. A New Aluminium Alloy. BP.476, 930.

4. BRADBURY, T. F. and WARRINGTON, H. G. Improvements Relating to Extruded Aluminium Base Alloys. BP.601, 813.

5. DIX, E. H. Aluminium-Zinc-Magnesium Alloys: Their Development and Commercial Production. *Transactions of the American Society for Metals*, Vol. 42, p. 1057, 1950.

6. CHADWICK, R., MUIR, N. B. and GRAINGER, H. B. Stress-Corrosion of Wrought Ternary and Complex Alloys of the Aluminium-Zinc-Magnesium System. *Journal of the Institute of Metals*, Vol. 85, p. 161, 1957.

7. PERRYMAN, E. C. W. and BLADE, J. C. Relationship Between the Ageing and Stress-Corrosion Properties of Aluminium-Zinc Alloys. *Journal of the Institute of Metals*, Vol. 77, p. 263, 1950.

8. PERRYMAN, E. C. W. Intercrystalline Cracking of Aluminium-Zinc Alloys. (In French). *Comptes Rend.*, Vol. 235, p. 884, 1952.

9. HARDY, H. K. Modern Descriptive Theories of Precipitation Processes. *Journal of the Institute of Metals*, Vol. 75, p. 707, 1949.

10. British Intelligence Objectives Sub-Committee. High Strength Aluminium-Zinc-Magnesium Alloy Development in Germany. B.I.O.S. Final Report No. 1770, Item No. 21.

11. MEIKLE G. and LEWIS, D. The Atmospheric Stress-Corrosion of Aluminium-Zinc-Magnesium Type Alloys. R.A.E. Report No. Met. 88, October 1955.

12. FINK, W. L. and WILLEY, L. A. Quenching of 75S Aluminium Alloy. *Metals Technology*, Vol. 14, No. 5, Technical Publication No. 2225, 1947.

13. WILSON, C. Quenching Conditions. *Aircraft Production*, Vol. 17, p. 72, 1955.

14. EDMUNDS, W. T. and LLOYD, R. C. The Production of Light-Alloy Drop-Forgings, Their Heat Treatment, Inspection and Testing. Institute of Metals Monograph and Report Series No. 17: 1955-59.

15. High Duty Alloys Limited. *Hiduminium Technical Data*, 1958.

Notes on Thin Wing Theory at Low Supersonic Speeds

PART II. A Unified Numerical Method for the Calculation of the Loading on Wings with Subsonic Leading Edges

G. J. HANCOCK

(*Queen Mary College, University of London*)

8. Introduction to Part II

The main advantage of the method presented in Part I of this paper is the generality with regard to the shape of the wing plan form. This is a welcome innovation in the field of supersonic wing theory, where methods of solution of the usual lifting problem are restricted to a limited number of wing shapes. Most of the lifting characteristics of wings are now known at supersonic speeds, but the range of wings with curved subsonic leading and trailing edges needs further investigations. Therefore it seems that the extension of the design problem to include these lifting problems is a useful addition to the extensive literature on the subject.

Mathematically, the inversion of the design problem in Part I is simple. The incidence distribution, given at a series of discrete points on the wing surface, has been specified in terms of the discontinuity in the velocity potential, also at a series of discrete points, so that there is, effectively, a matrix equation between these two functions. The inversion of the influencing matrix leads to the determination of an unknown velocity potential distribution from a known incidence distribution. In the notation given in Part I, the relevant equations are equations (9) and (10), which state that

$$\gamma_{k,l}=4d \sum_{\substack{i=0,\ldots k \\ j=0,\ldots l}} A_{(i,j)(k,l)}\,\phi_{i,j}, \qquad (15)$$

where $A_{(i,j)(k,l)}$ are tabulated coefficients (Appendix to Part I), and

$$\alpha_{k,l}=\frac{M}{\pi V d^2}(\gamma_{k,l}+\gamma_{k-1,l-1}-\gamma_{k-1,l}-\gamma_{k,l-1}). \qquad (16)$$

Received June 1958. Part I was published in August 1959.

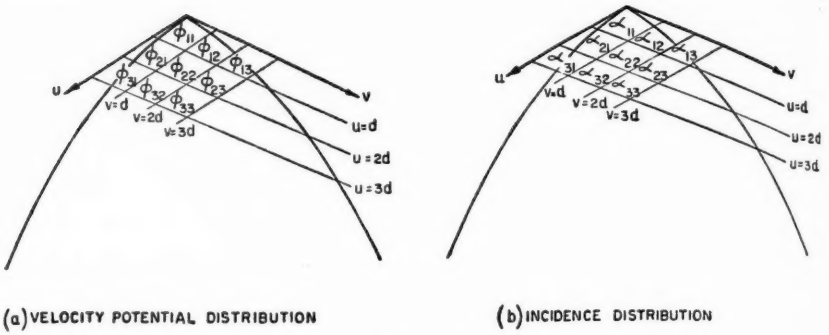

(a) VELOCITY POTENTIAL DISTRIBUTION (b) INCIDENCE DISTRIBUTION

FIGURE 16.

Combining (15) and (16),

$$\alpha_{k,\,l} = \sum_{\substack{i=0,\ldots k \\ j=0,\ldots l}} B_{(i,\,j)(k,\,l)}\,\phi_{i,\,j}, \qquad \ldots\ldots \quad (17)$$

which in effect defines the influence coefficients $B_{(i,\,j)(k,\,l)}$. This is a matrix equation which needs inverting for $\phi_{i,\,j}$ in terms of $\alpha_{k,\,l}$. The calculation of the coefficients $B_{(i,\,j)(k,\,l)}$ is straightforward, allowing for the leading edge approximations, as in Part I, where applicable.

However this approach may be modified to a more direct method by a consideration of the physical interpretations of equations (15), (16) and (17). Consider, for example, the diagrams in Fig. 16.

Ignoring any leading edge approximations for the present, in order to illustrate the fundamental points, the diagrams show the general distribution of velocity potential and incidence in the present notation. Thus, working aft of the wing apex:—

(*i*) α_{11} is directly proportional to ϕ_{11} by equation (17); hence, for a given α_{11}, ϕ_{11} can be determined.

(*ii*) α_{12} depends on ϕ_{11} and ϕ_{12}; therefore, for a given value of α_{12}, ϕ_{12} can be found, since ϕ_{11} is known from (*i*).

(*iii*) Assuming symmetry, *i.e.* $\alpha_{i,\,j} = \alpha_{j,\,i}$ (this condition is not necessary for the application of this technique), α_{22} depends on ϕ_{11}, ϕ_{12}, ϕ_{21}, and ϕ_{22}; therefore, for a given α_{22}, ϕ_{22} can be calculated with the values of ϕ_{11} and ϕ_{12} determined from (*i*) and (*ii*).

Therefore it is possible to work aft over the wing surface in this fashion. This technique is completely general, since all reference points remain on the wing surface. It can be applied to subsonic trailing edges, remembering that ϕ is independent of the streamwise co-ordinate aft of the trailing edge.

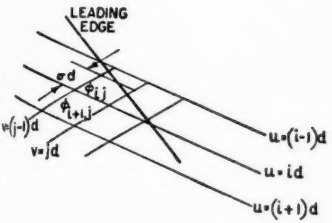

FIGURE 17. Notation for area at the leading edge.

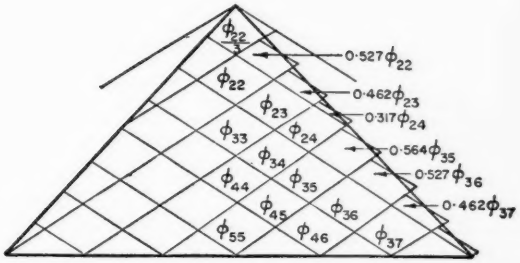

FIGURE 18. Mesh system for velocity potential used in the example.

9. Numerical Technique

As before the main difficulties arise at the edges where singularities are expected, *i.e.* the leading edges and wing tips. It is advisable not to attempt to determine the velocity potential too close to these boundaries. The author assumed that ϕ tends to zero as $\delta^{1/2}$ (where δ is the distance from the edges), as in the normal case. Thus the potential of a sub-area $\phi_{i,j}$ affected by a leading edge, say, is related to the value of its neighbouring area by the formula

$$\phi_{i,j}=\phi_{i+1,j}\left(\frac{\sigma/2}{\sigma+\frac{1}{2}}\right)^{1/2}, \qquad . \quad . \quad . \quad . \quad . \quad (18)$$

where the notation is shown in Fig. 17.

This assumption implies that only the incidence $\alpha_{i+1,j}$ need be satisfied; the incidence $\alpha_{i,j}$ is ignored. This is further justified because of the inaccuracies in averaging incidences near the leading edge, where large upwash velocities are theoretically forecast just ahead of the wing.

The final point before the onset of computation is the assumption for the apex area, where the extension of the foregoing ideas to an area affected by two leading edges is difficult to envisage. The author assumed that flat plate conditions exist near the apex for the size of mesh considered, so that

$$\phi_{11}=\tfrac{1}{3}\phi_{22}. \qquad . \quad . \quad . \quad . \quad . \quad (19)$$

10. Application to a Thin Symmetrical Delta Wing

The mesh system chosen for this example is indicated in Fig. 18, showing the unknown function ϕ with the modified leading edge conditions. Only half the wing characteristics are shown, since there is symmetry about the centre chord ($\phi_{ij}=\phi_{ji}$).

The author adopted the following procedure, using both sets of tables of $A_{(i,j)(k,l)}$ presented in the Appendix to Part I.

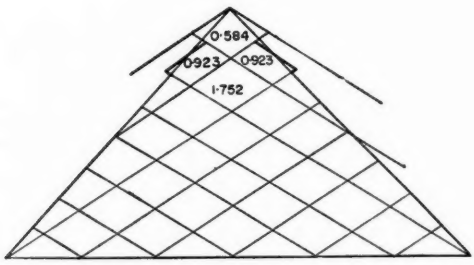

FIGURE 19. Values of ϕ/K.

(*i*) A table of the set of values of γ is calculated, defined by equation (15). To start with

$$\gamma_{11}=\boxed{\frac{\quad}{4d\,(\phi_{22}/3)}} \qquad \gamma_{12}=\boxed{\frac{\quad}{4d\,(0{\cdot}5547\,\phi_{22})}}$$

$$\gamma_{22}=\boxed{\frac{\quad}{4d\,(1{\cdot}346\,\phi_{22})}}$$

BLOCK 1

Applying equation (16),

$$\gamma_{22}+\gamma_{11}-2\gamma_{12}=\frac{\alpha\pi V d^2}{M}=4dK,$$

where α is the constant incidence over the wing, and K is the constant defined by the equation

$$K=\frac{\alpha\pi V d}{4M}.$$

Therefore $\phi_{22}=1{\cdot}752\,K.$

Next this value is substituted in Block 1, forming Block 2:—

$$\gamma_{11}=\boxed{\frac{0{\cdot}584\,K}{4d\,(\phi_{22}/3)}} \qquad \gamma_{12}=\boxed{\frac{0{\cdot}9718\,K}{4d\,(0{\cdot}5547\,\phi_{22})}}$$

$$\gamma_{22}=\boxed{\frac{2{\cdot}3596\,K}{4d\,(1{\cdot}346\,\phi_{22})}}$$

BLOCK 2

Also the value of ϕ_{22} can now be substituted in an open mesh diagram, as in Fig. 19.

(*ii*) The process is continued with the calculation of γ_{13} and γ_{23} by reference to Figs. 18 and 19. Block 2 is now extended, as shown in Block 3.

$$\gamma_{11}=\frac{0{\cdot}584\,K}{4d\,(\phi_{22}/3)} \qquad \gamma_{12}=\frac{0{\cdot}9718\,K}{4d\,(0{\cdot}5547\,\phi_{22})}$$

$$\gamma_{22}=\frac{2{\cdot}3596\,K}{4d\,(1{\cdot}346\,\phi_{22})} \qquad \gamma_{13}=\frac{\quad}{4d\,(0{\cdot}2829\,\phi_{23}+0{\cdot}4880\,K)}$$

$$\gamma_{23}=\frac{\quad}{4d\,(1{\cdot}0797\,\phi_{23}+1{\cdot}091\,K)}$$

BLOCK 3

Since
$$\gamma_{12}+\gamma_{23}-\gamma_{22}-\gamma_{13}=\frac{\alpha\pi Vd^2}{M}=4dK,$$

then
$$\phi_{23}=2{\cdot}240\,K.$$

Hence γ_{23} and γ_{13} can be calculated in terms of K and Block 3 completed. Fig. 19 can be extended to include ϕ_{23}, as shown in Fig. 20.

(*iii*) From Figs. 18 and 20, Block 3 can now be extended to include γ_{33}, where

$$\gamma_{33}=\frac{\quad}{4d\,(\phi_{33}+2{\cdot}6354\,K)}.$$

Since
$$\gamma_{33}+\gamma_{22}-2\gamma_{23}=4dK,$$

then
$$\phi_{33}=3{\cdot}024\,K.$$

Therefore γ_{33} can be calculated in terms of K and ϕ_{33} included in Fig. 20.

In this way the mesh can be completed. The steps (*i*), (*ii*) and (*iii*) can be combined to the formation of a single table of γ_{ij}, filling in consecutive values of ϕ_{ij} into the mesh system, as in the derivation of Fig. 20.

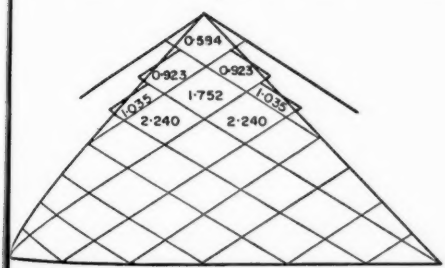

FIGURE 20. Values of ϕ/K.

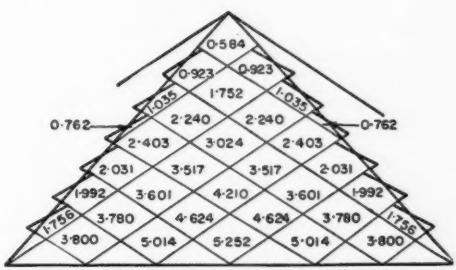

FIGURE 21. Values of $\phi/K\equiv\phi(4M)/(\alpha\pi Vd)$, where $d=0{\cdot}194\,c_0$ and c_0 is the centre chord.

TABLE I

VALUES OF γ_{ij}

Note: The factors K in the upper half and $4d$ in the lower half of each expression have been omitted for ease of tabulation, but must be included in their application.

0·584					
$\phi_{22}/3$					
	0·9718				
	0·5547 ϕ_{22}				
2·3594		1·1217			
1·346 ϕ_{22}		0·2829 ϕ_{23} + 0·4880			
	3·5096				
	1·0797 ϕ_{23} + 1·0911		0·1121 ϕ_{24} + 0·6510		
5·6596		4·3078			
ϕ_{33} + 2·6354		1·0192 ϕ_{24} + 1·8587			
	7·4576		4·4138		
	ϕ_{34} + 3·9406		0·5276 ϕ_{35} + 2·5139		
10·2560		8·5636		4·4260	
ϕ_{44} + 6·0460		1·2083 ϕ_{35} + 4·2125		0·4166 ϕ_{36} + 2·8513	
	12·3620		9·5760		
	ϕ_{45} + 7·7329		1·1448 ϕ_{36} + 5·2487		0·2829 ϕ_{37} + 3·0630
ϕ_{55} + 10·2160		ϕ_{46} + 9·3601		1·0797 ϕ_{37} + 6·1862	

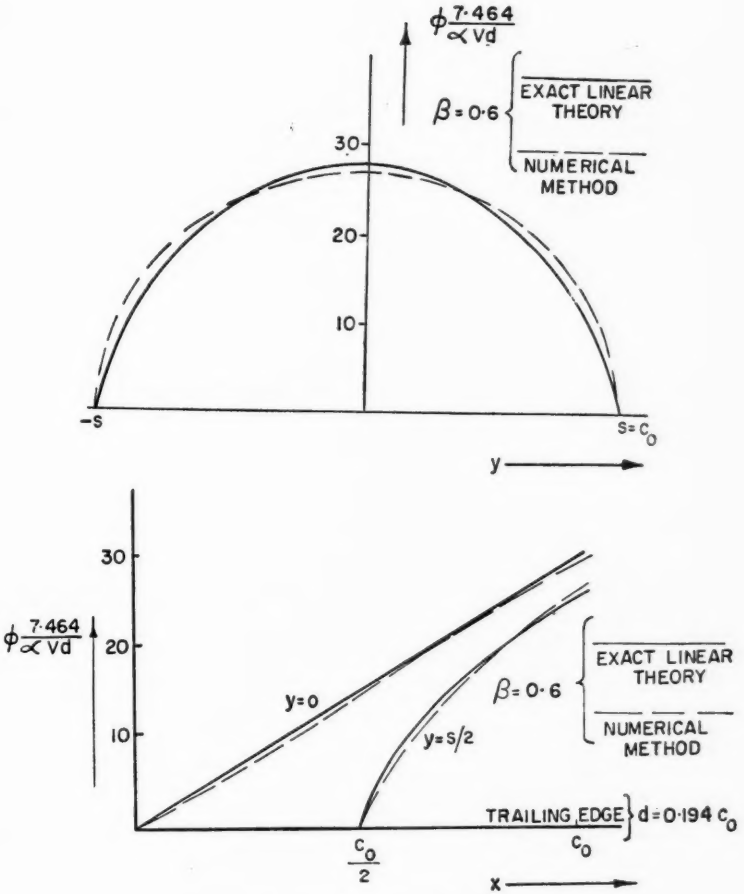

FIGURE 22. Variation of velocity potential.

The final set of values of γ_{ij} is shown in Table I, with distribution of the velocity potential ϕ_{ij} in Fig. 21.

It is seen by the comparison with exact linearised theory in Fig. 22 that, with a relatively wide mesh, the accuracy is within acceptable bounds. The lift distribution, given by ϕ at the trailing edge, is of the order of 3 per cent error. It is suggested that the pressure loading distribution $\partial\phi/\partial x$ can be obtained by interpolation of the $\phi(x)$ curve.

The numerical method described is completely general for wings with subsonic leading edges, for any camber and trailing edge conditions. The necessary computation is not excessive and can easily be accommodated on a desk machine.

The Stress Concentration Factors in Cylindrical Tubes with Transverse Circular Holes

H. T. JESSOP, C. SNELL and I. M. ALLISON

(*Department of Civil and Municipal Engineering, University College, London*)

SUMMARY: The "frozen stress" techniques of photoelasticity can give a complete knowledge of the stress system in a solid body, but the examination of the stresses requires more time and care than in corresponding flat plate tests. In tests on tubes with transverse circular holes, sponsored by The Royal Aeronautical Society, all practicable geometrical shapes are examined and the maximum stress is measured in tension, bending and torsion. The results are comprehensive and show the inadequacy of previous results. In all cases the maximum stress occurs inside the bore of the hole. The accuracy of all the graphs of stress concentration factors is better than five per cent.

1. Introduction

Cylindrical tubes are a common feature in aircraft frames and it is frequently necessary to provide transverse holes in tubular components which may be subjected to high loads. A certain amount of information is available on the stress concentration factors (S.C.F.) in solid cylindrical rods with transverse holes, but this is incomplete and there appears to be no information at all upon the stress concentration in tubes.

This investigation was initiated by the Structures Committee of The Royal Aeronautical Society, to obtain systematic data on the stress concentrations in such tubes over the complete range of wall thickness of tube and diameter of transverse hole which would be likely to occur in practice. The tests covered this range of models for three types of applied load: torsion, axial load and bending.

The problem is essentially a "three-dimensional" one, and was approached by the now well established stress-freezing photoelastic method.

Received October 1958.

NOTATION

D_O outside diameter of tube

D_I inside diameter of tube

d diametral hole diameter

x, y, z Cartesian axes

x axis of the diametral hole

z cylindrical tube axis

P, Q, R principal stresses

p, q, r directions of the principal stresses P, Q and R

f_{max} maximum value of the principal stress in the component

f_a mean peripheral boundary stress through a slice A of thickness t_a

f_b mean peripheral boundary stress through a slice B of thickness t_b

$f_{b\,mean}$ mean value of f_b over the range 0 to t_a

$f_{b\,max}$ maximum value of f_b

} *See* Figs. 2 and 3.

σ density of the shaft material

f fringe value of the photoelastic material

For convenience the stress concentration factors are based on the gross cross section. The factor K used throughout this paper is defined as

$$K = \frac{\text{peak stress in the component}}{\text{maximum stress in the undrilled tube}}.$$

For comparison with other work it is necessary to refer to factors based on the net or reduced area of cross section. In all cases this factor will be defined as K_{net}.

2. Method of Tests

2.1. General

The range of models used is shown in Table I.

TABLE I

THE PHOTOELASTIC TEST MODELS

	$d/D_O = 0{\cdot}05$	0·1	0·2	0·3	0·4
$D_I/D_O = 0$	×	×	×	×	×
0·4	×		×		×
0·6		×		×	
0·8	×	×	×		×
0·9	×	×	×	×	×

The models were machined from castings of Araldite B, hot-setting resin, annealing being carried out both before and after machining. An accuracy of $\pm 0{\cdot}002$ in. was maintained in the dimensions of the models and the initial casting stress was never permitted to exceed one fringe per inch (*i.e.* about 3 per cent of the peak stresses).

The model dimensions were 1·5 in. outside diameter by 8 in. long, except for models having a D_I/D_O ratio greater than 0·8, when the outside diameter was increased to 2 in.

A special loading frame was designed in which the models could be subjected to tension, compression, bending or torsion.

After "freezing" the necessary slices were cut from the models and placed in immersion fluid for examination in a standard photoelastic bench. Since the peak stress occurred on a free boundary in all cases, the method adopted was that of measuring the stress difference at a number of points in a slice and using a graphical extrapolation to the point of highest stress on the boundary. The extrapolation method is necessary because of the difficulty in locating the "fringe" on the extreme boundary. The presence of a "time-edge stress," owing to the absorption of water in the surface of the photoelastic model, further complicated the measurement of the boundary stress. Optical measurements were made by the Senarmont method, which gave the boundary stress to an accuracy of 0·5 fringes per inch, while the position of points on the model was measured with a travelling microscope to an accuracy of $\pm 0{\cdot}001$ in. The measurements were made to within 0·005 in. of a boundary and the extrapolation over this distance is estimated to give an overall

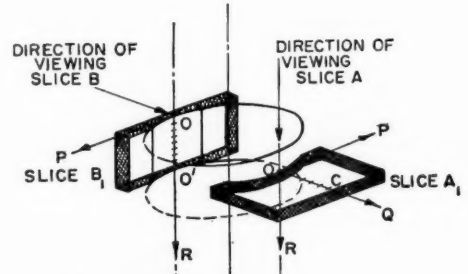

FIGURE 1. Slices for "Improvement" method.

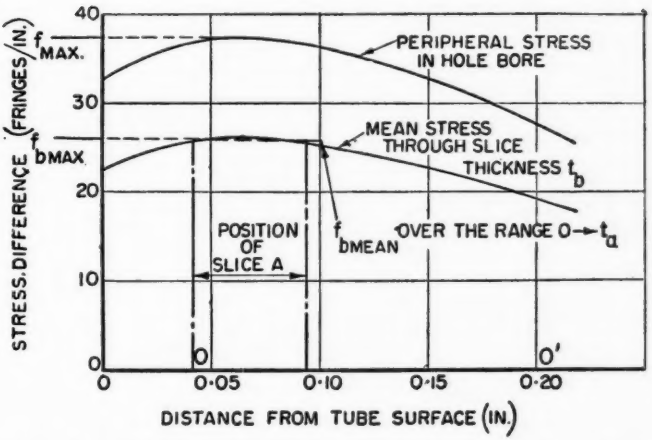

FIGURE 2. Mean stress difference $P-R$ through Slice B at points along OO.

accuracy in the S.C.F. of between ±5 per cent for large diametral holes, and ±7 per cent for small diametral holes.

2.2. Peak Stress Measurement in Cylindrical Tubes

Any cylindrical surface co-axial with the tube cuts the diametral hole in a curve which is not a plane curve. At any point on this curve the principal stresses are found to be P, tangential to the curve, Q in the direction of the radius vector from the diametral hole axis and therefore normal to the curve, and R normal to the plane containing the radius vector and the tangent to the curve (*see* Fig. 6).

It was found, in agreement with previous measurements by Thum and Kirmser[1], that the peak stress in the cylindrical tube (P in the notation just given) occurs in the bore of the diametral hole just below the tube surface, and that there is a variation in peripheral stress as the peak is approached in any direction on the surface of the hole bore. The stress difference $P-R$ changes slowly in direction x, while the difference $P-Q$ changes extremely rapidly as the diametral hole boundary is approached in the radial direction OC (Fig. 1). It is clear that any satisfactory attempt to measure the peak peripheral stress must be carried out by viewing in direction x, since this will lead to measurement, through a thin slice, of mean $P-Q$ values which are close to the peak values. The method of examination finally adopted depends on the improvement of the mean peripheral stress measured through a slice of appreciable thickness, using a knowledge of the variation in stress through the slice.

Two distinct slices are required (Fig. 1), the plane of one (Slice B) being tangential to the diametral hole boundary at the point of concentration. The other slice (Slice A) is in general a singly-curved slice containing the P-direction. To

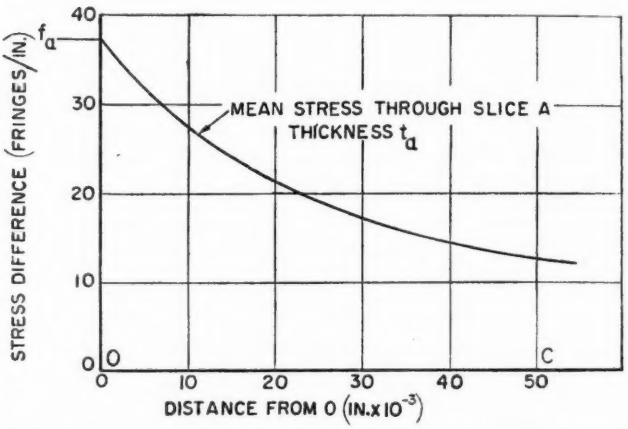

FIGURE 3. Mean stress difference $P-Q$ through Slice A at points along OC.

simplify the measurements and the production of slices, the slices A are cut differently for each of the three loading conditions investigated. Detailed descriptions of the slicing are given in the separate sections on torsion, tension and bending (Sections 3, 4, 5). For descriptive purposes the general case of a stress concentration occurring on a concave singly-curved surface is considered.

Senarmont observations of relative retardation are made through Slice B (approximately 0·030 in. thick) at a series of points along OO' (Fig. 1). The results are plotted as fringes per inch against distance from O, in order to ascertain the position of the peak peripheral stress (Fig. 2). Slice A (approximately 0·040 in. thick) is then cut so that it embraces the peak observed in Slice B. A microscope traverse is set up to pass through O, the peak of the stress concentration, and measurements of relative retardation are made at intervals along OC. The results are plotted as fringes per inch against distance from O, for a distance of 0·05 in. The curve of mean $(P-Q)$ through the slice is extrapolated to the boundary to obtain f_a, the mean peripheral boundary stress through a slice of thickness t_a (Fig. 3).

Examination of slices taken in the xr-plane indicates that, even with thick-walled tubes, the R stress is negligible over the range OO', being of the order of one fringe per inch (the same as the casting stress permitted). Thus, the $(P-R)$ curve may be taken as the mean peripheral stress (f_b) through a thickness t_b of Slice B. Assuming that the form of the variation in peripheral stress at the hole boundary along the line OO' is the same as the mean stress difference along OO', the maximum value of peripheral stress in the hole bore is

$$f_{max} = f_a \times \frac{f_{b\,max}}{f_{b\,mean}} \quad (see\ \text{Fig. 2}),$$

where $f_{b\,max}$ = maximum value of f_b

$f_{b\,mean}$ = mean value of f_b over the range 0 to t_a.

In practice the f_b curve is flat and the value of $f_{b\,\text{mean}}$ differs very little from $f_{b\,\text{max}}$. The variation in the surface peripheral stress along the line OO' may be obtained by multiplying all the f_b ordinates by the ratio $f_{\text{max}}/f_{b\,\text{max}}$.

2.3. Uniform Stress Measurement

No attempt was made to measure the load applied to the model, the stress in the undrilled model being obtained from measurements made in the uniform stress region between the disturbances caused by the diametral hole and the loading pins. This had two advantages: it provided a check that uniform conditions existed on either side of the change in shape, indicating that end conditions were not affecting the stress distribution around the concentration, and it also dispensed with the necessity for finding the fringe value for each model.

3. Torsion Tests

3.1. Stress Pattern in Torsion

On viewing the cylindrical tube along the axis of the diametral hole, the observed stress pattern in the vicinity of the hole is seen to be similar to that around a hole in an infinite plate, subject to uniform shear in the plane of the plate. The characteristic pattern gives rise to four alternate tensile and compressive peaks, equi-spaced around the hole boundary.

3.2. Slicing and Measurement of the Peak Stress

The model was "halved" by the cut shown in Fig. 4. Four slices (Fig. 5) were necessary to obtain the peak stress in the hole bore. The slices B_1 and B_2 were cut from the tensile and compressive peaks respectively. In general the curves of relative retardation measured through these slices coincided (Fig. 7).

The position of the peak was used to locate Slices A_1 and A_2, which were obtained by boring and turning opposite halves of the cylindrical tube. When the

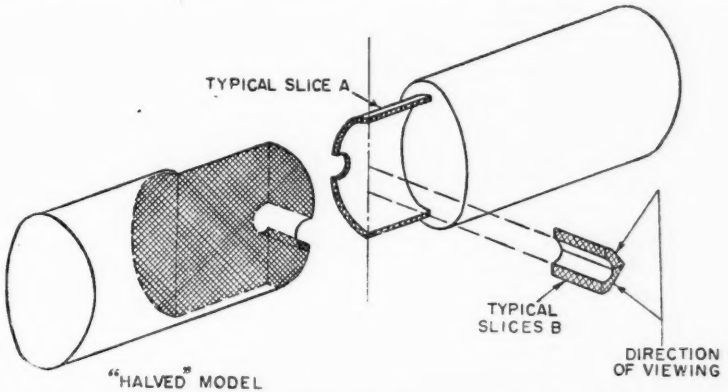

FIGURE 4. "Halving" of model and exploded view of torsion test slices.

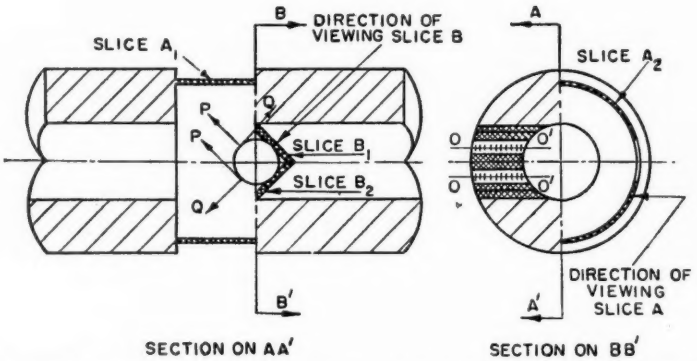

FIGURE 5. Slices to obtain the peak stress in the hole bore. Torsion test models.

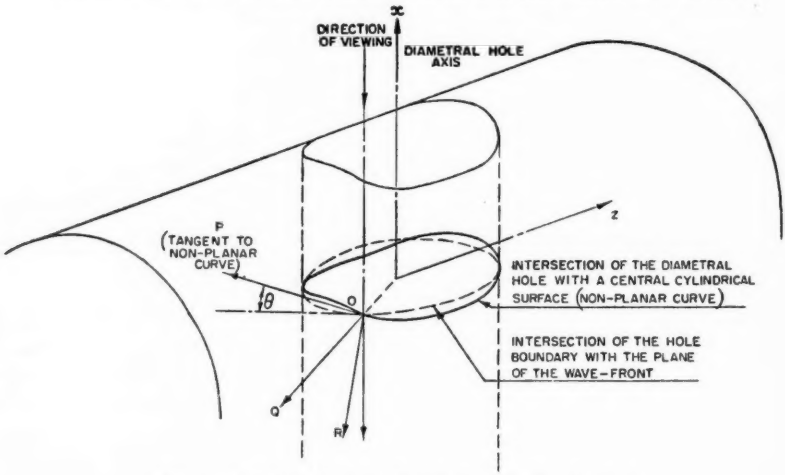

FIGURE 6. Principal stress directions at O. Torsion test.

slice is viewed in direction x, a consequence of the method of slicing is that P and Q, the principal stresses, do not lie in the plane of the wave front, the P stress being inclined at angle θ to this plane at the point of concentration (Fig. 6). Thus the extrapolated value of the observed boundary stress N is proportional to $P\cos^2\theta + R\sin^2\theta$. A further point arises in that the optical path length is greater than t_a, the measured thickness of the slice. It can be shown that N/t_a is equal to P/f (the correct peripheral stress in fringes per inch) with a maximum error of one per cent over the test range. The relative retardation was measured at points on lines OC passing through both tensile and compressive peaks in Slices A_1 and A_2. Sample curves of the mean results obtained from the two tensile and two compressive peaks are given in Fig. 8. It will be seen that the effect of compressive time-edge stresses is to depress the peripheral tensile stress and increase the peripheral compressive stress. Taking the mean of the two extrapolated results eliminates this error and gives the true value of N.

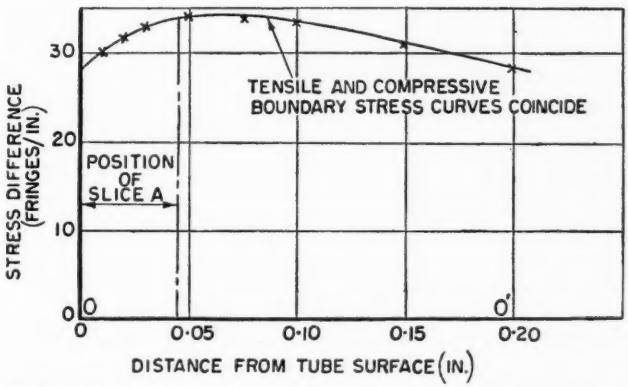

FIGURE 7. Relative retardation measured through Slices B_1 and B_2 at points along OO'.

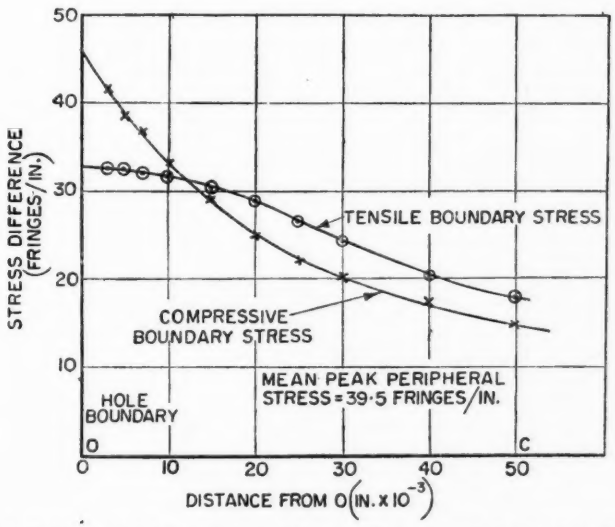

FIGURE 8. Relative retardation measured through Slices A_1 and A_2 at points along OC.

FIGURES 7 and 8. Typical torsion test results. Model details: outside diameter 1·5 in., inside diameter 0, diametral hole diameter 0·45 in., $D_1/D_0 = 0$, $d/D_0 = 0{\cdot}3$.

3.3. RESULTS

The stress concentration factor K, defined as in the Notation, is plotted for constant wall thickness in Fig. 9 and for constant hole size in Fig. 10.

In both cases smooth curves were drawn, within the estimated experimental error, so that, for a given geometry, Figs. 9 and 10 give the same S.C.F.

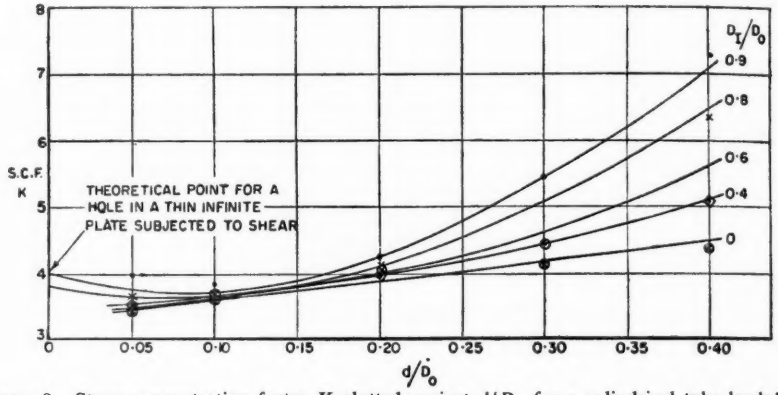

FIGURE 9. Stress concentration factor K plotted against d/D_0 for a cylindrical tube loaded in torsion.

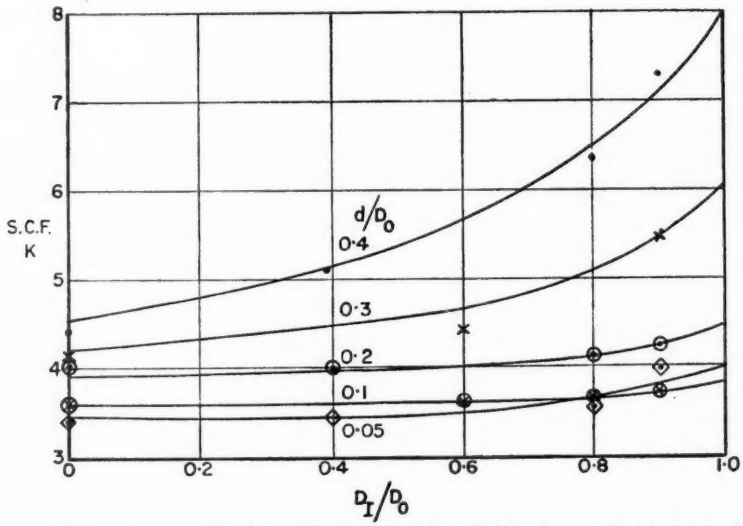

FIGURE 10. Stress concentration factor K plotted against D_1/D_0 for a cylindrical tube loaded in torsion.

3.4. DISCUSSION OF RESULTS

The design of a tubular member often involves changes of shape and size which alter the net, but not the gross, area. The S.C.F. based on the latter includes the effects both of removal of material and of geometric shape and is generally easier to apply. For torsion of tubes with transverse holes, basing the S.C.F. on the nominal stress on the net cross section implies the assumption of cross radial shear stresses proportional to distance from the tube axis. This is incompatible with the boundary conditions. For these reasons the stress concentration factors

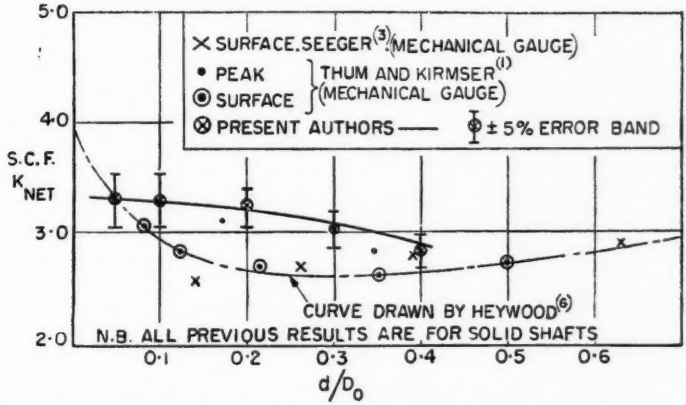

FIGURE 11. Stress concentration factor K_{net} plotted against d/D_0 for a shaft with a diametral hole in torsion.

presented in this investigation refer to a nominal stress based on the gross cross section, although all previous work refers to a net concentration factor. Comparisons are made after the appropriate recalculation.

For tubes with diametral holes there are no previous results. Comparison with previous investigations for a solid shaft is made in Fig. 11, the S.C.F., K_{net}, being based on an assumed linear shear stress distribution on the minimum section.

The indications for a solid shaft are as follows:—

(*i*) That existing estimates of the S.C.F. are low. The two experiments which do measure the peak stress are within the lower limit of the error band in the present investigation. The curves previously drawn place too much importance on the surface measurements.

(*ii*) That there are no grounds for Heywood's extrapolation from Thum and Kirmser's results to a value of 4 as $d/D_0 \longrightarrow 0$. The limiting value of 4 is only justified for very thin walled tubes (*see* Fig. 9).

4. Tension and Compression Tests

4.1. Range of Tests

The stress pattern around a diametral hole in a cylindrical tube, loaded in torsion, gives rise to tensile and compressive peak stresses of equal magnitude. Thus the effect of time-edge stress, which is always compressive in Araldite, may be eliminated by taking the mean of the results obtained from one model. To eliminate this edge-stress effect in the axial load tests it was necessary to test two similar models, one under tension and one under compression. All the models were given the same heat treatment and, as far as possible, a pair was selected from the same casting batch to ensure similarity. The two models were machined together and frozen in the straining frame.

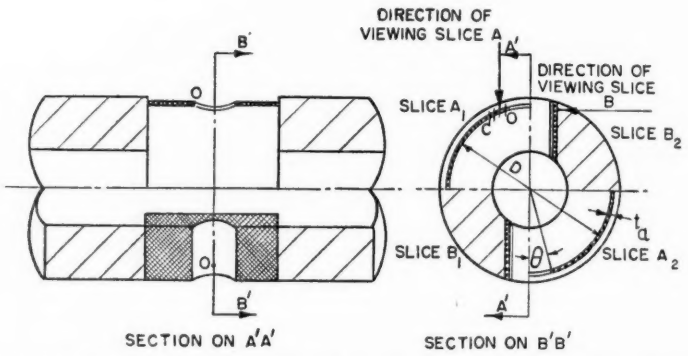

FIGURE 12. Slices to obtain the peak stress in the hole bore. Tension or compression models.

4.2. Stress Pattern Under Axial Load

The pattern observed on viewing Slice A in the direction of the diametral hole axis is similar to that obtained for a hole in an infinite plate subjected to unidirectional stress. The peak stress occurs on the boundary of the diametral hole at a point which has the direction of the applied stress as its tangent. As in the torsion case, the peak stress did not occur on the outside surface of the tube.

4.3. Slicing and Peak Stress Measurement

Both models were "halved" as in the torsion tests. Preliminary tests indicated that Slice B_2 was unnecessary and three slices were cut from each of the models (Fig. 12). The curves of relative retardation measured through the B slices are much flatter than those obtained from the B slices in the torsion tests. In many of the tension-compression tests, correct positioning of Slice A gave a ratio $f_{b\,\max}/f_{b\,\text{mean}}$ so close to 1 that the improvement was not significant, and f_a, the extrapolated value obtained from Slice A, could be taken as the peak peripheral stress in the hole bore. Slices A_1 and A_2 were obtained by turning and boring, and the relative retardation through the slices was measured at a number of points along the line OC. It was necessary to take the mean of these observations to eliminate the effects of any bending induced by the loading system. The peripheral stress at the boundary lies in the plane of the wave front (viewing Slice A in the direction of the diametral hole axis) but the optical path is equal to $t_a \sec\theta$ (where t_a is the measured thickness of the slice (Fig. 12)). Thus N_1, the mean extrapolated value of relative retardation, must be divided by $t_a/[1-(d/D)^2]$ to obtain $f_{\max}$, for each of the models.

4.4. Results

Eliminating edge-stress effects by taking the mean of the tension and compression test results, the stress concentration factor, as defined in the Notation, becomes

$$K = \frac{\text{peak stress in tension test} + \text{peak stress in compression test}}{\text{nominal stress in tension test} + \text{nominal stress in compression test}}.$$

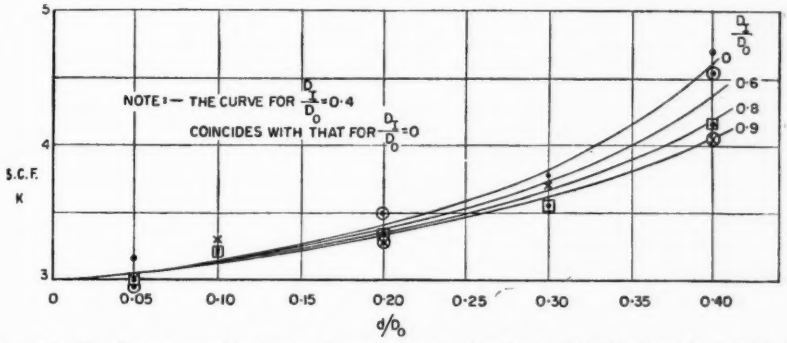

FIGURE 13. Tension-compression tests. Stress concentration factor K plotted against d/D_0 for varying D_1/D_0 ratios.

Graphs of S.C.F. are plotted for constant wall thickness ratios in Fig. 13 and for constant hole size in Fig. 14.

For a small hole ($d/D_0 < 0{\cdot}2$) the S.C.F. is independent of wall thickness. For a larger hole the S.C.F. increases with increasing wall thickness. The S.C.F. increases with increasing hole diameter, the increase being greatest in thick-walled tubes.

4.5. Discussion of Results

The experimental results indicate that all the S.C.F. curves (Fig. 15) extrapolate to a value of 3 as d/D_0 decreases to 0. The theoretical solution for a hole in an infinite plate subjected to unidirectional stress gives a factor of 3. This applies to a hole in a thin plate (generalised plane stress) or to a hole in an infinitely thick plate (plane strain) and it seems reasonable to suppose that the values of S.C.F. for a square bar and for a cylinder under axial load will tend to the same limit as the hole size is decreased to 0.

For the thin-walled tube, the increase in K as the hole size is increased would appear to be due mainly to the removal of material, since the S.C.F. based on the net area is constant to within 4 per cent for d/D_0 ratios in the range 0 to 4. For a solid shaft, a redistribution of stress also occurs and the S.C.F. based on the net area decreases by up to 25 per cent as the hole size is increased from 0 to 0·4 of the outside diameter of the shaft.

Some results for a solid shaft with a diametral hole have been obtained by Thum and Kirmser[1], using a small gauge length extensometer on a steel shaft, and by Frocht[2], using the photoelastic method. By making measurements both on the shaft surface and in the hole bore, Thum and Kirmser discovered that the true peak stress lay in the hole bore below the tube surface. Their results are significantly higher than those obtained in this investigation. Frocht mentions that difficulties in technique were encountered which led him to believe that his results were low.

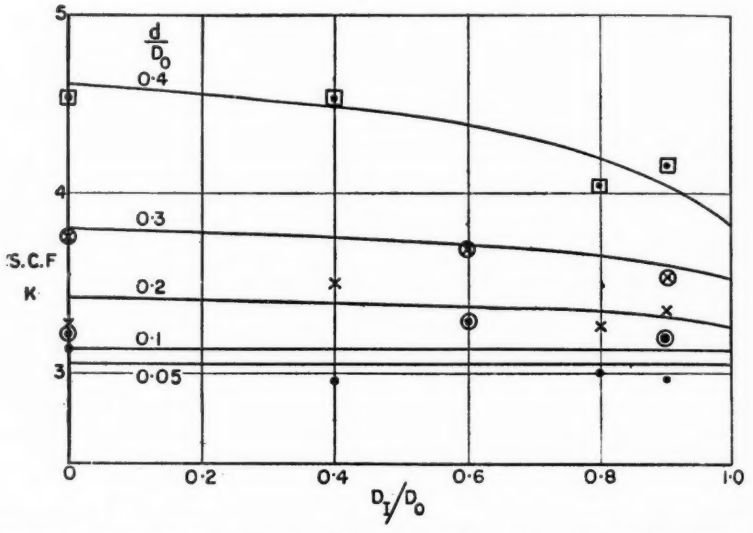

FIGURE 14. Tension-compression tests. Stress concentration factor K plotted against D_1/D_0 for varying d/D_0 ratios.

In fact he has extrapolated the measurements of peak stress in the hole bore incorrectly to satisfy his assumption that the true peak stress occurs on the surface of the shaft, and this leads to the calculation of S.C.F.'s which are too high. Thum and Kirmser have also made some measurements on square bars with diametral holes. Heywood compared all these results and plotted two curves, one for round and the other for square bars (Fig. 15). The two curves have completely different gradients as the hole size decreases to 0, but it seems unlikely that a small diameter hole is going to affect a square bar and a cylindrical tube differently. All the results of the present investigation lie below previous work. Although the difference in the results is less than twice the estimated error for an individual result, it is considered to be significant for three reasons:—

(*i*) The experimental curve for shafts is drawn against a background of information for tubes, and is estimated to have an accuracy of the order of ± 3 per cent.

(*ii*) The results of the present investigation are consistently low when compared with previous work, although no systematic error has been noted in the experimental method.

(*iii*) The difference in the previous and the present investigations cannot be attributed to the "scatter" of the present results, which is considerably less than ± 5 per cent.

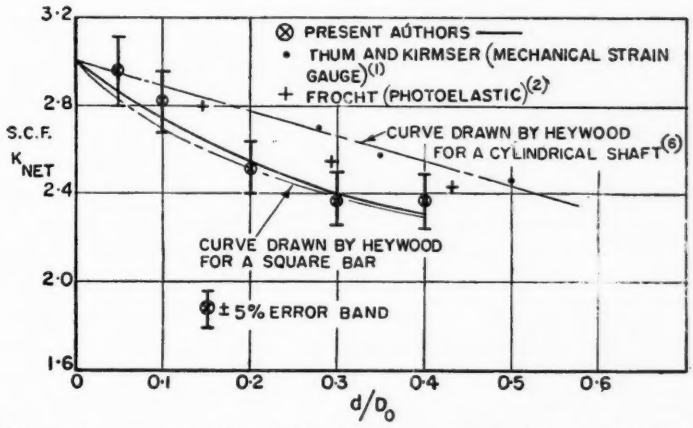

FIGURE 15. Stress concentration factor K_{net} plotted against d/D_0 for a shaft with a diametral hole in tension.

5. Bending Tests on Cylindrical Tubes with Diametral Holes

5.1. Range of Tests

The photoelastic models for the bending tests covered the same range as those for the torsion tests. The axis of the bending required to give the maximum stress concentration factor was not known and it was decided to calculate the result from the measurement of K_a and K_b, the stress concentration factors for bending about two axes which are respectively perpendicular and parallel to the diametral hole axis

5.2. Stress Pattern Under Uniform Bending

For bending in a plane parallel to the axis of the diametral hole, the pattern obtained (on viewing Slice A in the direction of the diametral hole axis) is similar to that obtained in the vicinity of a hole in an infinite plate subjected to unidirectional stress. As in the torsion tests, the peak stress does not occur on the surface of the tube and the mean peak value, measured through a slice of appreciable thickness, is improved by using a knowledge of the variation in stress through the slice. For bending in a plane perpendicular to the axis of the diametral hole, the peak stress concentration was found to occur in sensibly the same position as in the case of bending parallel to the diametral hole axis. The stress concentration factor is much lower in this case, however, and falls markedly as the hole size is decreased, the effect on the value of K being insignificant for the smaller hole sizes in the test range.

5.3. Slicing and Peak Stress Measurement

The method of slicing and examination was similar to that carried out with the tension test models, with one exception. Since the model was curved after freezing,

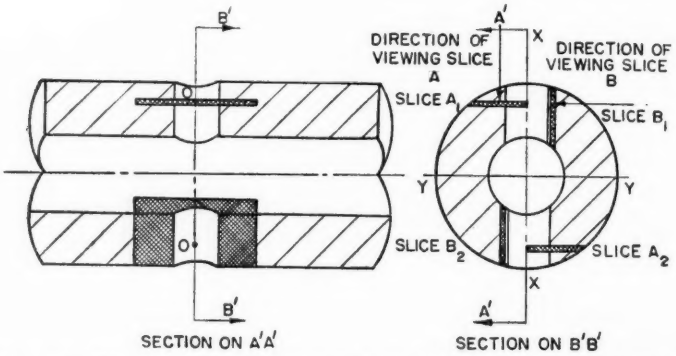

FIGURE 16. Slices to obtain the peak stress in the hole bore. Bending test models.

it was no longer possible to turn and bore the halved tube to obtain Slices A_1 and A_2. The model was set upon a Vee block and the four slices (Fig. 16) were marked out, using a height gauge, before cutting them out by hand. A finish suitable for viewing was obtained, as with all the B_1 and B_2 slices, by using fine emery paper. The mean of the two diametrically opposite A_1 and A_2 slices was taken to eliminate the effects of time-edge stress and non-uniformity in the loading and the mean stress f_a through a 0·04 in. thick slice was obtained. As before, the maximum value of peripheral stress in the bore of the diametral hole is given by

$$f_{\max} = f_a \times \frac{f_{b\,\max}}{f_{b\,\text{mean}}}.$$

In most cases the f_b curve was found to be flat near the peak and, in many of the experiments for bending parallel to the diametral hole axis and in all the experiments for bending perpendicular to the diametral hole axis, the correction $f_{b\,\max}/f_{b\,\text{mean}}$ was found to be insignificant, provided that the A slices were cut so as to embrace the peak in the f_b curve.

TABLE II

VALUES OF K_a AND K_b

	$d/D_O=0{\cdot}05$		0·1		0·2		0·3		0·4	
	K_a	K_b	K_a	K_b	K_a	K_b	K_a	K_b	K_a	K_b
$D_I/D_O=0$	3·00		2·66		2·94		3·44	0·72	3·95	1·35
0·4	2·92				3·03				4·00	1·30
0·6			2·93				3·26	0·72		
0·8	2·82				3·15				4·08	0·79
0·9	3·02		2·82		3·21		3·52	0·71	4·4	0·84

5.4. RESULTS

The values of K_a and K_b are given in Table II. It will be seen that the factors K_b were not obtained experimentally for models having a d/D_O ratio less than 0·3, the results for smaller diametral hole sizes being insignificant compared with the value of K. As in the torsion and tension tests, K is defined as in the Notation.

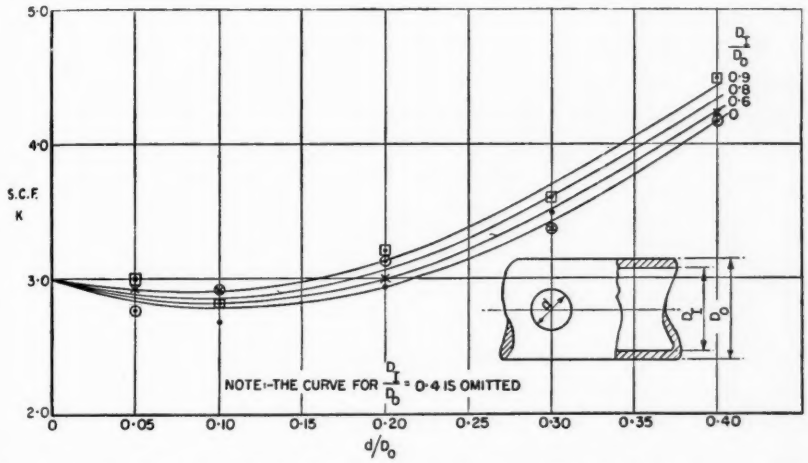

FIGURE 17. **Bending test.** Stress concentration factor K plotted against d/D_0 for varying D_1/D_0 ratios.

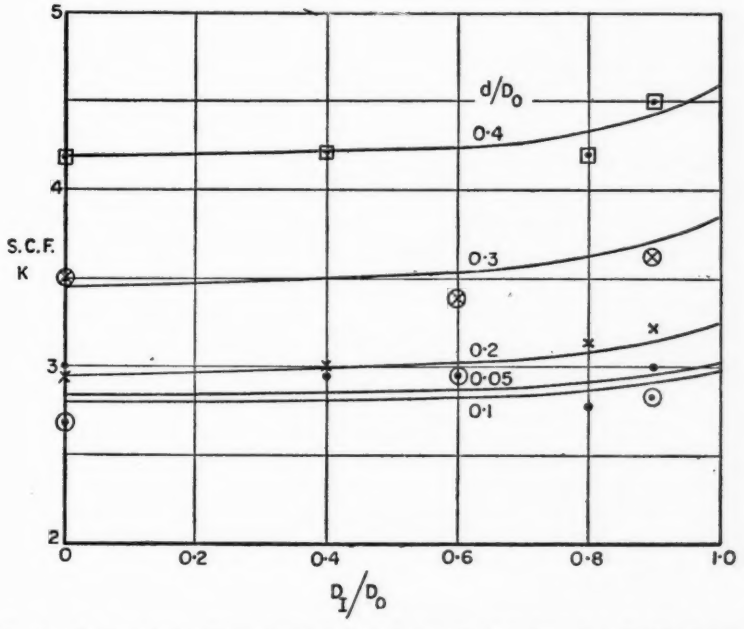

FIGURE 18. **Bending test.** Stress concentration factor K plotted against D_1/D_0 for varying d/D_0 ratios.

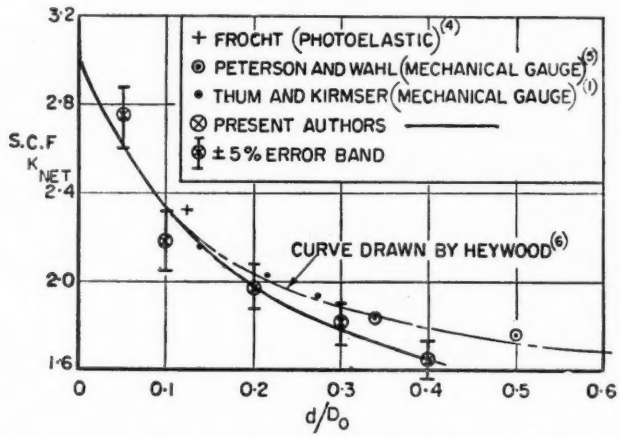

FIGURE 19. Stress concentration factor K_{net} plotted against d/D_O for a shaft with a diametral hole in bending.

In this context

K = maximum stress concentration factor

K_a = stress concentration factor for bending in a plane parallel to the diametral hole axis

K_b = stress concentration factor for bending in a plane perpendicular to the diametral hole axis.

It may be shown that

$K = \sqrt{(K_a^2 + K_b^2)}$ = maximum possible stress concentration factor for bending.

Graphs of the stress concentration factor K are plotted for constant wall thickness in Fig. 17 and for constant hole size in Fig. 18.

5.5. Discussion of Results and Conclusions

The curves all extrapolate to a S.C.F. of 3 as the d/D_O ratio decreases to 0, and are similar in shape to those obtained for the torsion tests. The S.C.F. for a thin tube lies above that for a thicker walled one, and initially there is a decrease in K as the diametral hole size is increased. It appears that these effects are associated with the presence of a radial stress gradient, since they occur both in bending and torsion but not under axial load. In the axial loading case, the S.C.F. for thick wall tubes lies below that for thin wall tubes and no initial decrease in K is observed. A comparison of Figs. 17 and 18 shows that changing the size of the diametral hole has a greater effect than changing the D_I/D_O ratio. Fig. 19 shows the comparison between the results of previous tests and those of the present investigation. The agreement is better than for the tension-compression and torsion tests.

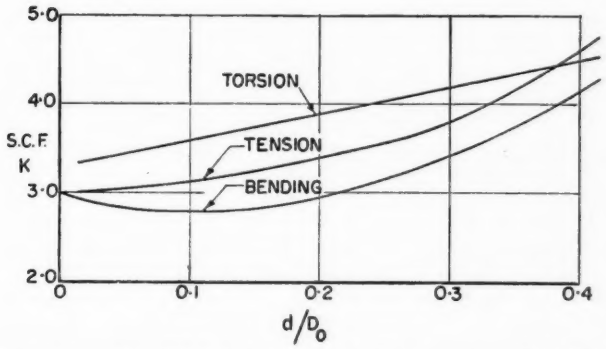

FIGURE 20. Comparison of the S.C.F. in a solid shaft with a transverse hole. Torsion, tension and bending.

6. General Conclusions

The present investigation is the most comprehensive yet undertaken, previous work being confined to the effects of diametral holes in solid shafts. In comparing the results for solid shafts with those of other investigators, it should be remembered that the curves have been drawn with due regard to a range of information about tubes of varying inside diameter. Although the estimated accuracy for an individual experimental result is of the order of ± 5 per cent, the graphs are the result of fitting curves to a large number of different points in order to satisfy the cross-plotting conditions. The results are probably more reliable than the estimated percentage error would indicate.

The photoelastic results in bending and under axial load are slightly lower, in general, than those obtained in previous tests. In making comparisons with previous results the following points should be noted. In bending, a single curve will fit all the existing experimental points to within 5 per cent, except for very large holes, which are outside the range of the present investigation. In tension, the differences between the results exceeds the experimental error of the investigation. The mechanical strain gauge results by Thum and Kirmser appear to be too high, but precise details of the experiment are not available. In torsion, the present results are significantly higher than previous results, mainly because previous investigators have failed to measure the peak stress. Thum and Kirmser have measured the stress in the diametral hole bore, below the surface of the shaft, and their results are only 4 per cent below those of the present tests. It is generally thought that the effect of a model material having a high Poisson's ratio is to lower the peak stress slightly. But the most reliable results for steel models, due to Thum and Kirmser, are higher in tension and lower in torsion than the corresponding photoelastic factors. Thus the Poisson's ratio effect is unlikely to be a major cause of the differences observed.

The stress concentration factors for the three types of loading do not follow similar trends, *e.g.* the factor for tension is not always greater than that for

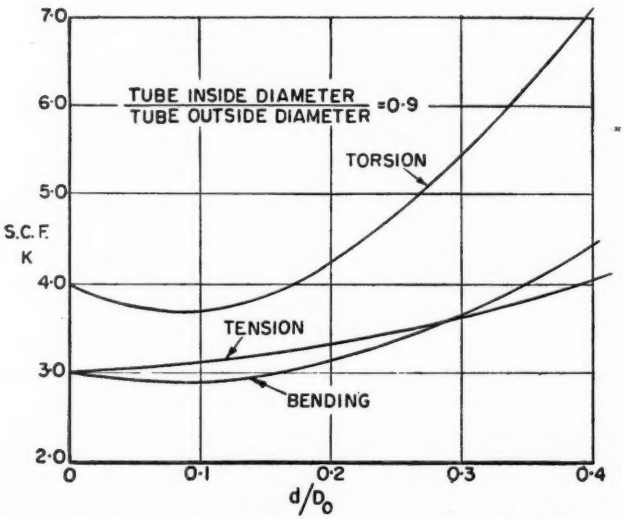

FIGURE 21. Comparison of the S.C.F. in a thin-walled tube with a transverse hole. Torsion, tension and bending.

bending, as would appear from the solid shaft results (Fig. 20). The torsion factor is nearly always the highest, the differences between this and the other factors being greatest for thin-walled tubes (Fig. 21). The trends which are observed in any particular case would not have been deduced from the knowledge of other cases and the large number of photoelastic tests completed could not have been reduced with safety.

REFERENCES

1. THUM, A. and KIRMSER, W. Tension, Bending and Torsion of Shafts with Transverse Holes. *V.D.I. Forschungsheft*, 419. March-April 1943.

2. FROCHT, M. M. Stress Concentrations in Shafts with Transverse Circular Holes in Tension. *Journal of Applied Physics*, January 1944.

3. SEEGER, G. Stresses in Transversely Loaded Shafts subjected to Torsion. *Die Technik*, 3. July 1948; *Engineers' Digest*, February 1949.

4. FROCHT, M. M. Stresses in Bent Circular Shafts with Transverse Holes. *Journal of Applied Mechanics*, March 1944.

5. PETERSON, R. E. and WAHL, A. M. Two- and Three-dimensional Cases of Stress Concentration and Comparison with Fatigue Strength. *Transactions of the American Society of Mechanical Engineers; Journal of Applied Mechanics*, Vol. 58, 1936

6. HEYWOOD, R. B. *Designing by Photoelasticity*. Chapman and Hall, London, 1952.

Theoretical and Experimental Studies of Stall Propagation in Rows of Axial Flow Compressor Blades

M. D. WOOD, M.A., Ph.D., A.M.I.Mech.E.

(University Engineering Laboratory, Cambridge)

SUMMARY: The paper concerns a phenomenon which occurs in rows of closely spaced blades, as in an axial flow compressor, when the flow around the blades approaches the stalling condition. Patches of stalled flow can propagate along the blade row, thus causing cyclic variations in the lift on individual blades. Under certain conditions this cyclic loading can lead to large blade stresses, and ultimately to blade failure.

The theory developed in the paper uses small perturbation concepts to predict the velocity of propagation of these stalled zones, or " stall cells," along the cascade. The results of the theory are applied to experimental data obtained by the author from 9- and 66-bladed cascades of aerofoils. The theoretical results are then compared directly with the velocities of propagation measured on the cascades.

The conclusions of the paper draw attention to the shortcomings of the small perturbation concept, used in the theoretical work, and show that a different form of approach will be necessary to forecast the behaviour of the stall cells accurately.

1. Introduction

Stall propagation has been investigated by a number of research workers, both experimentally and analytically. Smith and Fletcher[1] observed a rotating stall on low speed fans by means of a wool-tuft technique. Emmons and his co-workers[2] used hot wire anemometer equipment to investigate stall cell propagation in an axial flow compressor and in the inducer of a centrifugal compressor. These authors proposed a description of the mechanism of stall propagation which is accepted as being qualitatively correct. They also developed a stability analysis to predict, from cascade data, the aerodynamic incidence at which stall propagation might be expected in a blade row. Iura and Rannie[3] have given details of another experimental investigation into stall propagation in an axial flow compressor.

Received December 1958.

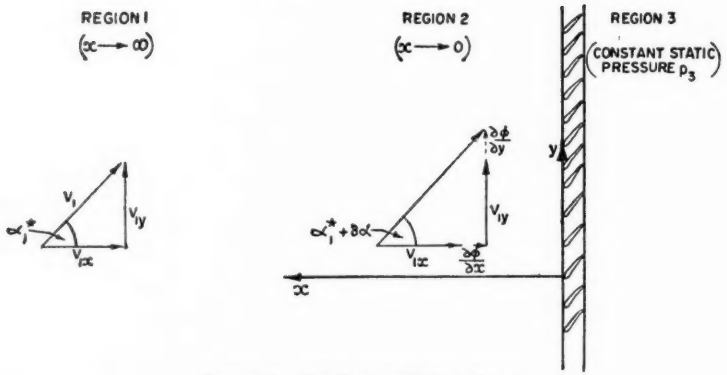

FIGURE 1. Small perturbation theory.

Sears[4], Marble[5] and Stenning[6] have each produced theories of stall propagation, based on the concept of treating the disturbances associated with each stall cell as small perturbations of the main flow. The present author makes use of the same concept and shows that it is possible to predict the velocity of propagation of an individual cell.

The results of the analysis are used to predict velocities of propagation in cascades of aerofoils and on a single-stage axial compressor. These theoretical results are then compared with experimental results, and the discrepancies used to deduce the probable inadequacies of the theory.

NOTATION

x, y	co-ordinates in a two-dimensional system (*see* Fig. 1)
t	time
V_1	inlet velocity
V_{1x}, V_{1y}	components of V_1 in x- and y-directions
α_1	air inlet angle measured relative to normal to cascade
$\alpha_1\star = \tan^{-1}(V_{1y}/V_{1x})$	
$\delta\alpha$	increase of $\alpha_1\star$ at $x=0$ due to $\partial\phi/\partial x$ and $\partial\phi/\partial y$
ϕ	disturbance velocity potential upstream of cascade
$\partial\phi/\partial x, \partial\phi/\partial y$	perturbation components of velocity caused by stall pattern
p	static pressure
ρ	air density (assumed constant)
$q_1 = \frac{1}{2}\rho V_1^2$	
γ	slope of curve of $\dfrac{(p_3 - p_1\star)}{q_1}$ $f(\tan\alpha_1)$
$\gamma\star = \gamma$ at $\alpha_1 = \alpha_1\star$	

$\gamma' = \gamma$ at $\alpha_1 = \alpha_1'$

l length between corresponding points on adjacent stall cells

λ velocity of propagation of stall cells

n number of the harmonic of ϕ under consideration

$p_1\star$ static pressure far upstream of the cascade corresponding to inlet angle $\alpha_1\star$

p_2 static pressure at cascade inlet (equal to $p_1\star$ under steady flow conditions)

p_3 static pressure downstream of cascade (assumed constant)

X distance along cascade (*see* Fig. 7)

A, B constants defined by equations (7) and (8)

b_n coefficient of n^{th} harmonic of assumed solution for ϕ

Suffixes

n refers to n^{th} harmonic

1 refers to flow region far upstream of the cascade

2 refers to flow region immediately in front of the cascade

3 refers to flow region downstream of the cascade.

2. Basic Theory

A small unsteady perturbation flow is assumed to be superimposed on the steady flow through an infinite two-dimensional cascade, as shown in Fig. 1. Since the flow upstream of the cascade is irrotational, the perturbation velocities in that region may be represented by means of a perturbation velocity potential ϕ. The cascade is assumed to lie on the y-axis, so that $\partial\phi/\partial y$ represents the perturbation velocity in the direction parallel to the cascade and $\partial\phi/\partial x$ represents the perturbation velocity in the x- or axial direction. Far upstream the perturbation velocities are all zero, only the basic flow remaining.

Since there are no losses in the flow field upstream of the cascade, the Bernouilli equation of flow may be applied between upstream infinity and inlet to the cascade.

This gives

$$\frac{p_1\star}{\rho} + \frac{V_1^2}{2} = \frac{p_2}{\rho} + \left(\frac{(V_{1x} + \partial\phi/\partial x)^2}{2}\right) + \left(\frac{(V_{1y} + \partial\phi/\partial y)^2}{2}\right) + \frac{\partial\phi}{\partial t} \quad . \quad (1)$$

Neglecting squares of small quantities, equation (1) reduces to

$$\frac{\partial\phi}{\partial t} + V_{1x}\frac{\partial\phi}{\partial x} + V_{1y}\frac{\partial\phi}{\partial y} + \frac{p_2 - p_1\star}{\rho} = 0. \quad . \quad . \quad . \quad . \quad (2)$$

$(p_2 - p_1\star)/\rho$ must now be expressed as a function of ϕ.

It is assumed that the static pressure rise characteristic of the cascade is available from tests carried out under steady flow conditions and that the characteristic has been plotted in the form $\triangle p/q_1 = \text{function } (\tan \alpha_1)$.

For small changes of inlet angle from the mean value $\alpha_1\star$ it may be assumed that the static pressure rise characteristic is linear, with a slope $\gamma\star$. The static pressure at inlet to the cascade can then be determined on a quasi-steady flow basis in terms of the mean flow characteristics and the perturbation velocity components. It is also assumed that the downstream static pressure (p_3) remains constant.

Thus, under steady flow conditions, the static pressure rise across the cascade would be given by

$$(p_3 - p_1\star) = q_1 \left[\frac{(p_3 - p_1\star)}{q_1}\right] .$$

With the perturbation velocity components at inlet to the cascade this becomes

$$(p_3 - p_2) = [q_1 + \delta q_1]\left[\frac{(p_3 - p_1\star)}{q_1} + \gamma\star\, \delta \tan \alpha_1\star\right] .$$

Neglecting products of small quantities, this reduces to

$$(p_1\star - p_2) = q_1\gamma\star\ (\delta \tan \alpha_1\star) + \frac{(p_3 - p_1\star)}{q_1}\ \delta q_1 . \quad . \quad . \quad . \quad (3)$$

The increase in $\tan \alpha_1$ caused by $\partial\phi/\partial x$ and $\partial\phi/\partial y$ is shown in Fig. 1.

Thus,
$$\tan (\alpha_1\star + \delta\alpha_1) = \frac{V_{1y} + \partial\phi/\partial y}{V_{1x} + \partial\phi/\partial x}$$
$$= \left[\tan \alpha_1\star + \frac{\partial\phi/\partial y}{V_{1x}}\right]\left[1 + \frac{\partial\phi/\partial x}{V_{1x}}\right]^{-1} \quad . \quad . \quad (4)$$

This may be expanded to give, approximately,

$$\delta \tan \alpha_1\star = \tan (\alpha_1\star + \delta\alpha_1) - \tan \alpha_1\star$$
$$= \frac{\partial\phi/\partial y}{V_{1x}} - (\tan \alpha_1\star)\ \frac{\partial\phi/\partial x}{V_{1x}} \quad . \quad . \quad . \quad . \quad (5)$$

Similarly $(q_1 + \delta q_1) = \frac{1}{2}\rho \left[\left(V_{1x} + \dfrac{\partial\phi}{\partial x}\right)^2 + \left(V_{1y} + \dfrac{\partial\phi}{\partial x}\right)^2\right]$

$$= \tfrac{1}{2}\rho \left[V_{1x}^2 + V_{1y}^2 + 2\left(V_{1x}\frac{\partial\phi}{\partial x} + V_{1y}\frac{\partial\phi}{\partial y}\right)\right]$$

Therefore $\delta q_1 = \rho \left[V_{1x}\dfrac{\partial\phi}{\partial x} + V_{1y}\dfrac{\partial\phi}{\partial y}\right] . \quad . \quad . \quad . \quad . \quad . \quad . \quad (6)$

Equations (5) and (6) may now be substituted in equation (3) and the resultant expression for $p_2 - p_1\star$ substituted in equation (2).

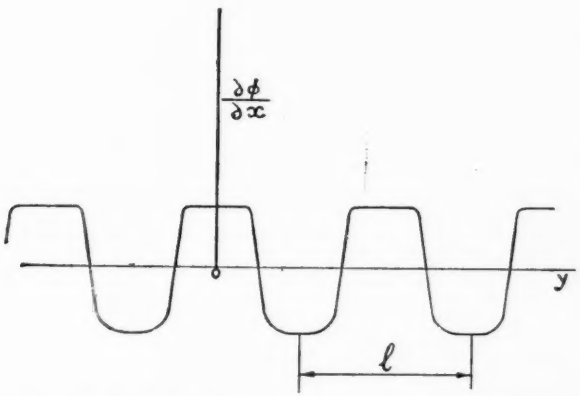

FIGURE 2. Perturbation of axial flow. Assumed wave form at cascade inlet.

After some manipulation this results in the equation

$$\frac{\partial \phi}{\partial t} + \frac{\partial \phi}{\partial x}\left\{V_{1x}\left[1 - \frac{(p_3 - p_1\star)}{q_1}\right] + \frac{q_1\gamma\star}{\rho V_{1x}}\tan\alpha_1\star\right\} + \\ + \frac{\partial \phi}{\partial y}\left\{V_{1y}\left[1 - \frac{(p_3 - p_1\star)}{q_1}\right] - \frac{q_1\gamma\star}{\rho V_{1x}}\right\} = 0. \quad . \quad (7)$$

which is rewritten, for convenience,

$$\frac{\partial \phi}{\partial t} + A\frac{\partial \phi}{\partial x} + B\frac{\partial \phi}{\partial y} = 0. \quad . \quad . \quad . \quad . \quad (8)$$

It is now necessary to postulate a solution for ϕ which satisfies equation (8). Observation of stall propagation in compressors, by the hot wire technique, indicated that the disturbances propagated at a steady velocity (λ) at fixed distances apart (l), each "cell" retaining a shape which was identical with those of its neighbours. Also, it was known that far upstream of the blade row the disturbances disappeared. The author considered that it would be a reasonable approximation to represent the axial velocity perturbations at the cascade inlet as a series of symmetrical wakes of undefined width and spacing. The axial velocity perturbation would then appear as in Fig. 2 and might be represented by the series

$$\phi = \sum_{n=1}^{n=\infty} e^{-2n\pi x/l}\left[b_n \cos\frac{2n\pi}{l}(y - \lambda t)\right] \quad . \quad . \quad . \quad . \quad (9)$$

This solution satisfies:—

(*i*) Continuity ($\nabla^2\phi = 0$ for all values of t).

(*ii*) The condition that the disturbance should disappear at large values of x (far upstream of the cascade).

(*iii*) The wave form conditions imposed in Fig. 2.

(*iv*) The condition that the disturbance propagates at a velocity λ along the cascade, each cell retaining its initial shape.

It should be noted that the choice of solution (9) implies that there is no alteration in the total mass flow through the blade row ($\int_0^l (\partial\phi/\partial x)\,dy = 0$ for each term of the series).

Substituting relation (9) into equation (8) gives

$$\Sigma\, e^{-2n\pi x/l}\left[b_n \frac{2n\pi}{l}\lambda \sin\frac{2n\pi}{l}(y-\lambda t)\right] + A\,\Sigma\left(-\frac{2n\pi}{l}\right) e^{-2n\pi x/l}\left[b_n \cos\frac{2n\pi}{l}(y-\lambda t)\right] +$$

$$+ B\,\Sigma\, e^{-2n\pi x/l}\left[-b_n\left(\frac{2n\pi}{l}\right)\sin\frac{2n\pi}{l}(y-\lambda t)\right] = 0. \quad . \quad (10)$$

Equation (10) is solved by equating coefficients of the sines and cosines of the n^{th} harmonic of ϕ as follows:—

Coefficients of $\sin\frac{2n\pi}{l}(y-\lambda t)$: $\quad \lambda b_n - B b_n = 0.$

Therefore $\lambda = B$ (if b_n is finite). . . . . (11)

Coefficients of $\cos\frac{2n\pi}{l}(y-\lambda t)$: $\quad -A b_n = 0.$

Therefore $A = 0$ (if b_n is finite). . . . . (12)

Thus stall propagation will occur when $A = 0$, or when $\gamma\star$ has the unique value γ' where

$$\gamma' = -\frac{\rho V_{1x}^2}{q_1 \tan\alpha_1'}\left[1 - \frac{(p_3 - p_1\star)}{q_1}\right] \quad \text{at inlet angle } \alpha_1'. \quad . \quad . \quad (13)$$

In accordance with experience, the theory shows that stall propagation will occur at an inlet angle where the slope of the pressure rise characteristics is negative. At this selected value of α_1 all harmonics of the disturbance associated with the stall cells would travel along the cascade with a velocity λ, where

$$\lambda = V_{1y}\left[1 - \frac{(p_3 - p_1\star)}{q_1}\right] - \frac{\gamma' q_1}{\rho V_{1x}},$$

from (11).

Substituting for γ', from equation (13), the velocity of propagation is defined by

$$\lambda = V_{1y}\left[1 - \frac{(p_3 - p_1\star)}{q_1}\right] + \frac{V_{1x}}{\tan\alpha_1'}\left[1 - \frac{(p_3 - p_1\star)}{q_1}\right]$$

$$\text{or} \quad \frac{\lambda}{V_{1x}} = 2\,[\operatorname{cosec} 2\alpha_1']\left[1 - \frac{(p_3 - p_1\star)}{q_1}\right]. \quad . \quad . \quad . \quad . \quad . \quad (14)$$

The velocity of propagation predicted by equation (14) may now be compared with experimental values.

3. Comparison with Experiment

3.1. Initial Cascade Tests

Stall propagation was detected on a 9-bladed cascade operating at high incidence. The cascade is fully described in Ref. 7. The blading specification was as follows:—

6 in. chord, 6 in. pitch, 18 in. span, 36° stagger profile 10C4/30C50, Reynolds number approximately 10^5 at an inlet velocity of 30 ft./sec.

The observed velocity of propagation was 30 per cent of the inlet axial velocity, *i.e.* $\lambda/V_{1x}=0{\cdot}30$. However, the value predicted by the small perturbation theory was $\lambda/V_{1x}=1{\cdot}45$.

3.2. Discrepancy Between Theory and Experiment

The discrepancy could be attributed to at least three causes:—

(*i*) The quasi-steady flow approach of the theoretical analysis was inadequate.

(*ii*) The number of blades on the cascade was insufficient to simulate the "infinite" cascade of the theory.

(*iii*) The disturbances were too large to be treated as "small perturbations".

The first cause was investigated theoretically. The analysis was extended to include dynamic effects on the static pressure at inlet to the cascade. Instead of assuming that this pressure took up the steady-flow value corresponding to the perturbed inlet conditions instantaneously, it was assumed that it would approach this condition exponentially with lapse of time. The analysis is laborious and is not reproduced here. It will suffice to quote the results. The extended theory showed that the inlet static pressure variation lagged behind the inlet velocity conditions by an amount which was uniquely determined by the steady-flow cascade characteristics. The velocity of propagation, which was dependent on the "lag", was also determined, but it still differed markedly from the experimental results on the 9-bladed cascade. A value of λ/V_{1x} of 1·10 was predicted, which must be compared with the experimental value of 0·30, and the value of 1·45 predicted by the more simple theory.

3.3. Experiments on 66-Bladed Cascade

It was necessary to investigate the second cause experimentally, and for this purpose a 66-bladed two-dimensional cascade was built to simulate the conditions of the theory as closely as possible. For purposes of comparison the blading configuration was designed to be as nearly as possible identical with that of the 6 in. chord cascade on which the initial work had been done. Some compromise was necessary for practical reasons. For example, the $1\frac{1}{2}$ in. chord blading was formed by an extrusion process which necessitated a slightly increased trailing edge radius

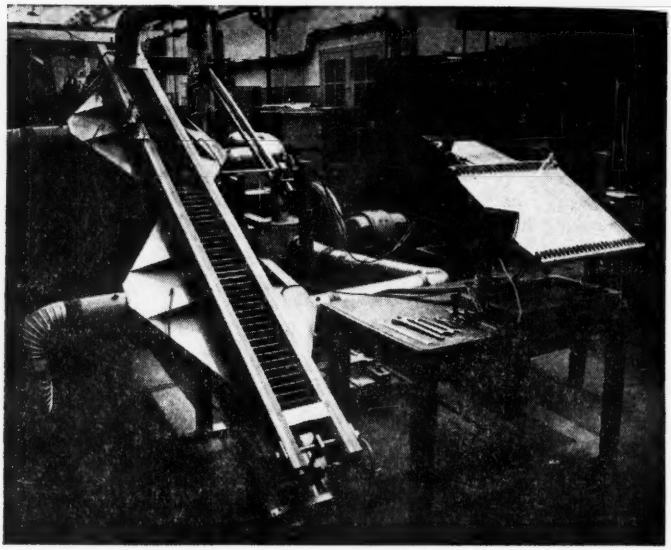

FIGURE 3. 66-bladed cascade

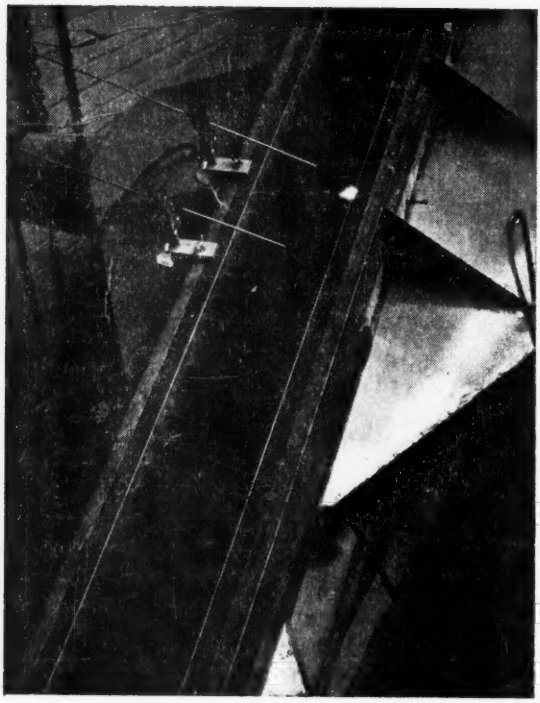

FIGURE 4. Hot wire anemometers arranged for measurement of velocity of stall propagation on 66-bladed cascade.

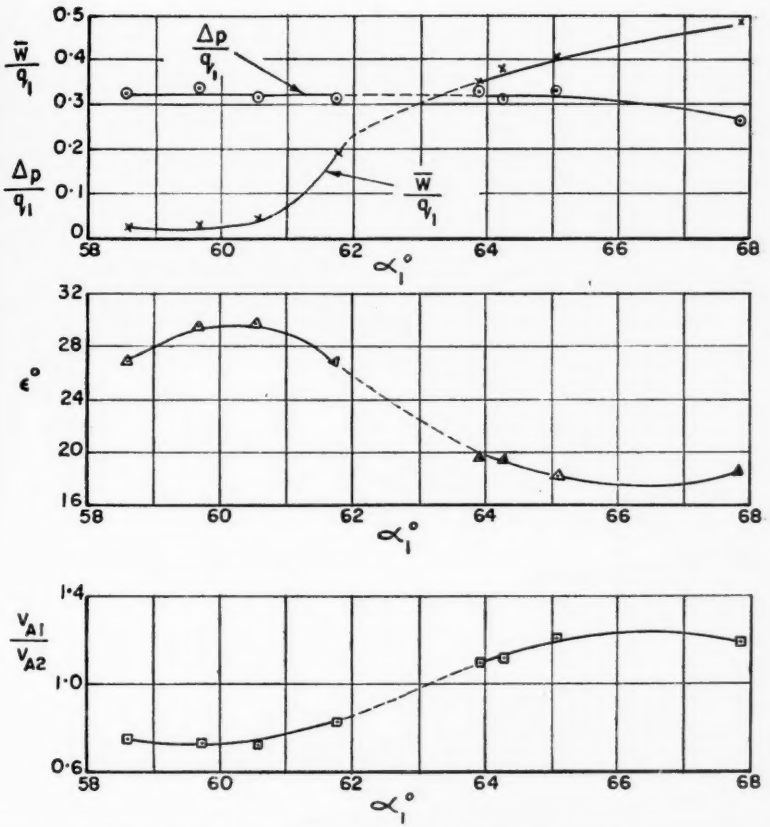

FIGURE 5. 66-bladed cascade. Aerodynamic data:—10C5/30C50, $s/c = 1$, stagger = 36°, inlet Reynolds number = $0{\cdot}90 \times 10^5$.

to the profile. The blading specification for the 66-bladed cascade was therefore as follows:—

1·5 in. chord, 1·5 in. pitch, 6 in. span, 36° stagger, profile 10C5/30C50, Reynolds number approximately 10^5 at an inlet velocity of 120 ft./sec.

A general view of the cascade is shown in Fig. 3 and a close-up view of the cascade discharge, with hot wire anemometers in position for measuring the propagation velocity, in Fig. 4.

The centre-section aerodynamic characteristics of the blading were determined over the range in which stall propagation occurred. Great care was taken to ensure that the inlet conditions to the cascade were as nearly uniform as possible. In all tests approximately one per cent of the total flow at inlet was removed by boundary layer suction applied to the tunnel roof and to the two tunnel walls upstream of the

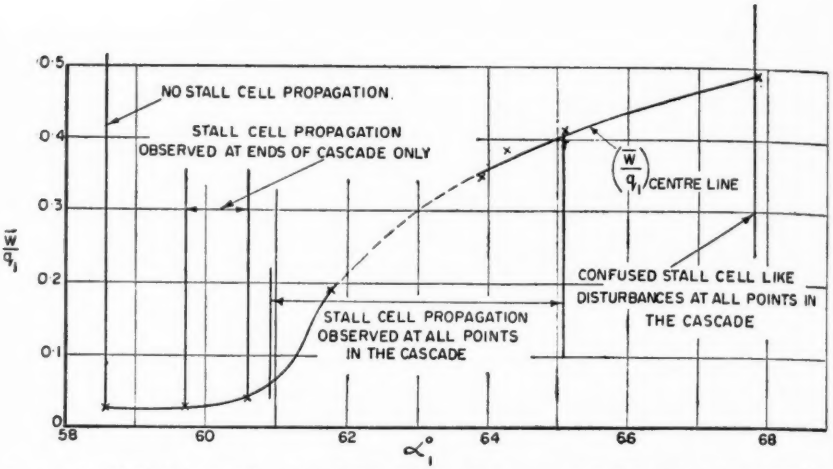

FIGURE 6. 66-bladed cascade. Correlation between loss curve and observed stall propagation.

cascade. The inlet conditions were checked by means of a Fecheimer three-hole probe. This probe was also used to determine the centre-line conditions at outlet from the cascade.

The centre-line characteristics, representing integrated mean values over several blade pitches, are presented on Fig. 5. An examination of the curve relating inlet and outlet axial velocities shows that strong three-dimensional effects were present. There was also a marked discontinuity in the flow conditions between inlet angles of 62° and 64° (shown on the curves as a broken line interpolation). In fact the cascade was set to the geometrical inlet angle corresponding to $\alpha_1 \simeq 62°$ and, by increasing the geometric inlet angle by only a quarter of a degree, the flow established itself in the condition corresponding to $\alpha_1 \simeq 64°$. This three-dimensional effect results in the rather unusual phenomenon of a static pressure rise coefficient which is virtually independent of incidence. The total pressure loss curve has therefore been used to show the correlation between the onset of stall and the onset of stall propagation (*see* Fig. 6).

No stall propagation was observed anywhere in the cascade at an air inlet angle (α_1) of 58° 37′. At $\alpha_1 = 59°\ 42'$ disturbances were noted at the ends of the cascade, but it was only when the inlet angle was raised to 60° 34′ that it was possible to obtain sufficiently clear information from the hot wire oscillograms to compute the velocities of propagation. At air inlet angles between 60° 53′ and 65° 03′ stall propagation was observed at all points on the cascade (except in blade channels which accepted flow from the tunnel roof and floor boundary layers and which showed permanent stall). At an inlet angle of 67° 50′, the hot wire oscillograms indicated confused stall cell-like disturbances at all points in the cascade, but it was not possible to determine the velocity of propagation. The tests were discontinued at this inlet angle (67° 50′).

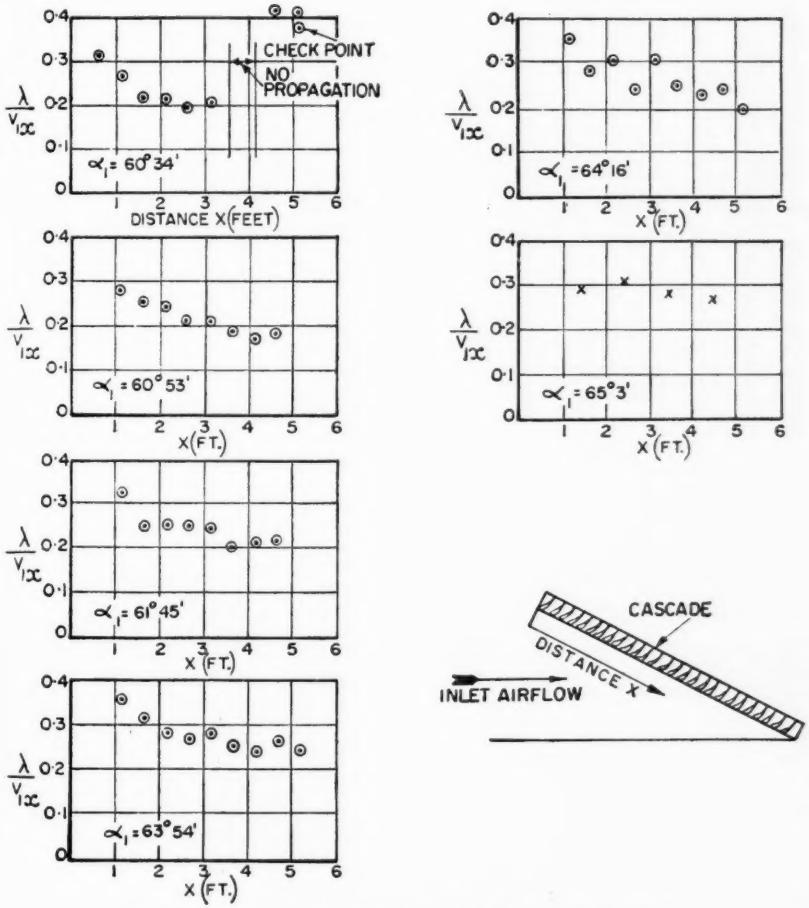

FIGURE 7. 66-bladed cascade. Local velocities of propagation.
⊙ Mean propagation velocity (probes 0·5 ft. apart).
× Mean propagation velocity (probes 1·0 ft. apart).

Figure 7 shows the recorded velocities of propagation at a series of positions on the cascade for the range of inlet angles covered in the tests. Two points are immediately apparent:—

(*i*) There is no significant difference between the order of magnitude of the velocities of propagation observed in the 66-bladed cascade from those observed in the 9-bladed cascade, in both cases approximately 30 per cent of the inlet axial velocity.

(*ii*) There is a general tendency for the stall cells to decelerate as they propagate from one end of the cascade to the other.

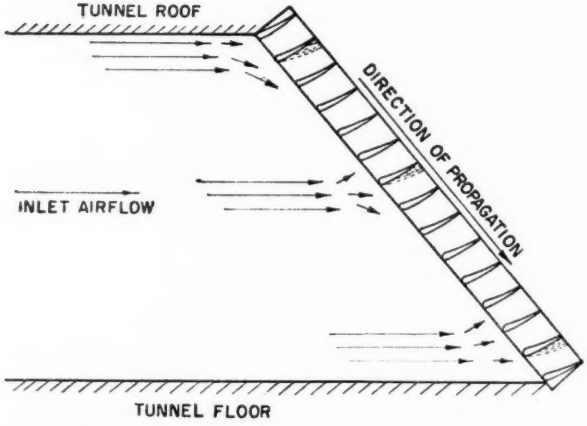

FIGURE 8. Stall propagation in cascades. Cascade end effects.

3.4. DECELERATION EFFECT

The deceleration may be explained by an extension to the conventional qualitative description of the mechanism of stall propagation. If a stall cell is established in the centre of a cascade, the flow ahead of the stall cell diverges (thus causing propagation) and to a first approximation it may be assumed that equal amounts of fluid are diverted to each side of the partially blocked channel. However, the inlet flow to a stall cell at the top of the cascade cannot deform symmetrically because of the influence of the tunnel roof, which imposes a rigid streamline on the flow pattern (Fig. 8). More spillage will thus occur ahead of the stall cell, the next blade will be affected by a greater flow perturbation and will therefore stall earlier than it would have done had the stall cell been remote from the tunnel roof. This would produce an increased velocity of propagation. The effect is reduced as the cell propagates away from the tunnel roof and accordingly the propagation velocity decreases.

The application of similar reasoning to the spillage flow around a stall cell approaching the tunnel floor shows that the disturbance ahead of the cell is reduced, the stall of the next blade is delayed and the propagation velocity falls to a value below that corresponding to the centre of the cascade. Examination of the results of Fig. 7 shows that the deceleration takes effect over most of the length of the cascade.

3.5. MAGNITUDE OF CASCADE PROPAGATION VELOCITY

The measured velocities of propagation are shown on Fig. 9 as a function of air inlet angle. The results shown are mean values over the length of the cascade in which propagation was detected. It will be noted that the propagation rate increases with incidence relative to the axial component of the inlet velocity but is

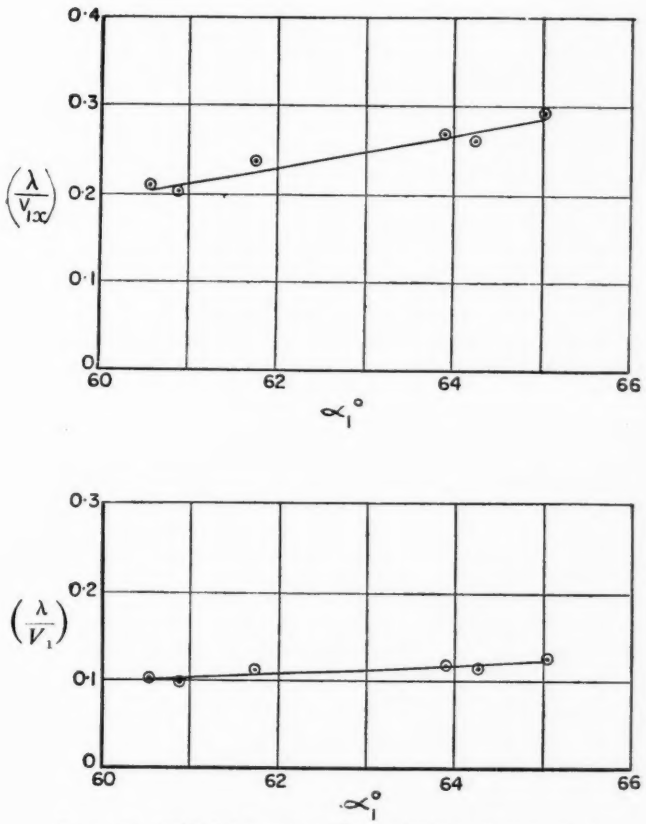

FIGURE 9. 66-bladed cascade. Mean velocities of propagation.

sensibly constant relative to the absolute inlet velocity. However, the similarity between the magnitude of the propagation velocities on the 9- and 66-bladed cascades is quite evident. It is apparently unnecessary to conduct stall propagation tests on many-bladed cascades in order to reproduce velocities of propagation equivalent to "infinite" conditions.

4. Consideration of Large Disturbance Effects

4.1. Reason for Discrepancies

Having discounted the first two suggested explanations for the discrepancy between small perturbation theory and experiment, the author concludes that the third alternative must be the correct one. The discrepancy is therefore attributed to the actual perturbations of the flow being inadequately represented by the small perturbations of the theory. Other explanations are possible but the author bases his conclusions on the following experimental results.

4.2. Flow Visualisation Tests

Tufts of goose-down placed in the trailing edge plane of the cascade pointed *upstream* during the passage of a stall cell. This showed that the velocity disturbances were of the same order of magnitude as the mean velocities, and that it would therefore be unlikely that they could be represented analytically by mathematically small perturbations.

4.3. Isolated Example of Fast Propagation on Cascade

The conclusion of Section 4.1 is further supported by the velocities of propagation measured at the lower end of the cascade at an inlet angle of 60° 34′ (*see* Fig. 7). The propagating stall cells observed at the top of the cascade ($X=0-3{\cdot}5$ ft.) did not reach the centre section of the cascade ($X=4$ ft.) where the flow was observed to be steady. Presumably, the inlet angle there was not sufficiently close to the stall to support propagation. However, due to some flow disturbance the propagation was observed to restart in the region $X=4{\cdot}5$ ft. In spite of the uniformity of the inlet conditions over the whole length of the cascade, the propagation restarted at a velocity which was nearly double that observed at the middle of the cascade. The value was checked to avoid the possibility of experimental error and the result was confirmed. The author considered that the disturbances which were observed to propagate at this high velocity might reasonably be expected to be initially small, since they originated at the edge of an unstalled disturbance-free section of the cascade. According to the author's reasoning, the observed velocities of propagation for these small disturbances should be closer to the values predicted by small perturbation theory than the velocities corresponding to the large disturbances originating at the severely stalled section at the top of the cascade. That this was confirmed by experiment lends weight to the conclusion linking the propagation velocity with the magnitude of the disturbance.

4.4. Test Results from a Single-Stage Compressor

Representative results from tests on a laboratory axial flow compressor also support the conclusion that the discrepancy between theory and experiment should be attributed to the large flow perturbations. It will be appreciated that the equations of the author's theory are directly applicable to the blade row of a compressor and the analysis is in no way restricted by the extra boundary condition that the spacing between cells must be a fraction of the circumference of the blade row.

During tests to investigate the occurrence of stall propagation on the rotor of the single-stage compressor, it was observed that the magnitude of the disturbances which formed each cell was of the same order as the normal blade wakes. It might be expected therefore that the measured velocity of propagation would show reasonable correlation with the theoretical predictions. In fact, this proved to be correct. The small perturbation theory predicted a value $\lambda/V_{1x}=1{\cdot}14$ which compares, not unfavourably, with the experimental result $\lambda/V_{1x}=0{\cdot}91$.

It should be emphasised that the compressor was so arranged that the rotor on which the tests were conducted was working in isolation, and was not subject to "interference" effects from nearby stator rows. No explanation can yet be offered for the reason why the rotor of this compressor should not develop a large scale disturbance. It is significant, however, that a test on a stator row of the compressor, also operating under "isolated" conditions, showed closer correlation with the cascade results than with the rotor results. The velocity of propagation on this isolated stator was 31 per cent of the local inlet axial velocity ($\lambda/V_{1x}=0{\cdot}31$). The author therefore concludes tentatively that the effect of rotation limits the magnitude of the disturbances forming the stall cells on the rotor. As a result, the measured velocity of propagation shows reasonable correlation with the value predicted by small perturbation theory.

5. Conclusions

(*i*) An analysis is presented which demonstrates the theoretical possibility of a small disturbance propagating along a two-dimensional row of axial flow compressor blades. The theory predicts that all harmonics of this disturbance should propagate at a particular velocity which is uniquely determined by the static pressure rise characteristic for the blading. The theory is applicable to both rotor and stator rows of axial flow compressors. In a particular test on a compressor rotor, it was demonstrated that the disturbances associated with each stall cell were of the same order of magnitude as the blade wakes. In this case the small perturbation theory predicted a velocity of propagation which was slightly greater than the observed value. It is therefore concluded that the theory is an adequate representation of the phenomenon, provided that the disturbances are small.

(*ii*) Correlation between the theory and experimental results from two-dimensional blade cascades was not so satisfactory. Propagation velocities were measured on 9-bladed and 66-bladed cascades. In both cases the propagation rate was approximately 30 per cent of the inlet axial velocity. Attempts to extend the small perturbation theory to include the effects of the finite time delay during which the flow in a blade passage readjusts itself to changed inlet conditions, were only partially successful. The extended theory predicted slightly lower velocities of propagation than the simple theory. The discrepancy between theory and cascade experiments was still approximately 400 per cent.

(*iii*) Flow visualisation tests showed that the flow within a blade passage reversed during the passage of a stall cell. This and other evidence leads to the conclusion that the discrepancy between theory and experiment is due to the fact that the disturbance velocities associated with the stall cells on the cascades were of the same order as the mean velocities. The small perturbation theory would then be inapplicable.

(*iv*) It appears that the large scale stall cell disturbances propagate at a lower velocity than that predicted by the small perturbation theory.

(*v*) It was noted that the disturbances which propagated at low velocity occurred on two straight cascades and on a compressor stator row, and that the higher velocity "small scale" propagation, which approached the value predicted by the small perturbation theory, occurred on a rotating blade row. It is therefore tentatively concluded that the motion of the blade row places a limit on the magnitude of the disturbance, which thus shows reasonably good correlation with the small perturbation theory.

(*vi*) The velocities of propagation measured on the 9- and 66-bladed cascades and on the stator row of a compressor, were all approximately 30 per cent of the inlet axial velocity. It is therefore unnecessary to conduct tests on many-bladed cascaded in order to simulate compressor conditions. To a first order, the results from a 9-bladed cascade are fully representative of the conditions on longer cascades.

(*vii*) A new phenomenon was noted on the 66-bladed cascade. As the stall cells propagated from one end of the cascade to the other, the rate of propagation decreased by approximately 30 per cent of the initial value. It was concluded that this could be explained in terms of the end effects imposed on the cascade flow by the wind tunnel.

References

1. Smith, A. G. and Fletcher, P. J. Note on the Surging of Four Low Speed Fans. Internal Note, National Gas Turbine Establishment, 1949.

2. Emmons, H. W., Pearson, C. E. and Grant, H. P. Compressor Surge and Stall Propagation. Paper No. 53-A-65 American Society of Mechanical Engineers Annual Meeting, November 1953.

3. Iura, T. and Rannie, W. D. Experimental Investigations of Propagating Stall in Axial Flow Compressors. *Transactions of the American Society of Mechanical Engineers*, Vol. 76, No. 3, April 1954.

4. Sears, W. R. On Asymmetric Flow in an Axial Flow Compressor Stage. *Journal of Applied Mechanics*, Vol. 20, No. 1, March 1954.

5. Marble, F. E. Propagation of Stall in a Compressor Blade Row. Technical Report No. 4, Guggenheim Jet Propulsion Centre, California Institute of Technology, January 1954.

6. Stenning, A. A. Stall Propagation in Cascades of Aerofoils. Readers' Forum, *Journal of the Aeronautical Sciences*, Vol. 21, October 1954.

7. Rhoden, H. G. Effects of Reynolds Number on the Flow of Air Through Cascades of Axial Flow Compressor Blades. R. & M. 2919, June 1952.

The Design of an Annular Entry to a Circular Duct

J. C. GIBBINGS, Ph.D.

(*Department of Fluid Mechanics, University of Liverpool*)

SUMMARY: This report describes the design of an annular entry for the axisymmetric flow into a circular duct, shaped so that the wall velocity gradients are favourable to the development of the boundary layer flow. As a first step the accelerating flow around a two-dimensional 90° duct bend with favourable gradients was obtained. This shape was modified and the axisymmetric flow pattern through it obtained by a combination of electrical analogue and relaxation methods and then checked by experiment. The favourable gradients were retained in the axisymmetric flow.

1. Introduction

The flow from an infinite volume into the entry of a duct of circular cross section can be smoothed by rounding the duct edge. For the two-dimensional version of this flow the known free streamline solution for an orifice flow can be used to provide a suitable boundary shape[1]. Then the velocity gradients along the wall would be either zero or favourable to the development of the boundary layer flow. For the axisymmetric flow from a finite reservoir, the solution given by Southwell and Vaisey[2] for the orifice and for the re-entrant Borda tube would similarly provide suitable boundaries.

However, it often happens that the surroundings of an entry are not placed symmetrically relative to the duct axis and this can result in the development of undesirable vortex flows. A way of avoiding this is to pass the flow into the duct through an annular entry, as illustrated in Fig. 1. Placing a wire gauze screen around the annulus, as shown, inhibits any circumferential flow asymmetry and its resulting vortex flow.

This paper describes the aerodynamic design of the annular entry shown in Fig. 1. In this figure the line AB forms an extension of the duct axis and the line CD is the generator of the cylinder of wire gauze. Avoidance of a stagnation point, and hence of a velocity gradient adverse to boundary layer development, requires a cone whose generator is marked BC. Point E is the joint between the entry and the duct.

Received February 1959.

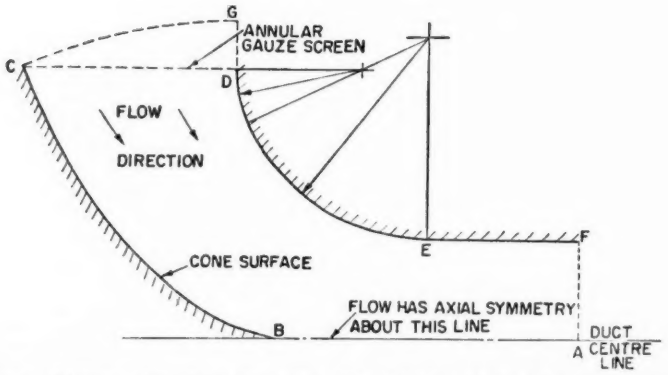

FIGURE 1. Diagram of the flow boundaries of the final bend before the working section.

The problem was to obtain surface shapes for the lines BC and DE along which there would be no pressure gradients adverse to the favourable development of the boundary layer flow. The various steps leading to a solution of this problem are now separably described. At each step an incompressible, irrotational flow model was postulated.

NOTATION

C_1, C_2 symbols defined in equations (4) and (5)

$h \equiv (dw/dz)^2$

K_1, K_2 symbols defined after equation (5)

q resultant velocity in two-dimensional flow

r ordinate of the sink in the hodograph plane

R radius of the circle in the hodograph plane

u, v x- and y-components of velocity in the two-dimensional flow, respectively

V resultant velocity in the axisymmetric flow

$w \equiv \phi + i\psi$

x, y ordinates in the physical plane

$z \equiv x + iy$

α velocity potential in the relaxation solution to the two-dimensional flow

β stream function in the relaxation solution to the two-dimensional flow

θ angle between the Ox-axis and the velocity vector in the two-dimensional flow

ρ radial ordinate in the axisymmetric flow

ϕ velocity potential

ψ stream function

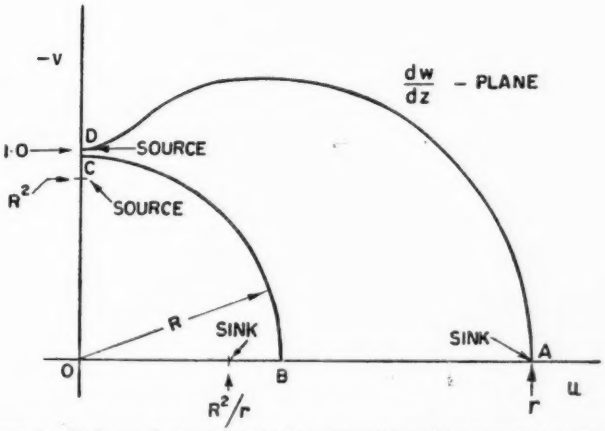

FIGURE 2. Hodograph plane for the two-dimensional flow in a 90° duct bend.

2. Two-Dimensional Exact Solution

As a first step a solution to the two-dimensional flow around a 90° bend is obtained. If the flow boundaries of Fig. 1 are regarded as containing a two-dimensional flow, then this can be represented by the hodograph plane boundaries, as sketched in Fig. 2.

The flow in the hodograph plane, or dw/dz-plane, is from a source at D to a sink at A. If BC is to be a boundary along which the velocity is constant, then this will be represented by a circle in the hodograph plane. Thus the velocity will increase monotonically both along CBA and along DA.

For BC to be a circle image sources and sinks are required at the inverse points[3].

Noting that
$$\frac{dw}{dz} = u - iv, \quad . \quad . \quad . \quad . \quad . \quad . \quad (1)$$

and writing the radius of the circle BC as R and the ordinates of A as $(r, 0)$, then, with $w \equiv \phi + i\psi$ and $z \equiv x + iy$, the flow in the dw/dz-plane is given by

$$w = \log \frac{[(dw/dz)^2 + 1]\,[(dw/dz)^2 + R^4]}{[(dw/dz)^2 - r^2]\,[(dw/dz)^2 - R^4/r^2]}. \quad . \quad . \quad . \quad (2)$$

Writing
$$h \equiv (dw/dz)^2,$$

equation (2) becomes a quadratic in h, the solution being

$$2(e^w - 1)\,h = e^w\,(r^2 + R^4/r^2) + R^4 + 1 + [\{e^w\,(r^2 + R^4/r^2) + 1 + R^4\}^2 - 4\,(e^w - 1)^2 R^4]^{1/2}, \quad . \quad . \quad (3)$$

where the sign before the square root is determined by putting $e^w = 0$ at point D.

Along AB, the requirement that h has to be wholly real while $R^2 \leqslant h \leqslant r^2$ leads to the conditions $\sin\psi = 0$, $\cos\psi = -1$.

If the tangents to AD and AB at A are at an angle greater than 90°, the resultant velocity would have a maximum between D and A. Thus, to obtain a monotonic velocity distribution along DA this angle is made 90° and hence, from equation (1), along AD, $\sin\psi = -1$, $\cos\psi = 0$.

Writing the radical in equation (3) as $C_1 + iC_2$ and expanding gives

$$C_1 = e^{2\phi}\cos 2\psi\,(r^2 - R^4/r^2)^2 + 2e^{\phi}\cos\psi\,\{(r^2 + R^4/r^2)(1 + R^4) + 4R^4\} + (1 - R^4)^2, \quad (4)$$

$$C_2 = e^{2\phi}\sin 2\psi\,(r^2 - R^4/r^2)^2 + 2e^{\phi}\sin\psi\,\{(r^2 + R^4/r^2)(1 + R^4) + 4R^4\}. \quad (5)$$

Further, writing $K_1 + iK_2 \equiv (C_1 + iC_2)^{1/2}$, noting that $h = q^2\,e^{i2\theta}$, where $\theta = \arg(dw/dz)$, and splitting equation (3) into real and imaginary parts gives

$$q^2\cos 2\theta = \frac{e^{2\phi}(r^2 + R^4/r^2) + e^{\phi}[\cos\psi\,\{(R^4 - r^2)(1 - 1/r^2) + K_1\} + K_2\sin\psi] - (1 + R^4 + K_1)}{2\,[e^{2\phi} - 2e^{\phi}\cos\psi + 1]}, \quad (6)$$

$$q^2\sin 2\theta = \frac{e^{\phi}\,[K_2\cos\psi - \{(R^4 + r^2)(1 + 1/r^2) + K_1\}\sin\psi] - K_2}{2\,[e^{2\phi} - 2e^{\phi}\cos\psi + 1]}. \quad (7)$$

where now $$K_2^2 = \frac{-C_1 + [C_1^2 + C_2^2]^{1/2}}{2}, \quad (8)$$

$$K_1^2 = \frac{C_2^2}{4K_2^2}. \quad (9)$$

For specified values of ϕ and ψ, successive use of equations (4) to (9) enabled corresponding values of u, v, and q to be computed.

Transformation into the z-plane was performed by integrating equation (1) numerically, it being rewritten as

$$d(x + iy) = \frac{u + iv}{q^2}\,d(\phi + i\psi),$$

so that
$$dx = \frac{1}{q^2}[ud\phi - vd\psi], \quad (10)$$

$$dy = \frac{1}{q^2}[vd\phi + ud\psi]. \quad (11)$$

These equations are in a convenient form for numerical integration when values of u, v, and q have been computed at regular intervals of ϕ and ψ.

As an example, numerical constants were chosen as

$$R = 0{\cdot}95, \qquad r = 2{\cdot}135.$$

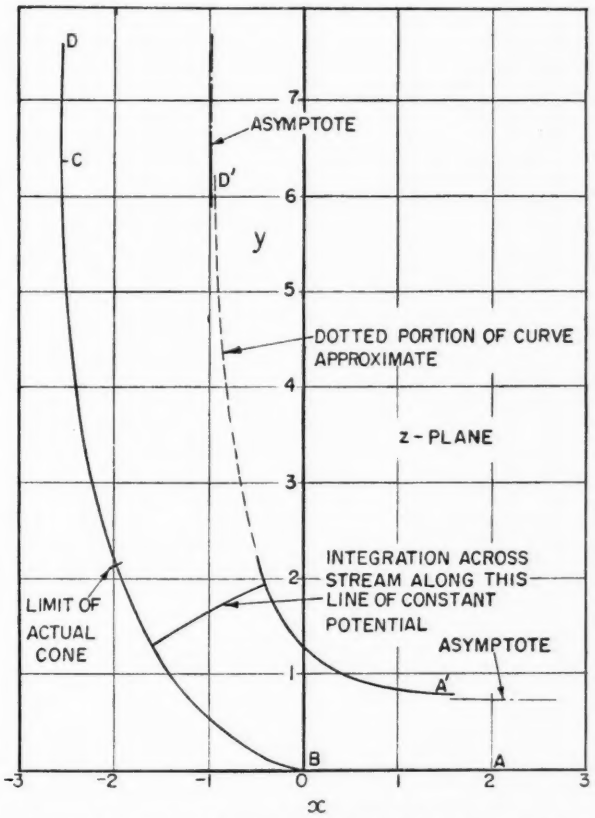

FIGURE 3. Boundary shape in the z-plane of the 90° duct bend.

Integration along BC was begun at point B, intervals being chosen as sufficiently small to retain four-figure accuracy. Near to the singularity at B rather small intervals were found necessary, but these could progressively be increased as integration proceeded. Point B was arbitrarily chosen as the origin in the z-plane.

Integration across the stream was performed along a constant potential line, chosen so as to be well away from the two singularities at B and C.

The resultant boundary shapes obtained are plotted in Fig. 3, together with the constant potential line along which integration was performed from one boundary to the other.

The bend shown in Fig. 3 is seen to be rather long in the y-direction. For structural reasons such a gentle turn is not usually feasible and an arbitrary limit placed upon the cone size is marked in Fig. 3. Also, for structural reasons, the curve $A'D'$ of Fig. 3 was modified in the model tests. The actual model shape is that given in Fig. 1.

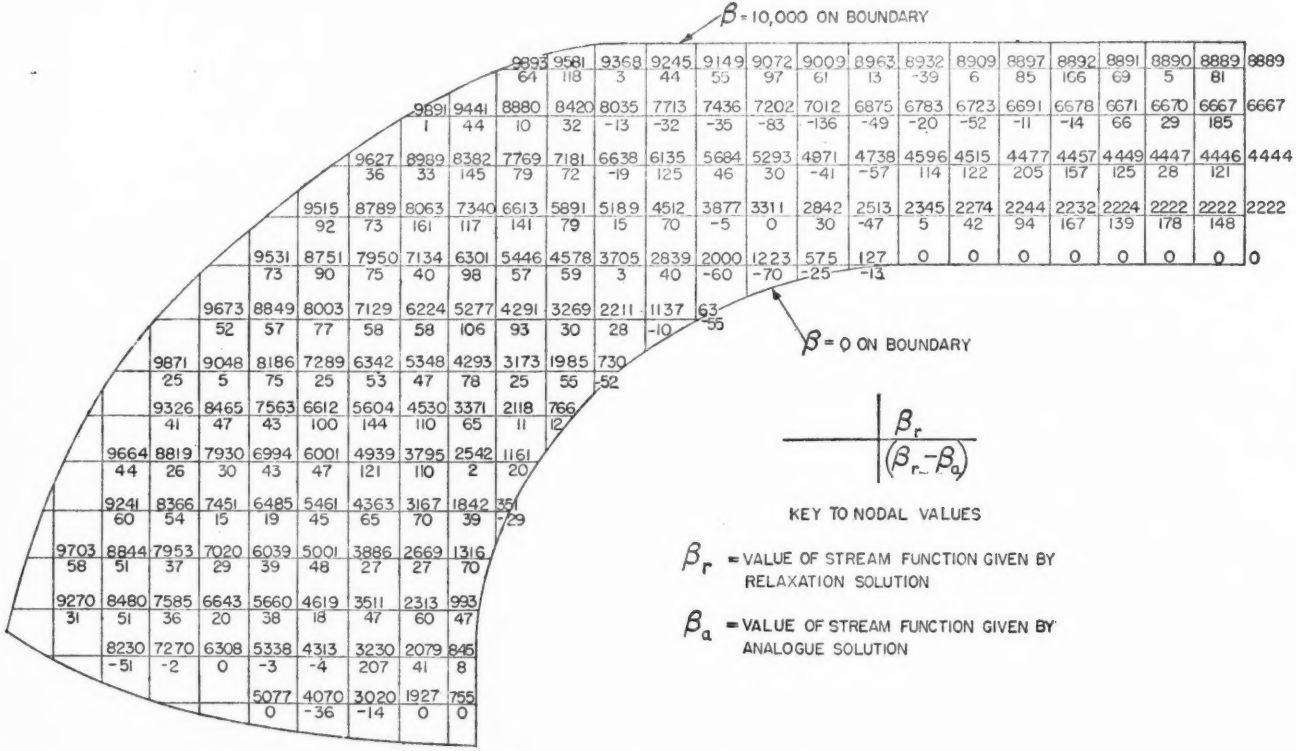
β = 10,000 ON BOUNDARY
β = 0 ON BOUNDARY
KEY TO NODAL VALUES
β_r = VALUE OF STREAM FUNCTION GIVEN BY RELAXATION SOLUTION
β_a = VALUE OF STREAM FUNCTION GIVEN BY ANALOGUE SOLUTION

FIGURE 4. Accepted values of β, the stream function, given by the relaxation solution for the two-dimensional flow with errors of the analogue solution.

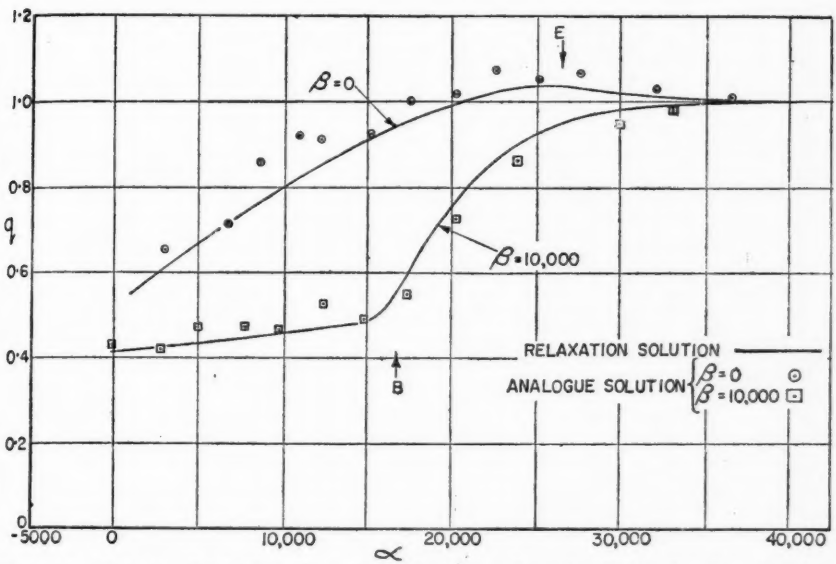

FIGURE 5. Velocity distribution along the walls in two-dimensional flow for the relaxation solution and for the analogue solution.

3. Two-Dimensional Flow past Actual Boundaries

3.1. Electrical Analogy Solution

As a first step towards a solution of the axisymmetric flow past the actual model boundaries, a solution to the two-dimensional flow within these walls was obtained.

A first approximation to the two-dimensional solution was obtained using the analogy to the distribution of electrical potential in a sheet of conducting paper[4]*. The conducting boundaries, marked *ABC* and *FEDG* in Fig. 1, were set up by masking them with cardboard templates and then spraying a coat of zinc metal. The insulated boundary, marked *AF* in Fig. 1, was placed at a position, adjudged sufficiently downstream, where the flow was regarded as uniform. The choice of the upstream boundary shape was more difficult. The boundary marked *CD* in Fig. 1 would be occupied in the real flow by gauze screens. Representation of it by an insulated boundary would result, because of the acute angle *DCB*, in a stagnation point at *C* in the analogue solution. An alternative boundary that was studied was the circular arc marked *GC* in Fig. 1 and which was normal to the walls at *C* and *G*. The paper was laid upon a wooden surface and pins driven through at each nodal point. These nodal points are shown in Fig. 4. The mesh size used was one inch. Solutions for the two boundary shapes *CD* and *CG* were obtained by the analogue and it was found that there was only a negligible difference

*The paper used was a conducting carbon paper with the commercial name of "Teledeltos."

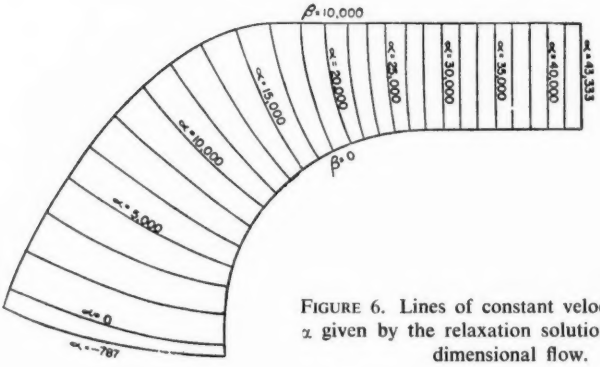

FIGURE 6. Lines of constant velocity potential, α given by the relaxation solution to the two-dimensional flow.

in potential values near to the walls in the region of B and E; it was considered that these were the important flow areas. The solution with the boundary CG (Fig. 1) was preferred because it avoided a stagnation point at C.

Values of the measured potential were then adopted as values of the stream function β. They were plotted against either of the x or y ordinates, depending upon which end of the bend was being considered; the resulting graphs were smoothed and the slopes at the wall measured graphically. This gave values of either $\partial\beta/\partial x$ or $\partial\beta/\partial y$. Then, knowing the appropriate value of the boundary slope dy/dx, the resultant velocity along the walls, q, was computed from

$$q^2 = u^2 + v^2$$
$$= u^2\,[1 + (v/u)^2]$$
$$= (\partial\beta/\partial y)^2\,[1 + (dy/dx)^2]$$

or, alternatively, $$q^2 = (\partial\beta/\partial x)^2\,[1 + 1/(dy/dx)^2].$$

Values so obtained are plotted, in Fig. 5, against the corresponding values of the velocity potential α. The relation between x and y and the corresponding value of α, as plotted in Fig. 6, was taken from the more accurate solution described in the next section.

The accuracy of the analogue results is also discussed in the next section.

3.2. Relaxation Solution

Using the analogue solution as a first approximation, a refined solution was readily obtained using relaxation methods[5].

The Laplace equation for the stream function β,

$$\frac{\partial^2\beta}{\partial x^2} + \frac{\partial^2\beta}{\partial y^2} = 0,$$

was replaced by the usual approximation

$$\sum_{1}^{4} \beta - 4\beta_0 = 0,$$

where suffixes indicate the nodal points illustrated in Fig. 7.

Near to the boundaries this approximation was modified in the usual way, using relations that have since been tabulated by Wu[6].

The mesh used was the same as was used for the analogue solution and is illustrated in Fig. 4.

The relaxation nodal values for β are given in Fig. 4. Also, in this figure, values of the error in the analogue solution are given. The fact that most of the errors are positive suggests that there might have been an error in the relative setting of the analogue boundaries to the mesh.

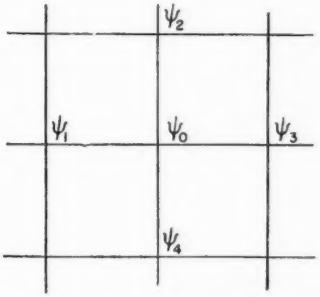

FIGURE 7. Relaxation mesh diagram.

Values of the two-dimensional velocity potential α were obtained from the values of β as follows. The values of β were numerically differentiated, using a three-point formula; then the Cauchy-Riemann equations,

$$\frac{\partial \alpha}{\partial x} = \frac{\partial \beta}{\partial y}$$

$$\frac{\partial \alpha}{\partial y} = -\frac{\partial \beta}{\partial x},$$

gave differentials of α. These were integrated by three-point formulae to give α values. For irregular mesh intervals near the boundaries, formulae such as those of Ref. 6 were again used. Lines of constant α were obtained by three-point interpolation formulae and are shown plotted in Fig. 6.

The wall velocity distribution was obtained as described for the analogue solution, except that the differential coefficients of β were obtained numerically using three-point formulae. Values are plotted against α as a continuous line in

Fig. 5. This provides a comparison with the analogue solution, indicating the accuracy of the latter. The largest analogue errors are seen to be of the order of 10 per cent, although smoothed curves, if drawn through the experimental points, would give a smaller error.

In Fig. 5 are marked the value of α corresponding to the tip of the cone (*B* in Fig. 1) and the value corresponding to the point at which the entry joins the duct (*E*).

The previously described exact solution from which the cone shape was derived gave a constant velocity along the cone. Despite the considerable modification of the opposite boundary wall and of the upstream boundary conditions, the velocity variation along the cone is a gentle one. Furthermore it is a favourable velocity gradient, the velocity rising in the flow direction*.

Along the other wall (*DEF* in Fig. 1), Fig. 5 shows a favourable velocity gradient over most of its length, with a slight adverse gradient from *E* onwards. The latter is a consequence of the parallel duct from *E* and cannot be avoided.

4. Axisymmetric Flow past Actual Boundaries

4.1. Relaxation Solution

Once a two-dimensional flow solution had been obtained a relaxation solution to the axisymmetric flow was readily performed, using a method previously suggested[7].

The equation for the stream function in the axisymmetric flow ψ is

$$\frac{\partial}{\partial x}\left(\frac{1}{\rho}\frac{\partial \psi}{\partial x}\right)+\frac{\partial}{\partial \rho}\left(\frac{1}{\rho}\frac{\partial \psi}{\partial \rho}\right)=0,$$

where ρ is the radius from the axis of symmetry.

This equation can be transformed into

$$\frac{\partial}{\partial \alpha}\left(\frac{1}{\rho}\frac{\partial \psi}{\partial \alpha}\right)+\frac{\partial}{\partial \beta}\left(\frac{1}{\rho}\frac{\partial \psi}{\partial \beta}\right)=0,$$

so that solution in the $\alpha\beta$-plane involves only regular mesh sizes.

The approximation to this equation is given in Ref. 7 as

$$\sum_1^4(\rho\psi)-3\rho_0\sum_1^4\psi-\psi_0\sum_1^4\rho+12\psi_0\rho_0=0.$$

This was solved by relaxation methods in the usual way.

The velocity at the walls in the axisymmetric flow, *V*, was computed from[7]

$$V=\frac{q}{\rho}\frac{\partial \psi}{\partial \alpha},$$

*The singularity at *B* is masked by the relaxation solution whose mesh straddles this point.

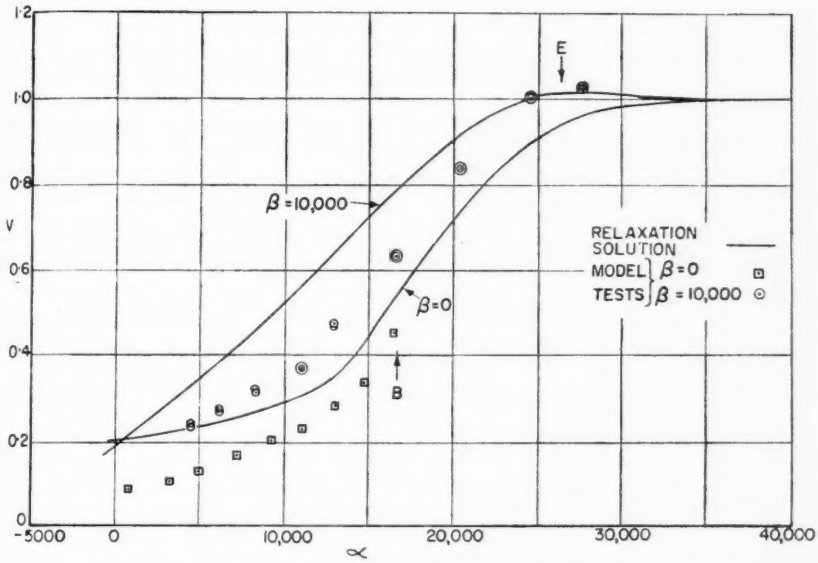

FIGURE 8. Velocity distribution along the walls in axisymmetric flow for the relaxation solution and from experiment.

q being the velocity in the two-dimensional flow. Values of $\partial\psi/\partial\alpha$ were computed from the relaxation solution, using a three-point numerical differentiation formula.

Values of V are plotted against the two-dimensional velocity potential in Fig. 8. Again, the tip of the cone is marked B (Fig. 1) and the end of the other wall is marked E.

In comparison with the two-dimensional case, it is seen that the velocity gradient along the cone surface is now more favourable. Along the other surface the velocity peak at E is reduced and the adverse gradient along the straight wall EF is correspondingly lessened.

4.2. Experimental Wall Velocity Distribution

A model of the entry was used to measure the velocity distribution.

The pressure distribution along the cone was obtained from the readings from a series of static hole tappings. Along the other wall it was obtained by the successive fitting of a static tube close to the surface in a number of positions.

Considerable difficulties were encountered in the experiments because of the low air velocities occurring; at the entry to the bend they were of the order of 0·4 ft./sec.

The experimental velocity values are plotted in Fig. 8 for comparison with the calculated values. The positions of the measured values are again related to the two-dimensional velocity potential, α, by use of the relaxation solution (Section 3.2).

The experimental values are seen to be consistently lower than the calculated values. Although no definite explanation of this discrepancy can be advanced, it corresponds at the low speed end to a zero error of 0·012 in. of water or, alternatively, to an error of two per cent in $\frac{1}{2}\rho V^2$ in the working section, both of which could be possible explanations. Measured boundary layer thicknesses were found to be too small to account for these discrepancies.

However, what is important is that the experiments confirm the presence of favourable velocity gradients along all of the cone surface and along most of the other wall, except beyond where the slight velocity peak is confirmed.

Thus a satisfactory design was obtained.

5. Conclusions

The boundary shape for the axisymmetric flow through an annular entry to a duct was obtained from a two-dimensional flow solution in which all the velocity gradients were favourable to the development of the real boundary layer flow. This shape was found, both by calculation and by experiment, to be satisfactory in the axisymmetric flow where the velocity gradients became more favourable.

Incidental to this, it was found that an electrical analogue to the two-dimensional flow using conducting paper gave velocity values having a maximum error of about ten per cent.

Acknowledgments

In the work described in this paper, the author was greatly assisted by various colleagues, in particular R. L. Maltby, Mrs. D. S. Capps and J. H. Anderson, to whom he is much indebted.

References

1. Lamb, H. *Hydrodynamics.* 3rd Edition, Para. 74, Cambridge University Press, 1906.
2. Southwell, R. V. and Vaisey, G. Relaxation Methods Applied to Engineering Problems. XII. Fluid Motions Characterised by Free Streamlines. *Phil. Trans. Roy. Soc.* A, Vol. 240, p. 117, 1946.
3. Milne-Thomson, L. M. *Theoretical Hydrodynamics.* 2nd Edition, Sec. 8.61, Macmillan, 1949.
4. Scott, R. E. An Analog Device for Solving the Approximation Problem of Network Synthesis. Research Laboratory of Electronics, Technical Report 137, Massachusetts Institute of Technology, June 1950.
5. Southwell, R. V. *Relaxation Methods in Theoretical Physics.* Oxford University Press, 1946.
6. Wu, C. H. Formulas and Tables of Coefficients for Numerical Differentiation with Function Values Given at Unequally Spaced Points and Application to Solution of Partial Differential Equations. N.A.C.A. T.N. 2214.
7. Whitehead, L. G., Wu, L. Y. and Waters, M. H. L. Contracting Ducts of Finite Length. *Aeronautical Quarterly,* Vol. 2, p. 254, February 1951.

Stresses Around Reinforced Elliptical Holes, with Applications to Pressure Cabin Windows

W. H. WITTRICK

(*Department of Aeronautical Engineering, University of Sydney*)

SUMMARY: An analytical solution, using complex variable methods, is given for the problem of the stress distribution due to an elliptical hole, reinforced around its boundary, in a plane sheet subjected at infinity either to an arbitrary constant stress system or to a bending type stress system. Numerical results were obtained for a wide range of parameters, including three different shapes of ellipse, and ten different amounts of reinforcement. Poisson's ratio was assumed to be 1/3.

These results were used to investigate the stress concentrations arising at elliptical pressure cabin windows due to the pressurisation stresses. It is shown that, for each shape of ellipse, there is a limit to the reduction in stress concentration factor which can be achieved by increasing the weight of reinforcement; beyond this the stress concentration factor rises again. It is also shown that, for a hole with axes in the ratio $\sqrt{2}$, a stress concentration factor as low as 1·09 may be achieved by using a uniform reinforcement whose weight is only about half that required for Mansfield's neutral hole.

1. Introduction

Considerable attention has been paid in recent years to the stress distribution around window openings in pressurised fuselages and most of the theoretical work available refers to circular or elliptical holes. To the author's knowledge it has always been assumed that the problem may be idealised as that of a hole in a flat sheet, subjected to the appropriate stress condition at infinity. Doubt has been thrown upon this idealisation following some experimental work by Richards[1]; despite this, however, the same assumption will be made here.

The problem of the unreinforced elliptical hole was first solved by Inglis[2] and more recently that of an elliptical hole reinforced by means of a compact member attached to its boundary has been investigated by Wells[3] and Hicks[4]. Both of these authors analysed the problem in a semi-inverse manner, making use of Inglis's solution; they were able to obtain exact solutions provided that they were willing to accept the non-uniformity of the cross-sectional area of the reinforcement prescribed by their solutions. In many cases the amount of non-uniformity was quite small, and useful results were thereby obtained.

Received April 1959.

Mansfield[5] went further still, and investigated the requirements for a neutral hole, defined as a hole of such a shape and with such a distribution of reinforcement around the boundary that the stresses in the surrounding sheet are unchanged. For the case of a sheet subjected to uniform stresses at infinity, one principal stress being twice the other, as in a fuselage due to pressurisation, he showed that the neutral hole is an ellipse with its major axis parallel to the greater of the two principal stresses and equal to $\sqrt{2}$ times the minor axis. A non-uniform reinforcing member is required, the cross-sectional area at the end of the major axis being roughly three times that at the end of the minor axis, for practical values of Poisson's ratio. Furthermore, the total weight of reinforcement required is about three times the weight of sheet removed in forming the hole.

The primary purpose of the present paper is to provide some systematic numerical data on the stresses around elliptical holes of various shapes, with various amounts of uniform reinforcement, and with special reference to the problem of the pressure cabin window.

It is found that, by using only slightly more than half the weight of reinforcement required for Mansfield's neutral hole, but distributed uniformly around the periphery, an elliptical hole with a ratio of axes equal to $\sqrt{2}$ produces a stress concentration factor as low as 1·09 when the principal stresses at infinity are in the ratio of 2:1.

In the process of the analysis it was found that a simple exact solution can be obtained for the stress distribution around a neutral elliptical hole due to loadings other than that for which it is neutral.

The analysis employs the complex variable methods developed by Muskhelishvili[6] *et al* whereas Inglis[2], Wells[3] and Hicks[4] all used real variable theory with an elliptical co-ordinate system. For this particular problem there is not a very great advantage in using complex variables. However the analysis can readily be adapted to any shape of hole, provided that the transformation function which maps the region outside the boundary of the hole on to the region outside the unit circle is a known polynomial. For this reason it was felt that a complex variable solution to the problem would be of wider interest.

Notation

x, y Cartesian co-ordinates

$z = x + iy$

a, b semi-axes of the ellipse, parallel to x and y

$R = \frac{1}{2}(a+b)$

$m = (a-b)/(a+b)$

ξ angle between the x-axis and the tangent to the ellipse

r radius of curvature of the ellipse

t thickness of the sheet

A cross-sectional area of the reinforcement

$K = Rt/A$

n, s co-ordinates normal and tangential to the ellipse

ζ complex co-ordinates in the circle plane

θ polar angle in the ζ-plane

$\sigma = e^{i\theta}$. Complex co-ordinate on the unit circle

$P = 1 + m^2 - 2m \cos 2\theta$

E Young's modulus

G shear modulus

μ Poisson's ratio

$Q = 2P/[KP^{3/2} + (1 - m^2)(1 + \mu)]$

T tension in the reinforcement

f_1, f_2 tensile stresses at infinity in the x, y directions

S shear stress at infinity referred to the x, y directions

p constant defining the magnitude of a bending stress distribution at infinity

$U(x, y)$ Airy stress function

u, v displacements of a point in the x, y directions

$\Omega(\zeta)$ function which transforms the region outside the hole on to the region outside the unit circle

$\phi_0(z)$, $\chi_0(z)$ *see* equation (2)

$\psi_0(z)$ *see* equation (5)

Note: A prime (′) on a function denotes differentiation.

A bar over a complex quantity denotes the conjugate value.

2. Basic Formulae for Stresses and Displacements in Complex Form

In this section the basic equations of the two-dimensional theory of elasticity will be summarised in complex form[6]. Any system of plane stress may be defined in terms of the Airy stress function $U(x, y)$ which satisfies the biharmonic equation. Introducing complex variables z and $\bar{z}$ by the equations

$$z = x + iy, \qquad \bar{z} = x - iy \quad . \quad . \quad . \quad . \quad . \quad (1)$$

the biharmonic equation becomes

$$\frac{\partial^4 U}{\partial z^2 \partial \bar{z}^2} = 0$$

and its general (real) solution is

$$U=\bar{z}\phi_0(z)+z\overline{\phi_0(z)}+\chi_0(z)+\overline{\chi_0(z)}, \quad . \quad . \quad . \quad (2)$$

where $\phi_0(z)$ and $\chi_0(z)$ are functions analytic within the region concerned, and a bar denotes the conjugate complex value.

The normal stresses, $\widehat{xx}$ and $\widehat{yy}$, and the shear stress $\widehat{xy}$ are given by the equations

$$(\widehat{xx}+\widehat{yy}) \quad =4\partial^2U/\partial z\partial\bar{z}=4\,[\phi_0'(z)+\overline{\phi_0'(z)}] \quad . \quad . \quad (3)$$

$$(\widehat{yy}-\widehat{xx}+2i\widehat{xy})=4\partial^2U/\partial z^2 \quad =4\,[\bar{z}\phi_0''(z)+\psi_0'(z)] \quad . \quad . \quad (4a)$$

$$\text{or} \quad (\widehat{yy}-\widehat{xx}-2i\widehat{xy})=4\partial^2U/\partial\bar{z}^2 \quad =4\,[z\overline{\phi_0''(z)}+\overline{\psi_0'(z)}]. \quad . \quad . \quad (4b)$$

where $$\psi_0(z)=\chi_0'(z) \quad . \quad . \quad . \quad . \quad . \quad . \quad . \quad (5)$$

and a prime (′) denotes differentiation.

The displacements u and v of the point (x, y) in the x and y directions are given by the complex equation

$$G(u+iv)=\kappa\phi_0(z)-z\overline{\phi_0'(z)}-\overline{\psi_0(z)} \quad . \quad . \quad . \quad . \quad (6)$$

where $\kappa=(3-\mu)/(1+\mu)$, μ is Poisson's ratio and G is the shear modulus.

Convenient formulae for the stresses $\widehat{ss}$, $\widehat{nn}$, and $\widehat{sn}$, referred to a new pair of axes s and n, formed by rotating the x and y axes through an angle ξ (Fig. 1) are as follows.

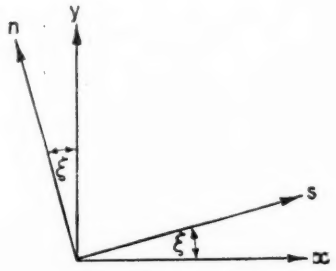

FIGURE 1. Rotation of axes.

$$(\widehat{ss}+\widehat{nn}) \quad = \widehat{xx}+\widehat{yy} \quad . \quad . \quad . \quad . \quad . \quad . \quad (7)$$

$$(\widehat{nn}-\widehat{ss}+2i\widehat{sn}) = (\widehat{yy}-\widehat{xx}+2i\widehat{xy})\, e^{2i\xi} \quad . \quad . \quad . \quad (8a)$$

$$\text{or} \quad (\widehat{nn}-\widehat{ss}-2i\widehat{sn}) = (\widehat{yy}-\widehat{xx}-2i\widehat{xy})\, e^{-2i\xi} \quad . \quad . \quad . \quad (8b)$$

In the case of an infinite sheet with a hole surrounding the origin, subjected to stresses at infinity whose values are bounded, the functions $\phi_0(z)$ and $\psi_0(z)$ may be expanded as series in descending powers of z, starting with the first power, thus

$$\phi_0(z) = \alpha z + \alpha_0 + \alpha_1 z^{-1} + \alpha_2 z^{-2} + \ldots \ldots \quad . \quad . \quad . \quad (9)$$

$$\psi_0(z) = \beta z + \beta_0 + \beta_1 z^{-1} + \beta_2 z^{-2} + \ldots \ldots \quad . \quad . \quad . \quad (10)$$

where the α_n and β_n are in general complex.

Expansions of this type will be used to obtain solutions for the cases where the stress is uniform at infinity. In the other case considered, that of a bending stress distribution at infinity, it is necessary to include terms in z^2 in the series (9) and (10).

3. The Effect of Symmetry

3.1. General

In all the problems discussed here there is symmetry of one type or another about the x and y axes. The effect of this is to restrict the type of term which can occur in the expansions for $\phi_0(z)$ and $\psi_0(z)$, and this will now be considered in detail.

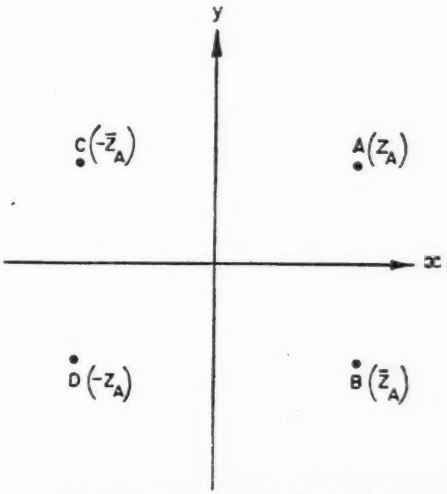

FIGURE 2. Image points in the z-plane.

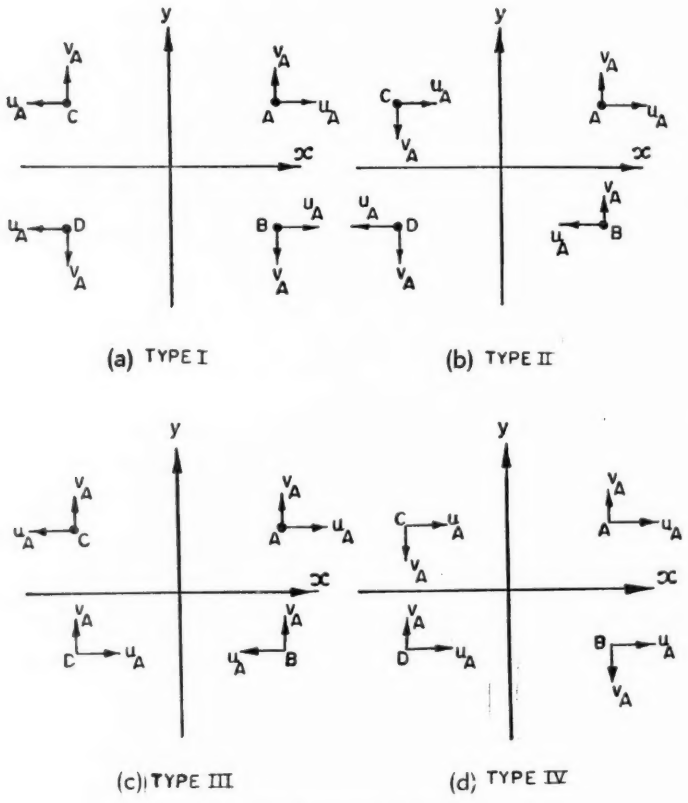

FIGURE 3. The four types of symmetry.

Figure 2 shows a point A, whose complex co-ordinate is z_A, together with its image points B and C in the x and y axes respectively. The complex co-ordinates of B and C are $\bar{z}_A$ and $-\bar{z}_A$ respectively. Then the displacements of the points A, B and C are found from equation (6) as follows*

$$\left.\begin{aligned} G(u_A+iv_A) &= \kappa\phi_0(z_A) \quad -z_A\bar{\phi}_0'(\bar{z}_A) \quad -\bar{\psi}_0(\bar{z}_A) \\ G(u_B+iv_B) &= \kappa\phi_0(\bar{z}_A) \quad -\bar{z}_A\bar{\phi}_0'(z_A) \quad -\bar{\psi}_0(z_A) \\ G(u_C+iv_C) &= \kappa\phi_0(-\bar{z}_A)+\bar{z}_A\bar{\phi}_0'(-z_A)-\bar{\psi}_0(-z_A) \end{aligned}\right\} \quad . \quad . \quad (11)$$

*Note the following definitions:—

If $\phi(z)=\alpha z+\alpha_0+\alpha_1 z^{-1}+\ \ldots\ .$

then $\bar{\phi}(z)=\bar{\alpha}z+\bar{\alpha}_0+\bar{\alpha}_1 z^{-1}+\ \ldots\ .$

and $\overline{\phi(\bar{z})}=\bar{\phi}(\bar{z})=\bar{\alpha}\bar{z}+\bar{\alpha}_0+\bar{\alpha}_1\bar{z}^{-1}+\ \ldots\ .$

3.2. Type I Symmetry

Consider first the case where only *odd powers* of z are included in the expansions for $\phi_0(z)$ and $\psi_0(z)$ and where *all the coefficients are real, i.e.*

$$\phi_0(z)=\alpha z+\alpha_1 z^{-1}+\alpha_3 z^{-3}+\ldots\ldots \quad ; \quad \alpha_n \text{ real.}$$

$$\psi_0(z)=\beta z+\beta_1 z^{-1}+\beta_3 z^{-3}+\ldots\ldots \quad ; \quad \beta_n \text{ real.}$$

It is easy to see that in this case

$$\phi_0(z)=\bar{\phi}_0(z)=-\bar{\phi}_0(-z),$$

with similar expressions involving ψ_0 instead of ϕ_0.

Hence from equations (11) or their conjugates it is seen that

$$(u_A+iv_A)=(u_B-iv_B)=-(u_C-iv_C).$$

i.e.
$$u_A=\quad u_B=-u_C$$

$$v_A=-v_B=\quad v_C.$$

This type of symmetry is illustrated in Fig. 3(*a*) and it is clear that this applies to the problem of a hole, symmetrical about both the x and y axes, in a sheet subjected to a uniform tensile stress at infinity in either the x or the y directions, or both.

3.3. Type II Symmetry

Suppose now that the expansions of $\phi_0(z)$ and $\psi_0(z)$ contain only *odd powers* of z, but that *the coefficients are purely imaginary, i.e.*

$$\phi_0(z)=i(\alpha z+\alpha_1 z^{-1}+\alpha_3 z^{-3}+\ldots.) \quad ; \quad \alpha_n \text{ real.}$$

$$\psi_0(z)=i(\beta z+\beta_1 z^{-1}+\beta_3 z^{-3}+\ldots.) \quad ; \quad \beta_n \text{ real.}$$

Then
$$\phi_0(z)=-\bar{\phi}_0(z)=-\phi_0(-z),$$

and it follows from equations (11) that

$$(u_A+iv_A)=-(u_B-iv_B)=(u_C-iv_C)$$

i.e.
$$u_A=-u_B=\quad u_C$$

$$v_A=\quad v_B=-v_C.$$

This is illustrated in Fig. 3(*b*) and applies to the problem of a hole, symmetrical about the x and y axes, in a sheet subjected at infinity to a uniform shear stress parallel to the x and y directions.

3.4. Type III Symmetry

If the expansions of $\phi_0(z)$ and $\psi_0(z)$ contain only *even powers* of z, and *the coefficients are purely imaginary, i.e.*

$$\phi_0(z) = i(\alpha z^2 + \alpha_0 + \alpha_2 z^{-2} + \ldots) \quad ; \quad \alpha_n \text{ real}$$

$$\psi_0(z) = i(\beta z^2 + \beta_0 + \beta_2 z^{-2} + \ldots) \quad ; \quad \beta_n \text{ real},$$

it follows in an exactly similar way that

$$u_A = -u_B = -u_C$$

$$v_A = \quad v_B = \quad v_C.$$

This is illustrated in Fig. 3(*c*) and is applicable to the problem of a hole, symmetrical about both the x and y axes, in a sheet subjected to bending stresses at infinity parallel to the x direction, the stress being zero on the x axis.

3.5. Type IV Symmetry

Finally, if the expansions of $\phi_0(z)$ and $\psi_0(z)$ contain only *even powers* of z, and *the coefficients are real, i.e.*

$$\phi_0(z) = \alpha z^2 + \alpha_0 + \alpha_2 z^{-2} + \ldots \quad ; \quad \alpha_n \text{ real}$$

$$\psi_0(z) = \beta z^2 + \beta_0 + \beta_2 z^{-2} + \ldots \quad ; \quad \beta_n \text{ real},$$

it follows that

$$u_A = \quad u_B = \quad u_C$$

$$v_A = -v_B = -v_C.$$

This is shown in Fig. 3(*d*) and represents the same sort of symmetry as Type III, but turned through a right angle.

4. Boundary Conditions for a Reinforced Hole

It will be assumed that the boundary of the hole is reinforced by a compact member of cross-sectional area A, which may be constant or may vary with the peripheral co-ordinate s. It will also be assumed that, compared with its extensional rigidity, the relevant flexural rigidity of the member is sufficiently small to neglect the shear forces in it compared with the tension T.

Figure 4 shows an element of the reinforcement, together with a triangular element of the attached sheet. This element is in equilibrium under the action of the tensions T and $(T+dT)$ at the ends of the reinforcement, together with the stresses $\widehat{xx}$, $\widehat{yy}$ and $\widehat{xy}$ on the edges of the element of sheet.

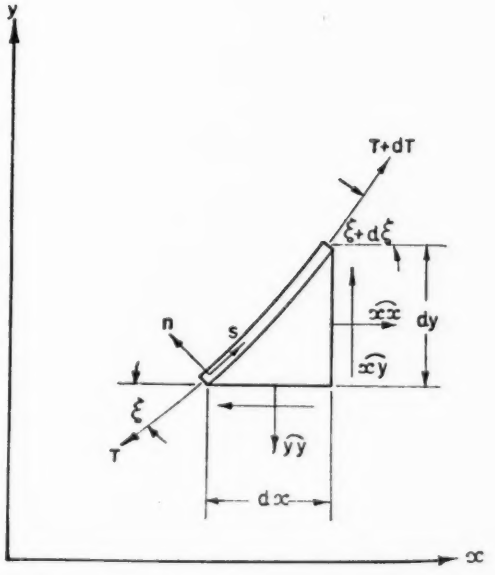

FIGURE 4. Forces on an element of reinforcement and attached sheet.

Hence, resolving horizontally and vertically:—

$$d(T\cos\xi) = t(\widehat{xy}\,dx - \widehat{xx}\,dy)$$

and $$d(T\sin\xi) = t(\widehat{yy}\,dx - \widehat{xy}\,dy),$$

where t is the sheet thickness and ξ is the slope of the boundary of the hole.

On multiplying the second of these equations by i and adding it to the first, we obtain the complex equation

$$d(Te^{i\xi}) = t(\widehat{xy} + i\widehat{yy})\,dx - t(\widehat{xx} + i\widehat{xy})\,dy.$$

Now, from equations (1),

$$dx = \tfrac{1}{2}(dz + d\bar{z}) \;; \qquad dy = -\tfrac{1}{2}i(dz - d\bar{z})$$

and the complex equation becomes

$$d(Te^{i\xi}) = \tfrac{1}{2}ti\,[(\widehat{xx} + \widehat{yy})\,dz + (\widehat{yy} - \widehat{xx} - 2i\widehat{xy})\,d\bar{z}].$$

Hence, on using equations (3) and (4*b*),

$$d(Te^{i\xi}) = 2ti\left[\frac{\partial^2 U}{\partial z \partial \bar{z}}\,dz + \frac{\partial^2 U}{\partial \bar{z}^2}\,d\bar{z}\right]$$

$$= 2ti\,d(\partial U/\partial \bar{z}).$$

On integration, it follows that

$$Te^{i\xi} = 2ti\left(\frac{\partial U}{\partial \bar{z}} + \alpha\right),$$

where α is a constant of integration, in general complex.

This equation may be rewritten in the form

$$Te^{i\xi} = 2ti\,\frac{\partial}{\partial \bar{z}}(U + \alpha\bar{z} + \bar{\alpha}z)$$

and it is easy to see from equation (2) that the terms $(\alpha\bar{z} + \bar{\alpha}z)$ may be absorbed in U, since they correspond to the addition of a constant α to the function $\phi_0(z)$. Hence, without loss of generality, we have

$$\frac{T}{2t} = ie^{-i\xi}\frac{\partial U}{\partial \bar{z}} = ie^{-i\xi}[\phi_0(z) + z\overline{\phi_0'(z)} + \overline{\psi_0(z)}]. \quad . \quad . \quad . \quad (12)$$

Now the left hand side of this equation is essentially real. It follows therefore that the right hand side of equation (12) is equal to its conjugate complex value, from which we obtain the first condition to be satisfied on the boundary, namely

$$e^{i\xi}[\overline{\phi_0(z)} + \bar{z}\phi_0'(z) + \psi_0(z)] + e^{-i\xi}[\phi_0(z) + z\overline{\phi_0'(z)} + \overline{\psi_0(z)}] = 0. \quad . \quad (13)$$

The second condition arises from the fact that the strain in the reinforcement is equal to the peripheral strain of the attached sheet, giving the equation

$$\frac{T}{A} = \widehat{ss} - \mu\widehat{nn}, \quad . \quad . \quad . \quad . \quad (14)$$

where $\widehat{ss}$ and $\widehat{nn}$ are the direct stresses in the sheet along and perpendicular to the boundary, respectively, and μ is Poisson's ratio.

Now from equations (3), (4), (7) and (8) it is seen that

$$\widehat{nn} - \widehat{ss} = 2\left[\frac{\partial^2 U}{\partial z^2}e^{2i\xi} + \frac{\partial^2 U}{\partial \bar{z}^2}e^{-2i\xi}\right] \quad . \quad . \quad . \quad . \quad (15)$$

and $$\widehat{nn} + \widehat{ss} = 4\,\frac{\partial^2 U}{\partial z \partial \bar{z}} \quad . \quad . \quad . \quad . \quad . \quad . \quad . \quad (16)$$

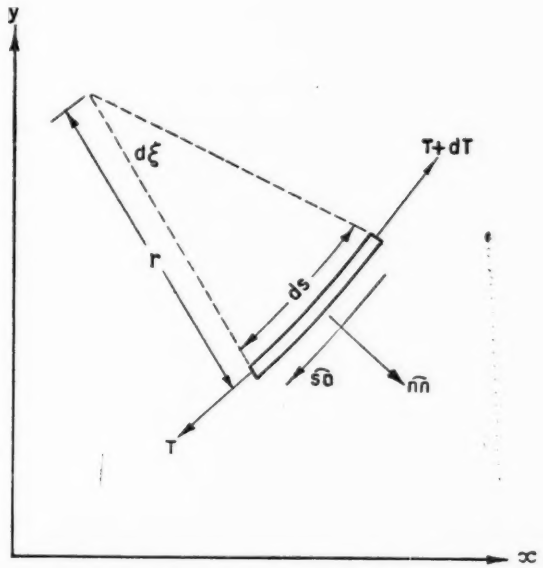

FIGURE 5. Forces on an element of reinforcement.

Hence, from equations (14), (15) and (16),

$$\frac{T}{A} = 2(1-\mu)\frac{\partial^2 U}{\partial z \partial \bar{z}} - (1+\mu)\left[\frac{\partial^2 U}{\partial z^2} e^{2i\xi} + \frac{\partial^2 U}{\partial \bar{z}^2} e^{-2i\xi}\right] \quad . \quad . \quad (17)$$

Finally, substitution of equation (2) into the right hand side of equation (17) gives

$$\frac{T}{A} = 2(1-\mu)[\phi_0'(z) + \overline{\phi_0'(z)}] - (1+\mu)[e^{2i\xi}\{\bar{z}\phi_0''(z) + \psi_0'(z)\} + e^{-2i\xi}\{z\overline{\phi_0''(z)} + \overline{\psi_0'(z)}\}]. \quad . \quad . \quad . \quad (18)$$

It will be seen later that equation (13) essentially enables us to determine the function $\psi_0(z)$, and hence T, in terms of $\phi_0(z)$, and equation (18) then becomes an equation from which $\phi_0(z)$ can be determined, thereby completing the solution.

Equation (13) was obtained by considering the equilibrium of the element of reinforcement plus attached sheet shown in Fig. 4. However, a consideration of the equilibrium of an element of reinforcement only, as shown in Fig. 5, leads to equations which form a useful check later. Thus, resolving in directions normal and tangential to the element, we have relations (19) and (20):—

$$\widehat{nn} = \frac{T}{tr} \quad . \quad . \quad . \quad . \quad . \quad . \quad . \quad . \quad (19)$$

$$\text{and} \quad \widehat{sn} = \frac{1}{t}\frac{dT}{ds} = \frac{d}{ds}(r\widehat{nn}), \qquad . \quad . \quad . \quad (20)$$

where r is the radius of curvature of the boundary.

Taken in conjunction with equation (14), equation (19) gives

$$\widehat{ss} = \widehat{nn}\left(\mu + \frac{tr}{A}\right) \qquad . \quad . \quad . \quad . \quad . \quad (21)$$

5. Transformation of the Ellipse

Suppose that the boundary of the hole in the z-plane is the ellipse

$$\frac{x^2}{a^2} + \frac{y^2}{b^2} = 1,$$

as shown in Fig. 6.

The function which conformally transforms the region outside this ellipse into the region outside the unit circle in the ζ-plane is

$$z = \Omega(\zeta) = R\left(\zeta + \frac{m}{\zeta}\right), \qquad . \quad . \quad . \quad . \quad (22)$$

where the constants R and m are related to the semi-axes a and b by the equations

$$a = R(1+m) \; ; \qquad b = R(1-m) \qquad . \quad . \quad . \quad . \quad (23)$$

or, alternatively,

$$R = \tfrac{1}{2}(a+b) \; ; \qquad m = \frac{a-b}{a+b}. \qquad . \quad . \quad . \quad . \quad (24)$$

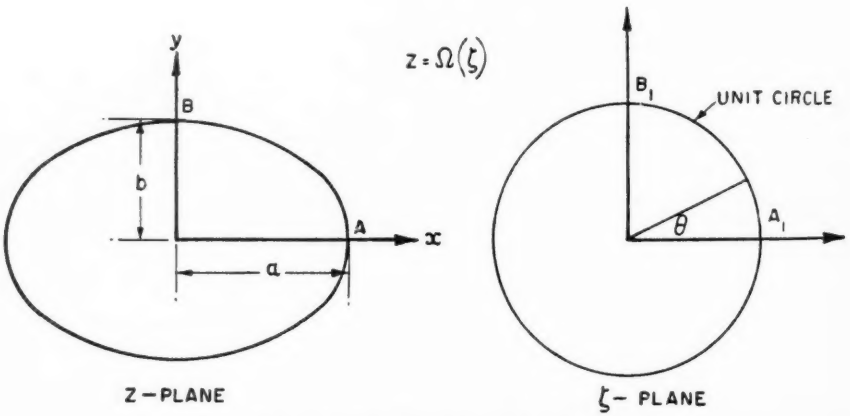

FIGURE 6. Transformation of the ellipse.

On the boundary of the unit circle, we have

$$\zeta = e^{i\theta} = \sigma, \text{ say,} \quad . \quad . \quad . \quad . \quad . \quad (25)$$

so that, from (22), the parametric equation of the ellipse is

$$x = R(1+m)\cos\theta = a\cos\theta$$

$$y = R(1-m)\sin\theta = b\sin\theta, \quad . \quad . \quad . \quad . \quad (26)$$

where θ is the polar angle in the ζ-plane (Fig. 6).

On the boundary of the ellipse

$$dz = |dz|\, e^{i\xi}.$$

Hence $$e^{i\xi} = \frac{dz}{|dz|} = \frac{\Omega'(\sigma)}{|\Omega'(\sigma)|}\,\frac{d\sigma}{|d\sigma|}$$

Also $$d\sigma = ie^{i\theta}d\theta = i\sigma d\theta$$

and $$|d\sigma| = d\theta,$$

so that $$-ie^{i\xi} = \frac{\sigma\Omega'(\sigma)}{|\Omega'(\sigma)|}. \quad . \quad . \quad . \quad . \quad . \quad (27)$$

Now $$|\Omega'(\sigma)| = [\Omega'(\sigma)\,\overline{\Omega'(\sigma)}]^{1/2}$$

$$= R[(1-m/\sigma^2)(1-m\sigma^2)]^{1/2}$$

$$= RP^{1/2}, \quad . \quad . \quad . \quad . \quad . \quad . \quad (28)$$

where $$P = 1 + m^2 - 2m\cos 2\theta. \quad . \quad . \quad . \quad . \quad (29)$$

Hence $$-ie^{i\xi} = P^{-1/2}(\sigma - m/\sigma). \quad . \quad . \quad . \quad (30)$$

Taking the conjugate form of this equation, and noting that

$$\overline{\sigma} = e^{-i\theta} = 1/\sigma,$$

we have $$ie^{-i\xi} = P^{-1/2}(1/\sigma - m\sigma). \quad . \quad . \quad . \quad (31)$$

Division of equation (30) by (31) gives the equation

$$e^{2i\xi} = -(\sigma^2 - m)/(1 - m\sigma^2). \quad . \quad . \quad (32)$$

To find an expression for the radius of curvature r of the boundary, differentiate equation (32) with respect to θ, giving the following equation.

$$2ie^{2i\xi}\frac{d\xi}{d\theta}=-\frac{2i\sigma^2(1-m^2)}{(1-m\sigma^2)^2}.$$

Hence, using equation (32),

$$\frac{d\xi}{d\theta}=\frac{(1-m^2)}{(1-m\sigma^2)(1-m/\sigma^2)}=(1-m^2)P^{-1}. \quad . \quad . \quad . \quad (33)$$

Also $$ds=|dz|=|\Omega'(\sigma)|\,d\theta$$

so that $$ds/d\theta=RP^{1/2}. \quad . \quad . \quad . \quad . \quad . \quad . \quad (34)$$

Hence, from equations (33) and (34),

$$r=\frac{ds}{d\xi}=\frac{RP^{3/2}}{(1-m^2)} \quad . \quad . \quad . \quad . \quad . \quad . \quad . \quad (35)$$

With this value of r, equations (19) and (21) now become

$$\widehat{nn}=\frac{(1-m^2)T}{RtP^{3/2}} \quad . \quad . \quad . \quad . \quad . \quad . \quad . \quad . \quad (36)$$

$$\widehat{ss}=\widehat{nn}\left(\mu+\frac{KP^{3/2}}{1-m^2}\right), \quad . \quad . \quad . \quad . \quad . \quad (37)$$

where K is a non-dimensional parameter defined by the equation

$$K=Rt/A=(a+b)\,t/(2A). \quad . \quad . \quad . \quad . \quad (38)$$

Note that K is not necessarily constant, since in general the reinforcing area A may be variable.

6. Elliptical Hole in a Sheet under Tension at Infinity

Consider now the case of a reinforced elliptical hole in a sheet subjected to stresses at infinity given by the equations

$$\widehat{xx}_\infty=f_1, \qquad \widehat{yy}_\infty=f_2, \qquad \widehat{xy}_\infty=0. \quad . \quad . \quad . \quad (39)$$

It will be assumed that, although the reinforcing area A may vary, it is nevertheless symmetrical about both the x and y axes. The stress distribution in the sheet therefore possesses a Type I symmetry (Fig. 3(a)). Hence

$$\left.\begin{aligned}\phi_0(z)&=\alpha z+\alpha_1 z^{-1}+\alpha_3 z^{-3}+\ldots.\\ \psi_0(z)&=\beta z+\beta_1 z^{-1}+\beta_3 z^{-3}+\ldots.\end{aligned}\right\} \quad . \quad . \quad . \quad (40)$$

where all the coefficients are real.

On substituting equations (40) into equations (3) and (4) and letting $z \longrightarrow \infty$, it will be seen that

$$\alpha = \tfrac{1}{8}(f_1 + f_2), \qquad \beta = -\tfrac{1}{4}(f_1 - f_2). \quad . \quad . \quad . \quad (41)$$

Now transform equations (40) into the ζ-plane, using the transformation function given in equation (22), and substitute equations (41). Then, since R, m and all the α_n and β_n are real, it is easy to see that

$$\phi_0(z) = \phi_0[\Omega(\zeta)] = \phi_1(\zeta) = R[\tfrac{1}{8}(f_1 + f_2)\zeta + \phi(\zeta)]$$
$$\psi_0(z) = \psi_0[\Omega(\zeta)] = \psi_1(\zeta) = R[-\tfrac{1}{4}(f_1 - f_2)\zeta + \psi(\zeta)], \quad . \quad . \quad (42)$$

in which $\phi(\zeta)$ and $\psi(\zeta)$ are functions which vanish at infinity and may be written in the form

$$\left.\begin{aligned} \phi(\zeta) &= a_1\zeta^{-1} + a_3\zeta^{-3} + a_5\zeta^{-5} + \ldots . \\ \psi(\zeta) &= b_1\zeta^{-1} + b_3\zeta^{-3} + b_5\zeta^{-5} + \ldots . \end{aligned}\right\} \quad . \quad . \quad . \quad (43)$$

The coefficients a_n and b_n are all real.

Now, from equations (42) it will be seen that

$$\phi_0'(z) = \frac{d\zeta}{dz}\phi_1'(\zeta) = \frac{\phi_1'(\zeta)}{\Omega'(\zeta)} \quad . \quad . \quad . \quad . \quad . \quad (44)$$

and similarly for $\psi_0'(z)$. Hence, on using equations (22), (27), (42) and (44), and replacing ζ by σ, the first boundary condition, equation (13), becomes

$$\sigma\overline{\Omega(\sigma)}\,\phi_1'(\sigma) + \sigma\Omega'(\sigma)[\overline{\phi_1(\sigma)} + \psi_1(\sigma)] = \frac{1}{\sigma}\Omega(\sigma)\,\overline{\phi_1'(\sigma)} + \frac{1}{\sigma}\overline{\Omega'(\sigma)}[\phi_1(\sigma) + \overline{\psi_1(\sigma)}].$$

Substitution of equations (22), (42) and (43) then leads to the following equation:—

$$\left[mb_1 - b_3 + 2a_1 + 2ma_3 + \tfrac{1}{4}m(f_1 + f_2) - \tfrac{1}{4}(f_1 - f_2)\right]\left(\sigma^2 - \frac{1}{\sigma^2}\right) +$$
$$+\left[mb_3 - b_5 + 4a_3 + 4ma_5\right]\left(\sigma^4 - \frac{1}{\sigma^4}\right) + \left[mb_5 - b_7 + 6a_5 + 6ma_7\right]\left(\sigma^6 - \frac{1}{\sigma^6}\right) + \ldots\ldots = 0.$$

This must be true for all values of σ, *i.e.* throughout the boundary. Each individual term in square brackets is therefore zero, giving

$$b_3 = mb_1 + 2a_1 + 2ma_3 + \tfrac{1}{4}m(f_1 + f_2) - \tfrac{1}{4}(f_1 - f_2),$$
$$b_5 = mb_3 + 4a_3 + 4ma_5,$$
$$b_7 = mb_5 + 6a_5 + 6ma_7, \text{ and so on.}$$

Hence, from the second of equations (43),

$$\psi(\zeta)=b_1\zeta^{-1}+m\zeta^{-2}(b_1\zeta^{-1}+b_3\zeta^{-3}+b_5\zeta^{-5}+\ldots.)+(2a_1\zeta^{-3}+4a_3\zeta^{-5}+6a_5\zeta^{-7}+\ldots.)+$$
$$+m(2a_3\zeta^{-3}+4a_5\zeta^{-5}+6a_7\zeta^{-7}+\ldots.)+\frac{1}{\zeta^3}\left[\frac{m}{4}(f_1+f_2)-\tfrac{1}{4}(f_1-f_2)\right].$$

Noticing that the first series on the right hand side of this equation is simply equal to $\psi(\zeta)$ and that the other two series may be written in terms of $\phi(\zeta)$ and $\phi'(\zeta)$ the following equation for $\psi(\zeta)$ is finally obtained.

$$\left(1-\frac{m}{\zeta^2}\right)\psi(\zeta)=-\frac{d}{d\zeta}\left[\left(\frac{1}{\zeta}+m\zeta\right)\phi(\zeta)\right]+\frac{b_1}{\zeta}+\frac{1}{4\zeta^3}[m(f_1+f_2)-(f_1-f_2)]. \quad . \quad (45)$$

Thus, apart from b_1, which remains unknown, we have now determined $\psi(\zeta)$ in terms of $\phi(\zeta)$.

Substitution of equations (22), (31), (42), (44) and (45) into equation (12*a*) gives, after a considerable amount of algebra, the following equation for the tension in the reinforcement, in terms of the coefficients b_1 and a_n.

$$T=4RtP^{-1/2}\left\{\tfrac{1}{8}(f_1+f_2)(1+m\cos 2\theta)+\tfrac{1}{8}(f_1-f_2)(m-2\cos 2\theta)+\tfrac{1}{2}b_1+\right.$$
$$\left.+\sum_{1,3,5,\ldots}^{\infty}a_n[\cos(n+1)\theta-m\cos(n-1)\theta]\right\} \quad . \quad (46)$$

The stresses $\widehat{nn}$ and $\widehat{ss}$ at the boundary may similarly be obtained from equations (15) and (16), while the shear stress $\widehat{sn}$ is derived from equations (4) and (8). After considerable simplification the results are as follows:—

$$\widehat{nn}=4(1-m^2)P^{-2}\{\tfrac{1}{8}(f_1+f_2)(1+m\cos 2\theta)+\tfrac{1}{8}(f_1-f_2)(m-2\cos 2\theta)+\tfrac{1}{2}b_1+$$
$$+\sum_{1,3,5,\ldots}^{\infty}a_n[\cos(n+1)\theta-m\cos(n-1)\theta]\}. \quad . \quad (47)$$

$$\widehat{ss}=-\widehat{nn}+8P^{-1}\{\tfrac{1}{8}(f_1+f_2)(1-m\cos 2\theta)-$$
$$-\sum_{1,3,5,\ldots}^{\infty}na_n[\cos(n+1)\theta-m\cos(n-1)\theta]\}.. \quad . \quad (48)$$

$$\widehat{sn}=-4P^{-2}\left\{\tfrac{1}{4}(f_1+f_2)[(2m+m^3)\sin 2\theta-\tfrac{1}{2}m^2\sin 4\theta]-\right.$$
$$-\tfrac{1}{4}(f_1-f_2)[(2+m^2)\sin 2\theta-m\sin 4\theta]+mb_1\sin 2\theta+$$
$$\left.+\sum_{1,3,5,\ldots}^{\infty}a_n(1-m^2+nP)[\sin(n+1)\theta-m\sin(n-1)\theta]\right\} . \quad (49)$$

As a check, note that equations (46) and (47) satisfy equation (36).

So far, b_1 and the a_n coefficients are unknown. However, the second boundary condition is not yet satisfied, and substitution of equations (47) and (48) into equation (14) now leads to the equation

$$\tfrac{1}{2}b_1 + \sum_{1,3,5,\ldots}^{\infty} (1+nQ)\,[\cos(n+1)\theta - m\cos(n-1)\theta]\,a_n =$$

$$\tfrac{1}{8}(f_1+f_2)\,[(1-m\cos 2\theta)\,Q-(1+m\cos 2\theta)] + \tfrac{1}{8}(f_1-f_2)\,(2\cos 2\theta - m), \qquad (50)$$

where $$Q = 2P/[KP^{3/2} + (1-m^2)(1+\mu)]. \qquad (51)$$

It should be noted that, in general, the cross-sectional area A of the reinforcement, and therefore K, is a function of θ. Furthermore P, defined by equation (29), also varies with θ. Hence, in general, Q is a function of θ and it is impossible to obtain the unknown coefficients from equation (50) simply by a process of comparing coefficients. In fact, only an approximate solution to the problem can be obtained, by retaining a finite number of the a_n coefficients and satisfying equation (50) at an appropriate number of points in the range $0 \leqslant \theta \leqslant \pi/2$. This is the procedure adopted for obtaining the numerical results given later.

There are, however, certain cases of interest in which Q is constant, as follows:—

(*i*) Elliptical hole with no reinforcement.

$$A=0; \quad K=\infty; \quad Q=0.$$

(*ii*) Circular hole with arbitrary constant area of reinforcement.

$$m=0; \quad P=1; \quad K=\text{constant}; \quad Q=2/(K+1+\mu).$$

(*iii*) Elliptical hole designed to be a neutral one for some specific uniform stress system at infinity. (This includes the case of a hole which is neutral for a 2/1 ratio of tensions at infinity, as produced by cabin pressurisation.) It will be shown later that the variations of A and P with θ are such that Q remains constant.

Now if, for any reason, Q is constant, the coefficients b_1 and a_n can easily be determined from equation (50) by comparing coefficients of the various cosine terms, with the following result.

$$\left.\begin{aligned} a_1 &= -\frac{m}{8}(f_1+f_2) + \frac{(f_1-f_2)}{4(Q+1)} \\ b_1 &= \tfrac{1}{4}(f_1+f_2)\,[(1-m^2)\,Q-(1+m^2)] + \frac{m}{4}(f_1-f_2) \\ a_3 &= a_5 = a_7 = \ldots\ldots = 0. \end{aligned}\right\} \qquad (52)$$

With these values for the coefficients the stresses at the boundary, obtained from equations (47), (48) and (49), are as follows.

$$\left.\begin{aligned}
\widehat{nn} &= \frac{(1-m^2)\,Q}{P^2}\left[\tfrac{1}{2}(1-m^2)(f_1+f_2) - \frac{(f_1-f_2)}{(Q+1)}(\cos 2\theta - m)\right] \\
\widehat{ss} &= \left[\frac{2}{P} - \frac{(1-m^2)\,Q}{P^2}\right]\left[\tfrac{1}{2}(1-m^2)(f_1+f_2) - \frac{(f_1-f_2)}{(Q+1)}(\cos 2\theta - m)\right] \\
\widehat{sn} &= \frac{Q}{P^2}\left[\frac{(f_1-f_2)}{(Q+1)}(2\sin 2\theta - m\sin 4\theta) - m(1-m^2)(f_1+f_2)\sin 2\theta\right]
\end{aligned}\right\} \quad . \quad . \quad (53)$$

Note that, for an unreinforced hole ($Q=0$), these equations give $\widehat{nn}=\widehat{sn}=0$ on the boundary as required and agree with the solution given by Inglis[2].

7. Elliptical Hole in a Sheet under Shear at Infinity

Attention is now turned to the case of a reinforced elliptical hole in a sheet subjected at infinity to a pure shear stress parallel to the x and y axes; thus

$$\widehat{xx}_\infty = \widehat{yy}_\infty = 0, \quad \widehat{xy}_\infty = S.$$

The stress distribution then possesses a Type II symmetry (Fig. 3(*b*), p. 378), assuming that the reinforcement is symmetrical about both axes.

Hence $$\phi_0(z) = i(\alpha z + \alpha_1 z^{-1} + \alpha_3 z^{-3} + \ldots)$$
$$\psi_0(z) = i(\beta z + \beta_1 z^{-1} + \beta_3 z^{-3} + \ldots),$$

where the α_n and β_n are real.

The stress conditions at infinity require that

$$\beta = \tfrac{1}{2}S.$$

Also, it is readily seen from equations (3) and (4) that the term $i\alpha z$ in the expression for $\phi_0(z)$ does not affect the stresses; in fact, from equation (6), this term simply represents a rigid body rotation about the origin, and can therefore be omitted. Substitution of $z=\Omega(\zeta)$ then gives the following equations:—

$$\phi_0(z) = iRS\phi(\zeta)$$
$$\psi_0(z) = iRS[\tfrac{1}{2}\zeta + \psi(\zeta)],$$

in which $\phi(\zeta)$ and $\psi(\zeta)$ are functions which vanish at infinity and which may be expressed in the following form, where the c_n and d_n are real:—

$$\phi(\zeta) = c_1\zeta^{-1} + c_3\zeta^{-3} + c_5\zeta^{-5} + \ldots.$$

$$\psi(\zeta) = d_1\zeta^{-1} + d_3\zeta^{-3} + d_5\zeta^{-5} + \ldots.$$

The analysis now follows a course exactly similar to that of the preceding section and only the essential results will be given here. The functions $\psi(\zeta)$ and $\phi(\zeta)$ are related by the equation

$$\left(1-\frac{m}{\zeta^2}\right)\psi(\zeta)=-\frac{d}{d\zeta}\left[\left(\frac{1}{\zeta}+m\zeta\right)\phi(\zeta)\right]+\frac{m}{2\zeta}-\frac{1}{2\zeta^3}. \quad . \quad (54)$$

Expressions for the tension in the reinforcement and the boundary stresses in the sheet are as follows:—

$$T=4RtSP^{-1/2}\left\{-\tfrac{1}{2}\sin 2\theta+\sum_{1,3,5,\ldots}^{\infty}c_n\left[\sin(n+1)\theta-m\sin(n-1)\theta\right]\right\}. \quad (55)$$

$$\widehat{nn}=4S(1-m^2)P^{-2}\left\{-\tfrac{1}{2}\sin 2\theta+\sum_{1,3,5,\ldots}^{\infty}c_n\left[\sin(n+1)\theta-m\sin(n-1)\theta\right]\right\} \quad . \quad . \quad . \quad . \quad (56)$$

$$\widehat{ss}=-\widehat{nn}-8SP^{-1}\sum_{1,3,5,\ldots}^{\infty}nc_n\left[\sin(n+1)\theta-m\sin(n-1)\theta\right] \quad . \quad . \quad . \quad (57)$$

$$\widehat{sn}=4SP^{-2}\left\{(m-\cos 2\theta)(1-m\cos 2\theta)+\right.$$

$$\left.+\sum_{1,3,5,\ldots}^{\infty}c_n(1-m^2+nP)\left[\cos(n+1)\theta-m\cos(n-1)\theta\right]\right\} \quad . \quad . \quad (58)$$

Finally, the equation from which the c_n coefficients can be determined is as follows:—

$$\sum_{1,3,5,\ldots}^{\infty}c_n(1+nQ)\left[\sin(n+1)\theta-m\sin(n-1)\theta\right]=\tfrac{1}{2}\sin 2\theta. \quad . \quad . \quad (59)$$

As with equation (50) of Section 6, the fact that Q is in general a function of θ means that only an approximate solution for the c_n coefficients can be obtained. However, if for any of the reasons specified previously Q happens to be constant, it is easy to see from equation (59) that

$$c_1=\frac{1}{2(Q+1)}, \quad c_3=c_5=c_7=\ldots=0. \quad . \quad . \quad . \quad (60)$$

In this event equations (56) to (58) reduce to the following simple expressions:—

$$\left.\begin{aligned}\widehat{nn}&=-\frac{2S(1-m^2)Q}{(Q+1)P^2}\sin 2\theta\\ \widehat{ss}&=-\frac{2S}{Q+1}\left[\frac{2}{P}-\frac{(1-m^2)Q}{P^2}\right]\sin 2\theta\\ \widehat{sn}&=\frac{4SQ}{(Q+1)P^2}(m-\cos 2\theta)(1-m\cos 2\theta)\end{aligned}\right\} \quad . \quad . \quad . \quad (61)$$

8. Elliptical Hole in a Sheet under Bending Stress at Infinity

The third case to be considered is that of a doubly symmetrical reinforced elliptical hole in a sheet, subjected at infinity to a stress system given by the equations

$$\widehat{xx}_\infty = py, \quad \widehat{yy}_\infty = \widehat{xy}_\infty = 0,$$

where p is a constant defining the magnitude of the stress system. The symmetry here is of Type III (Fig. 3(*c*), p. 378) and the functions $\phi_0(z)$ and $\psi_0(z)$ therefore take the form

$$\phi_0(z) = i\,[\alpha^\star z^2 + \alpha_0 + \alpha_2 z^{-2} + \alpha_4 z^{-4} + \ldots .]$$

$$\psi_0(z) = i\,[\beta^\star z^2 + \beta_0 + \beta_2 z^{-2} + \beta_4 z^{-4} + \ldots .],$$

where the α and β coefficients are all real. The stress conditions at infinity require that

$$\alpha^\star = -\beta^\star = -p/16.$$

It will be seen from equations (3) and (4) that the constant terms $i\alpha_0$ and $i\beta_0$ do not affect the stresses. However, a value for α_0 cannot be arbitrarily prescribed, because this term incorporates the constant of integration in the analysis leading to equation (12). On the other hand, the value of β_0 may be chosen, and it was found convenient to define it by the equation

$$\beta_0 = -m\alpha_0 - \tfrac{1}{8}\,pR^2(m - m^2).$$

With these values for $\alpha^\star$, $\beta^\star$ and β_0 the equations for $\phi_0(z)$ and $\psi_0(z)$ transform into the following:—

$$\phi_0(z) = \phi_1(\zeta) = \frac{ipR^2}{16}\left[-\zeta^2 + \phi(\zeta)\right]$$

$$\psi_0(z) = \psi_1(\zeta) = \frac{ipR^2}{16}\left[\zeta^2 + \psi(\zeta)\right],$$

in which $\phi(\zeta)$ and $\psi(\zeta)$ are functions of the form

$$\phi(\zeta) = g_0 + g_2\zeta^{-2} + g_4\zeta^{-4} + \ldots .$$

$$\psi(\zeta) = h_0 + h_2\zeta^{-2} + h_4\zeta^{-4} + \ldots .$$

and the g_n and h_n are all real. Furthermore the prescribed relation between β_0 and α_0 means that

$$h_0 = -mg_0.$$

The analysis now follows a course exactly similar to that of the two previous sections. It is found that $\psi(\zeta)$ and $\phi(\zeta)$ are related by the equation

$$\left(1-\frac{m}{\zeta^2}\right)\psi(\zeta)=-\frac{d}{d\zeta}\left[\left(\frac{1}{\zeta}+m\zeta\right)\phi(\zeta)\right]+\frac{(1+m)}{\zeta^2}-\frac{(1-3m)}{\zeta^4} \quad . \quad . \quad (62)$$

Expressions for the tension in the reinforcement and the boundary values of the stresses in the sheet are as follows:—

$$T=\tfrac{1}{4}pR^2tP^{-1/2}\left\{(2+m)\sin\theta-(1-2m)\sin 3\theta+\right.$$
$$\left.+\sum_{0,\,2,\,4,\ldots}^{\infty} g_n\left[\sin(n+1)\theta-m\sin(n-1)\theta\right]\right\} \quad . \quad . \quad . \quad (63)$$

$$\widehat{mn}=\tfrac{1}{4}pR(1-m^2)P^{-2}\left\{(2+m)\sin\theta-(1-2m)\sin 3\theta+\right.$$
$$\left.+\sum_{0,\,2,\,4,\ldots}^{\infty} g_n\left[\sin(n+1)\theta-m\sin(n-1)\theta\right]\right\} \quad . \quad . \quad . \quad (64)$$

$$\widehat{ss}=-\widehat{nn}+\tfrac{1}{2}pRP^{-1}\left\{2\sin\theta-2m\sin 3\theta-\right.$$
$$\left.-\sum_{0,\,2,\,4,\ldots}^{\infty} ng_n\left[\sin(n+1)\theta-m\sin(n-1)\theta\right]\right\} \quad . \quad . \quad . \quad (65)$$

$$\widehat{sn}=\tfrac{1}{4}pRP^{-2}\left\{(2+m-8m^2+m^3)\cos\theta-3(1+m^2)(1-2m)\cos 3\theta+\right.$$
$$\left.+2m(1-2m)\cos 5\theta+\sum_{0,\,2,\,4,\ldots}^{\infty} g_n(1-m^2+nP)\left[\cos(n+1)\theta-m\cos(n-1)\theta\right]\right\} \quad (66)$$

Equation (14) now leads to the following equation, from which the g_n may be determined.

$$\sum_{0,\,2,\,4,\ldots}^{\infty}(1+nQ)\left[\sin(n+1)\theta-m\sin(n-1)\theta\right]g_n=$$
$$(1-2m-2mQ)\sin 3\theta+(2Q-2-m)\sin\theta. \quad . \quad . \quad (67)$$

Once again, since Q in general varies with θ, only an approximate solution can be obtained.

If Q is constant, however, equation (67) gives

$$\left.\begin{aligned} g_0&=2(1-m)Q-\frac{2(1+m^2)}{(1+m)}\\ g_2&=\frac{1-2m-2mQ}{1+2Q}\\ g_4&=g_6=g_8=\ldots\ldots=0 \end{aligned}\right\} \quad . \quad . \quad . \quad . \quad (68)$$

With these values for the coefficients, the expressions for the stresses at the boundary reduce to the following:—

$$\left.\begin{aligned}
\widehat{nn} &= \frac{pRQ(1-m^2)(1-m)}{2(1+2Q)P^2}\left\{[m+(1+m)(1+2Q)]\sin\theta-\sin 3\theta\right\}\\
\widehat{ss} &= \frac{pR(1-m)}{2(1+2Q)}\left[\frac{2}{P}-\frac{(1-m^2)Q}{P^2}\right]\left\{[m+(1+m)(1+2Q)]\sin\theta-\sin 3\theta\right\}\\
\widehat{sn} &= \frac{pRQ(1-m)}{2(1+2Q)P^2}\left\{[4m+m(1-m)^2-(1+m)(1-m)^2(1+2Q)]\cos\theta-\right.\\
&\qquad\left.-3(1+m^2)\cos 3\theta+2m\cos 5\theta\right\}
\end{aligned}\right\} \quad (69)$$

9. The Hole which is Neutral for Pressurisation Stresses

Although the requirements for a hole which is neutral when the sheet is subjected to stresses at infinity given by $\widehat{xx}_\infty=2f$, $\widehat{yy}_\infty=f$, $\widehat{xy}_\infty=0$ have been fully worked out by Mansfield[5], it is convenient to reconsider the problem here using the analysis of this paper.

By definition of a neutral hole the stresses are constant throughout the sheet. Hence, from equations (3) and (4),

$$\phi_0(z)=\tfrac{1}{8}fz, \qquad \psi_0(z)=-\tfrac{1}{4}fz,$$

and therefore, from equations (42), it follows that

$$\phi(\zeta)=3mf/(8\zeta), \qquad \psi(\zeta)=-mf/(4\zeta).$$

Thus
$$\left.\begin{aligned} a_1&=\tfrac{3}{8}mf, \quad a_3=a_5=a_7=\ldots\ldots=0\\ b_1&=-\tfrac{1}{4}mf, \quad b_3=b_5=b_7=\ldots\ldots=0\end{aligned}\right\} \quad \ldots \quad (70)$$

Now these functions $\phi(\zeta)$ and $\psi(\zeta)$ must satisfy equation (45), from which it can easily be shown that m satisfies the quadratic equation

$$m^2-6m+1=0.$$

One root of this exceeds unity and can be discarded, since the length of the minor axis would then be negative. The other root is

$$m=3-2\sqrt{2}=(\sqrt{2}-1)^2, \quad \ldots \quad (71)$$

which defines the shape of the ellipse required. The corresponding ratio of the axes is

$$\frac{a}{b}=\frac{1+m}{1-m}=\sqrt{2},$$

which agrees with Mansfield's result.

Substitution of equations (70) and (71) into equation (50), with $f_1=2f$, $f_2=f$, now shows that Q is a constant given by

$$Q=2\sqrt{2}/3. \quad . \quad . \quad . \quad . \quad . \quad . \quad . \quad (72)$$

Further, from equations (29) and (71),

$$P=(2-\sqrt{2})^2\,(3-\cos 2\theta). \quad . \quad . \quad . \quad . \quad (73)$$

Hence, on solving equation (51) for K, we find that

$$K=\frac{Rt}{A}=\frac{5-4\mu-3\cos 2\theta}{2(\sqrt{2}-1)\,(3-\cos 2\theta)^{3/2}}. \quad . \quad . \quad . \quad . \quad (74)$$

This defines the variation of area A of the reinforcement and can easily be shown to agree with Mansfield's result.

The point to be emphasised here, however, is that Q is constant and the stresses in the sheet at the boundary of the hole, for stress systems at infinity other than the one for which the hole is neutral, can easily be determined. It is only necessary to substitute equation (72) into equations (53), (61) or (69), depending upon the stress system at infinity.

(The foregoing analysis applies in detail only to the case of a hole which is neutral under the one specified stress system at infinity. However, it can easily be generalised to cover the case of a hole which is designed to be neutral under a stress system of the form

$$\widehat{xx}=\lambda^2 f, \qquad \widehat{yy}=f, \qquad \widehat{xy}=0.$$

It can be shown that Q is again a constant, equal to $2\lambda/(\lambda^2+1)$.)

Returning to the case where $\widehat{xx}_\infty=2\widehat{yy}_\infty$, the total volume V of reinforcement required around the boundary of the neutral hole may be determined from the equation

$$V=\oint A\,ds.$$

Thence, on dividing by the perimeter of the ellipse, the cross-sectional area A_m of a *uniform* reinforcing member of the same weight is obtained, with the following result:—

$$\left.\begin{aligned} A_m/(Rt)&=1{\cdot}489 \quad \text{if} \quad \mu=1/3 \\ &=1{\cdot}255 \quad \text{if} \quad \mu=1/4 \end{aligned}\right\} \quad . \quad . \quad . \quad . \quad . \quad (75)$$

This result will be used later in discussing the numerical results.

10. Numerical Results for Elliptical Holes with Uniform Reinforcement

A large number of numerical results have been obtained using Silliac, the high speed digital computer of the Adolph Basser Computing Laboratory in the University of Sydney. The values of the parameters used in the computation were as follows.

(*i*) Three shapes of ellipse:—

$$m=0; \quad 0{\cdot}1; \quad (3-2\sqrt{2})$$

$$i.e. \quad \frac{a}{b}=1; \quad \frac{11}{9}; \quad \sqrt{2}.$$

(*ii*) Two values of Poisson's ratio:—

$$\mu=1/4; \quad 1/3.$$

(*iii*) Ten values for the reinforcing area:—

$$\frac{1}{K}=\frac{A}{Rt}=0; \quad \frac{1}{6}; \quad \frac{1}{3}; \quad \frac{1}{2}; \quad \frac{2}{3}; \quad \frac{5}{6}; \quad 1\ ; \quad \frac{5}{4}; \quad \frac{3}{2}; \quad 2.$$

(*iv*) Three loading cases:—

$$f_1=1, \quad f_2=0, \quad S=0;$$
$$f_1=0, \quad f_2=1, \quad S=0;$$
$$f_1=0, \quad f_2=0, \quad S=1.$$

Thus, in all, 180 different combinations of parameters were covered by the computations. The whole process was quite automatic once the machine had been programmed to perform the task and the end result was a table showing the stresses $\widehat{nn}$, $\widehat{ss}$ and $\widehat{sn}$ at various points around the boundary (at intervals of $\theta=15°$) for each combination of parameters.

In assessing the significance of the values of $A/(Rt)$ considered, it is helpful to notice that the total weight of reinforcement is roughly equal to $2\pi RA$, while the weight of sheet removed in forming the hole is roughly equal to $\pi R^2 t$. Hence the ratio of the weight of reinforcement to the weight of sheet removed is roughly equal to $2A/(Rt)$.

As pointed out previously, it is in general impossible to obtain exact solutions. Consequently a finite number of coefficients in the infinite series were retained, the others being assumed zero. For each of the first two loading cases considered, the coefficients retained were b_1, a_1, a_3, a_5, a_7, a_9, a_{11} and their values were determined by satisfying equation (50) at seven points on each quarter of the boundary, namely $\theta=0$, 15°, 30°, 45°, 60°, 75° and 90°. In no case did the ratio a_{11}/a_1 exceed 2×10^{-5}. In the third loading case, that of shear at infinity, only the coefficients c_1, c_3, c_5, c_7 and c_9 were retained, and equation (59) was satisfied at five points, namely $\theta=15°$, 30°, 45°, 60° and 75°. (Note that equation (59) is automatically satisfied at $\theta=0$ and 90°.) The convergence of the coefficients was not quite as

good as in the first two loading cases, but in no case did the ratio c_9/c_1 exceed 6×10^{-5}. It is therefore felt that the solutions are virtually exact for all practical purposes, and that all the calculated stresses are correct to at least three significant figures.

The stresses $\widehat{nn}$, $\widehat{ss}$ and $\widehat{sn}$ were computed at intervals of $\theta=15°$ around the boundary. As might be expected, it was found that the value of Poisson's ratio did not have a profound effect on the stresses, differences of about three per cent being obtained by varying μ between 1/4 and 1/3. Because of space limitations the results are not presented here but they are available in the form of tables in Ref. 8 for the one value of $\mu=1/3$.

11. Stress Concentration Factors Arising from Pressurisation Stresses

The stress values described in Section 10 were used, by superposition, to derive the stresses at the boundary due to the type of stress system existing in a pressurised fuselage, in which one principle tensile stress "at infinity" is twice the other. At each point the two principal stresses, σ_1 and σ_2, were also calculated, and the results are tabulated in Ref. 8.

A distinction must be made between the two possible orientations of the ellipse relative to the stresses at infinity. Therefore two loading cases were considered, depending upon whether the major or the minor axis is parallel to the greater of the two tensile stresses at infinity.

TABLE 1

VALUES OF STRESS CONCENTRATION FACTOR N DUE TO PRESSURISATION STRESSES

(*Note*: The maximum principal stress at infinity acts parallel to the semi-axis of length a.)

	$a/b=1/\sqrt{2}$ =0·707	9/11 =0·818	1·000	11/9 =1·222	$\sqrt{2}$ =1·414
$A/(Rt)=0$	3·328	2·944	2·500	2·136	1·914
1/6	2·408	2·217	1·974	1·754	1·609
1/3	2·006	1·863	1·680	1·512	1·399
1/2	1·823	1·645	1·488	1·343	1·247
2/3	1·752	1·561	1·365	1·219	1·131
5/6	1·738	1·526	1·321	1·161	1·089
1	1·743	1·522	1·306	1·158	1·107
5/4	1·768	1·527	1·302	1·165	1·133
3/2	1·803	1·537	1·309	1·179	1·163
2	1·874	1·571	1·331	1·211	1·217

From these principal stress values, the maximum principal stress occurring anywhere at the boundary in each case was determined, and the results are given in Table I for Poisson's ratio of 1/3. Note that, for the purpose of Table I, the maximum tensile stress at infinity is in each case parallel to the semi-axis of length a. The stress concentration factor N is defined as the ratio of the maximum value of the greater of the two principal stresses, σ_1, occurring at the boundary divided by the maximum principal stress at infinity. Alternatively, since both of the principal stresses σ_1 and σ_2 were positive throughout, N may equally well be defined as the maximum shear stress occurring at the boundary divided by the maximum shear stress at infinity.

The data of Table I are plotted in Fig. 7, from which it will be seen that for each value of a/b there is a limit to what can be achieved in reducing the stress

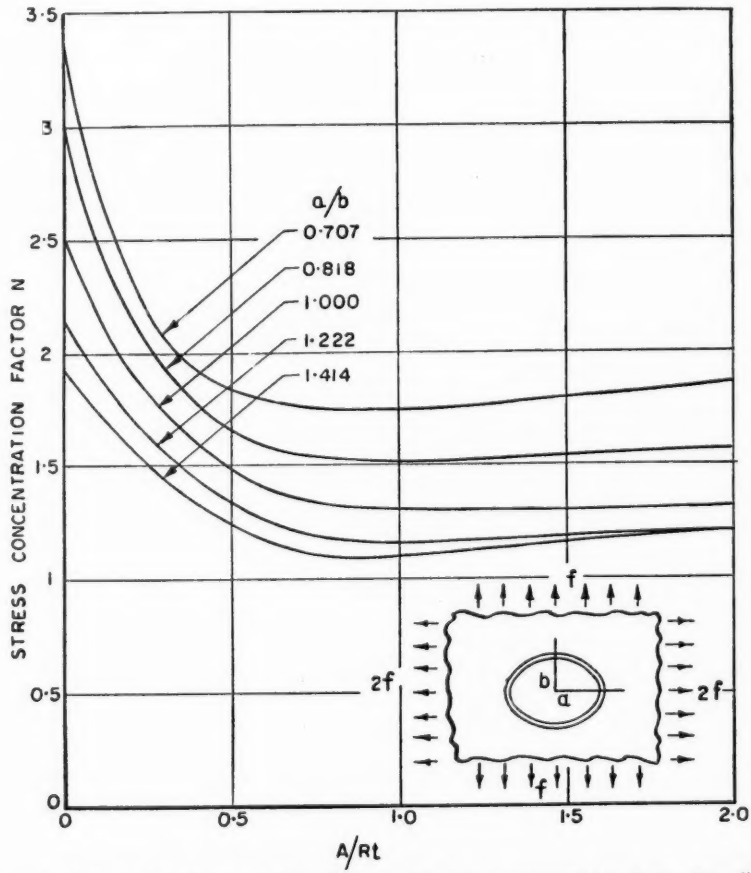

FIGURE 7. Effect of uniform reinforcement on the stress concentration factor for elliptical holes due to pressurisation loads. (Plotted from Table I).

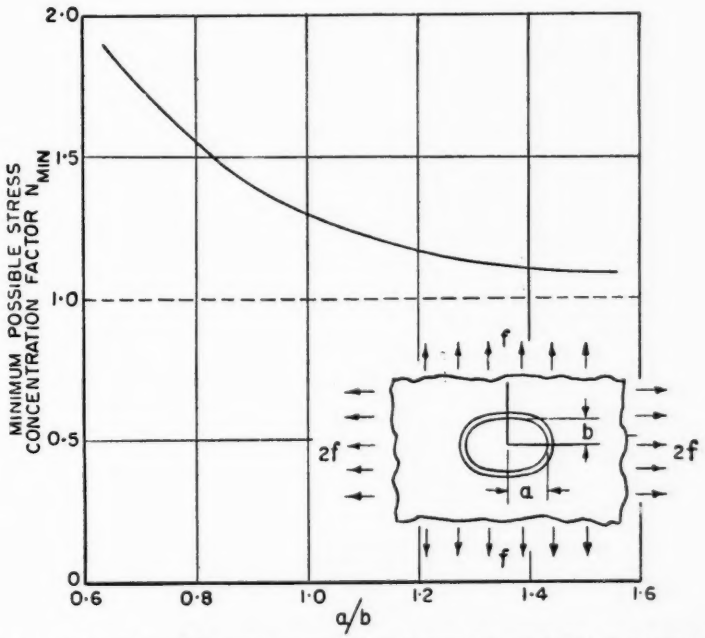

FIGURE 8. Minimum possible stress concentration factors for uniformly reinforced elliptical holes due to pressurisation loads.

concentration factor by means of a uniform reinforcing member. This was previously noted by Wells[3] who pointed out that a reduction of the tangential stress in the sheet at the boundary is achieved only at the expense of the shear stress necessary to build up the tension in the reinforcement. It is also stated by Williams[7] that excessive stiffness in the reinforcement defeats its object by actually attracting loads from the surrounding sheet.

The minimum possible stress concentration factor is plotted against a/b in Fig. 8, from which it appears that the absolute minimum would be achieved by using a hole in which the ratio of axes is somewhat greater than $\sqrt{2}$. This result confirms the prediction of Hicks[4], but it should be pointed out that the corresponding stress concentration factor obtained by Hicks is slightly optimistic, because he based his results on the maximum tangential stress at the end of one of the axes of the ellipse. This is not always identical with the maximum principle stress at the boundary.

With a Poisson's ratio of $1/3$ and a ratio of axes of $\sqrt{2}$ it is interesting to note, from Fig. 7, that a stress concentration factor slightly less than 1·09 can be achieved with a uniform reinforcing member whose area A is about $0{\cdot}8\,Rt$. By equation (75), the weight of such a member would be only about 54 per cent of the weight required for a neutral hole. Thus it appears that it may be advantageous to use a

uniform reinforcing member and to accept a slightly increased stress at the boundary, than to try to eliminate stress concentration completely, which at the same time raises manufacturing difficulties due to non-uniform reinforcement.

12. Conclusions

Solutions have been obtained for a wide range of elliptical holes, of various shapes, with various amounts of uniform reinforcement around the hole, and for various types of loading at infinity.

In the case of a window opening in a pressurised fuselage, a stress concentration factor of 1·09, due to the pressure loads alone, can be achieved by using a uniform reinforcing member whose total weight is only about half that required for Mansfield's neutral hole, but with the same shape of ellipse, *i.e.* with axes in the ratio $\sqrt{2}$.

A curve showing the minimum possible stress concentration factor for various shapes of ellipse is presented (Fig. 8).

(In all the numerical results presented here Poisson's ratio is assumed to be 1/3).

Acknowledgments

The author gratefully acknowledges the help given by Dr. J. M. Bennett and Mr. R. Whitfeld of the Adolph Basser Computing Laboratory in the University of Sydney, in programming the computer to perform the necessary calculations.

References

1. Richards, T. H. Stress Distribution in Pressurized Cabins: an Experimental Study by Means of Xylonite Models. A.R.C. 19, 360, June 1957.
2. Inglis C. E. Stresses in a Plate Due to the Presence of Cracks and Sharp Corners. *Transactions of the Institution of Naval Architects*, Vol. 55, p. 219, 1913.
3. Wells, A. A. On the Plane Stress-Distribution in an Infinite Plate with a Rim-Stiffened Elliptical Opening. *Quarterly Journal of Mechanics and Applied Mathematics*, Vol. 3, p. 23, 1950.
4. Hicks, R. Reinforced Elliptical Holes in Stressed Plates. *Journal of the Royal Aeronautical Society*, Vol. 61, p. 688, October 1957.
5. Mansfield, E. H. Neutral Holes in Plane Sheet—Reinforced Holes which are Elastically Equivalent to the Uncut Sheet. *Quarterly Journal of Mechanics and Applied Mathematics*, Vol. 6, p. 370, 1953.
6. Muskhelishvili, N. I. *Some Basic Problems of the Mathematical Theory of Elasticity*. Noordhoff, Groningen, Holland, 1953.
7. Williams, D. Pressure-Cabin Design. A.R.C. 17,688, March 1955.
8. Wittrick, W. H. The Stresses Around Reinforced Elliptical Holes in Plane Sheet. Aeronautical Research Laboratories (Melbourne) Report A.R.L. S.M. 267.

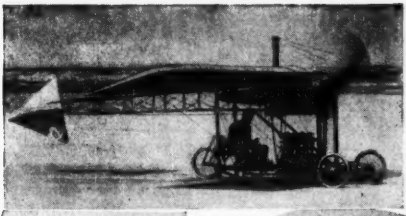

50 years of experience are behind the Blackburn NA.39

1909 Robert Blackburn designed, built and flew his first aircraft at Marske Sands in Yorkshire.

1959 Latest of a long line, the Blackburn NA.39 Strike Aircraft, which first flew on its target date in April, 1958, is now in production. Of this aircraft the Ministry of Defence has stated "In the low-level strike role, the NA.39 is ahead of any aircraft in the world."

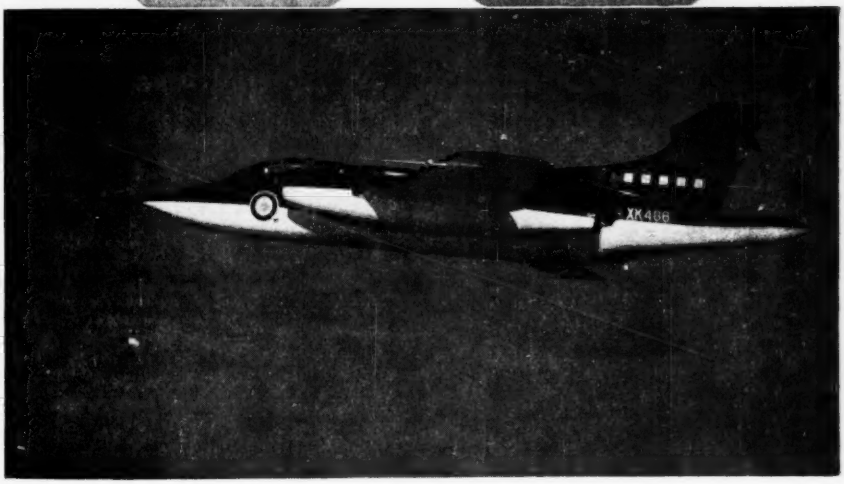

If you are an A.F.R.Ae.S. or possess an equivalent qualification, please write to the Technical Staff Manager, when we shall be pleased to give you details of the opportunities available to experienced men within our technical organisation.

Blackburn Aircraft Limited, Brough, Yorkshire

A128/d

OPPORTUNITIES AT BRISTOL

Opportunities exist for you at Bristol, if you have experience of, or are interested in, the following:—

AERODYNAMICS

DESIGN DRAUGHTSMANSHIP

ELECTRONICS

HYDRAULIC SYSTEMS

MATHEMATICAL PROGRAMMING

MECHANICAL ENGINEERING

MISSILE DYNAMICS AND SERVO-CONTROL SYSTEMS

MISSILE SYSTEM HANDLING AND LOGISTICS

STRUCTURAL DESIGN AND ENGINEERING

Successful applicants are offered:—

Substantial salaries · Worthwhile work on projects for which the Bristol companies hold important contracts · Removal expenses A congenial life in the pleasant West Country, where housing is relatively inexpensive and where there are particularly good facilities for the education of children.

If you are interested, write for an application form to:—

J RAIMES, PERSONNEL MANAGER, ROOM AEO/14/AQ,
BRISTOL AIRCRAFT LIMITED, FILTON, BRISTOL.

BRISTOL

BRISTOL AIRCRAFT LIMITED

NOTICE TO CONTRIBUTORS

1. All communications should be addressed to the Editor, The Aeronautical Quarterly, 4 Hamilton Place, London, W.1.

2. Papers for consideration should be typewritten with double spacing and be accompanied by a summary of not more than 250-300 words. *Papers must be as short as possible*, otherwise considerable delay in publication will result, and in any case they should not be longer than twenty foolscap pages. Full descriptions and complete results of work, as written for an internal report, are not suitable for publication in *The Aeronautical Quarterly*, and such reports need to be rewritten in concise form. Only necessary equations should be included in the text; routine mathematics should be omitted or given as an Appendix to the paper. Illustrations should be reduced to a minimum. The titles of papers should be kept short—with sub-titles if necessary.

3. Only simple symbols and formulae should be typewritten. All others should be written clearly in ink. Greek letters should be indicated and a clear distinction drawn between capital and small letters. Particular attention should be paid to the use of alpha and *a*, kappa and *k*, mu and *u*, nu and *v*, eta and *n*. The letter *l* must be distinguished from the numeral 1, and the letter *O* from the zero 0.

   The use of dots, bars, and so on, over letters, or the use of dots as multiplication signs and bars for brackets should be avoided as far as possible.

   Suffixes and prefixes must be indicated clearly and complicated suffixes and prefixes should be avoided.

4. A list of *all* symbols used, both in the illustrations and text, *must* be given at the end of the paper whether they are standard or not.

5. *Clear* diagrams or sketches must be submitted for redrawing by the Society's draughtsman.

   Photographs must be not less than half plate size and must be clear black and white glossy prints.

6. References should be given in the form:—
   WARD, G. N. Calculation of Downwash Behind a Supersonic Wing. *The Aeronautical Quarterly*, Vol. I, pp. 35-38, May 1949.

7. The copyright of every paper printed in *The Aeronautical Quarterly* is the property of The Royal Aeronautical Society. Permission to reprint or to use any paper will not be unreasonably refused.

8. It is a condition of publication that the author shall have obtained consent where necessary to use any material in his paper which is copyright or the property of any other person or his employers.

9. Authors will be entitled to 20 reprints of their papers free of charge. This number will be shared between joint authors.

The Aeronautical Quarterly is published at the Offices of The Royal Aeronautical Society, 4 Hamilton Place, Piccadilly, London, W.1, at 15s. 0d. net for a single number to non-members and 7s. 6d. net for a single number to members of The Royal Aeronautical Society. Instructions for Contributors are given above. None of the papers must be taken as expressing the opinion of the Council of The Royal Aeronautical Society unless such is definitely stated to be the case. All communications for publication or advertisement in The Quarterly should be addressed to—The Editor, The Aeronautical Quarterly, 4 Hamilton Place, W.1.

Telephone: Grosvenor 3515 (5 lines). Telegraphic Address: Didaskalos, Audley, London

THE AERONAUTICAL QUARTERLY

It is the aim of *The Aeronautical Quarterly* to attract not only original papers contributing to aeronautical science and engineering, and papers developing new or improved methods of analysis and experimental techniques, but also papers on allied sciences which have a bearing on aeronautical problems. *The Aeronautical Quarterly* is open to authors of any nationality and is not restricted to members of the Society.

VOLUME X

Volume X of *The Aeronautical Quarterly* is published in four parts, in February, May, August and November 1959. The prices, *including postage and packing*, are:—

	To Members of the Society		*To Non-Members*	
	£ s. d.		£ s. d.	
Per Part	8 0	($1.15)	15 6	($2.20)
Subscription (4 parts)	1 12 0	($4.50)	3 2 0	($8.70)

Papers to be published in forthcoming issues include:—

J. S. Przemieniecki—Analysis of Struts with Linearly Varying Axial Loading.

N. Curle—The Estimation of Laminar Skin Friction, including the Effects of Distributed Suction.

M. D. Wood, J. H. Horlock and E. K. Armstrong—Experimental Investigations of the Stalled Flow of a Single-Stage Axial Flow Compressor.

R. Hicks—The Bending and Twisting of a Flat Elastic Plate with a Reinforced Circular Hole.

R. J. Tonks and A. G. Smith—A Theory for Flow with Axial Symmetry in Centrifugal Impellers running at Low Speed.

Hugh L. Cox and Jack Boxer—Vibration of Rectangular Plates Point—Supported at the Corners.

8724

PRINTED BY THE LEWES PRESS, WIGHTMAN & CO. LTD., LEWES, SUSSEX, ENGLAND, AND PUBLISHED BY THE ROYAL AERONAUTICAL SOCIETY, 4 HAMILTON PLACE, LONDON, W.1, ENGLAND.